# Methods for Compact Modeling of Process Variations in Silicon Photonics Devices

by

Germain Martinez

S.B. Electrical Engineering
Massachusetts Institute of Technology, 2016

Submitted to the Department of Electrical Engineering and Computer Science
in Partial Fulfillment of the Requirements for the Degree of

Master of Engineering in Electrical Engineering and Computer Science

at the

Massachusetts Institute of Technology

February 2018



Signature of Author: _____

Department of Electrical Engineering and Computer Science
February 2, 2018

Certified by: _____

Duane S. Boning
Clarence J. LeBel Professor
Electrical Engineering and Computer Science
Thesis Supervisor

Accepted by: _____

Christopher J. Terman
Chairman, Masters of Engineering Thesis Committee

# Methods for Compact Modeling of Process Variations in Silicon Photonics Devices

by

Germain Martinez

Submitted to the Department of Electrical Engineering and Computer Science
February 2, 2018
In Partial Fulfillment of the Requirements for the Degree of Master of Engineering in Electrical Engineering and Computer Science.

**Abstract**

Photonic systems are being developed with extensions to existing CMOS processes, and are growing in complexity. Silicon photonics designs are evaluated in simulation using similar methods to those used for CMOS transistor and circuit designs; simulation models for common silicon-based photonics structures and devices currently exist and are used to design larger photonic systems. However, these photonics models are often not constructed with manufacturing variations in mind. This thesis presents methods for creating simulation models for nanophotonic devices that take systematic and random variations from manufacturing into account. Factorial experiment design is used to explore the effect of process variations on photonic device performance. Corner models are constructed using the results from experiment design and capture worst-case variations. The response surface modeling method is employed to develop parameterized compact models. Example variation-aware compact models are generated using these methods for the directional coupler and the Y-branch, two passive devices widely used in silicon photonics. The use of these models is demonstrated through corner and statistical variation analyses of a simple Mach-Zehnder interferometer photonic circuit composed of the directional coupler and Y-branch devices.

Thesis Supervisor: Duane S. Boning
Title: Clarence J. LeBel Professor, Electrical Engineering and Computer Science

## Acknowledgements

Behind every research project and thesis is a group of people that helped the student see it through to fruition. My project is no exception to this. I am extremely grateful to all the people I have worked with over the span of the project; without their support, this thesis would not have been realized.

First and foremost, I want to give a special thanks to my research advisor and academic advisor, Professor Duane S. Boning. I have not met anyone that is as passionate about their field of expertise as Duane. His expert insight, continued enthusiasm, and endless patience kept me inspired to continue working on research week after week. As an undergraduate at MIT, I was privileged to have the assistance of an award-winning undergraduate advisor as I made tough decisions throughout my undergraduate studies. Now, as a graduate student and alumnus of MIT, I am eternally grateful for his invaluable support throughout my Master's research.

Next, I want to thank Professor Jacob White and Professor Luca Daniel. I am privileged to have had the chance to work with two leading professors in numerical methods. Furthermore, their thoughts, questions, and criticisms were instrumental in the process of clarifying the modeling methods introduced in this thesis. I also want to thank the other students in the Statistical Metrology group. Their insight and suggestions during each group meeting was always helpful; their feedback and questions helped motivate the thesis' focus on methodology.

I want to thank PhoeniX Software for the contribution of their OptoDesigner software used in parts of this work. I also thank Jonas Flueckiger at Lumerical Inc. for helpful conversations.

I want to thank AIM Photonics for their contributions to this research project. This research has been supported in part under AIM Photonics: this material is based on research sponsored by Air Force Research Laboratory under agreement number FA8650-15-2-5220.

The U.S. Government is authorized to reproduce and distribute reprints for Governmental purposes notwithstanding any copyright notation thereon. The views and conclusions contained herein are those of the authors and should not be interpreted as necessarily representing the official policies or endorsements, either expressed or implied, of Air Force Research Laboratory or the U.S. Government.

Last but not least, I could not have completed this research without the support of my friends and family. I want to acknowledge my close friends Colin Fraser, David Jin, and Austin Liew, and my lifelong friend Michael Mitchell. They have been there for me when things were at their best and at their worst. I am ever grateful for their undying loyalty. I want to thank my mom and dad for always being supportive. I'm continually inspired by their perseverance against all odds. I want to thank my two sisters (Karen and Cindy), and my four brothers (Luis, Gabriel, Angel, and Jesus) for growing up to be fantastic people; they're the best family anyone could ask for. Despite being over 1,000 miles away in Chicago, IL, my family has been supportive as I have traveled through the peaks and valleys of academic life. I am eternally grateful to have them as my source of strength.

Thank you,

Germain Martinez

# Contents

# List of Figures

# Chapter 1

# Introduction

The semiconductor industry continues to improve on past integrated circuit designs, even after 40 years of continuous growth. Devices in current designs have become smaller and have more complicated behavior making them more complex to manufacture. In an effort to increase the product yield and efficiency of fabricated silicon wafers, techniques for modeling manufacturing process variations have been developed [1]. These techniques involve creating physical models and predictive tools based on empirical data collected from wafer and process fabrication. Simulation tools can be created based on these models; these tools are used to quickly evaluate expected yield and performance of integrated chip designs before they are sent out to fabrication.

As the demand for faster circuit interconnects and larger data transmission bandwidth continues to grow, the newer field of silicon-based photonics grows with it. The use of optical links for backplane, chip-to-chip, and on-chip communications instead of copper connections is being investigated. This is due to the higher data bandwidth that can be transmitted with light. Indeed, a microprocessor that uses optical waveguides to communicate information around the chip has been developed [2]. This system demonstrated the capabilities of using the same CMOS manufacturing process to develop both photonic components and digital circuits that interface with optical systems.

In addition, large-scale integrated photonics designs such as compact phased arrays are becoming feasible. Indeed, Watts, et al., have demonstrated the function of a photonic phased array developed using CMOS-based manufacturing processess [3]. This design consists of a grid of 64x64 optical antennas acting as light emitters. Designing a phased array like this requires care. Each light emitter component has to be sized so that it emits light with a specific pattern of amplitude and phase, which takes effort to design. Fabricating precise components on a silicon chip that match the design is difficult due to the imperfect nature of semiconductor manufacturing.

One way to reduce the time it takes to create silicon-based designs is to evaluate their performance in simulation. This is a common practice in CMOS-based electronic designs; efforts are constantly made to create MOSFET design models in simulation that adhere to a set of manufacturing process rules. This means that a circuit designer can create large-scale designs without having to worry about the device physics at every step. These models can also take manufacturing variations into account. While there are many physical models and simulation-based models developed for the quick evaluation of transistor-based integrated chip designs, there are currently few models for quickly evaluating integrated photonics designs, particularly those that account for manufacturing variation. Photonics designs can be released much more quickly if a designer has simplified, variation-aware compact models, together with photonics design tools that account for systematic and random variations.

Industry and academia have devoted a significant research effort towards the development of models for semiconductor device and integrated circuit evaluation and design, including models to accommodate manufacturing variations. The MIT Virtual Source (MVS) compact MOSFET model, developed by Antoniadis, et al., is a recent example of many proposed models used to quickly characterize transistor behavior [4]. This physical model describes MOSFET behavior on an individual device basis, and is used in simulations and hand calculations. The solid-state physics are abstracted away, and the phenomena that are critical to the function of the MOSFETs, like carrier mobility, are considered. This model proves

useful to both MOSFET designers that have to devise a device with desired or improved performance, and to process developers that have to construct the devices. However, it does not take into account the effects of multiple transistors over a certain area, like on a silicon wafer, particularly the variations in the manufacturing process that may impact different transistors. Extensions to statistical and variation-aware versions of the MVS model have been developed, enabling statistical characterization and extraction, and variation analysis of advanced technologies [5, 6, 7].

Boning et al. have also explored and developed statistical models that take into account spatial- or layout-dependent variations that occur in integrated chip manufacturing [8]. For example, such models can take into account how densely-packed transistors and other silicon-based devices are different on different areas of a chip. The more densely-packed the devices, for example, the lower the planarization rate may be to form the devices, giving rise to thickness deviations within the chip. This leads to differences in device operation that are dependent on where the devices are located with respect to one another; densely-packed transistors may perform similarly to one another, but have degraded performance compared to transistors in sparse areas. Models have been developed by Boning et al. that capture this phenomenon and are now used in design validation and simulation. Another example predicts the effects that deep reactive ion etching has on structures made in silicon, which has applications in the creation of MEMS structures [9].

As mentioned before, a nanophotonic phased array has been developed by Watts, et al., and utilizes conventional semiconductor fabrication techniques. This phased array consists of a 64x64 grid of optical nanoantennas made on a silicon chip. Each of them are controlled and designed to emit a far-field light pattern in the shape of the MIT logo. The scale of the design is large enough to observe spatial variation in the intensity of the light that the nanoantennas emit. However, to date only limited analysis of manufacturing variation and its impact on these photonic structures has been performed [3].

Furthermore, the design process for a large-scale system like the phased array is challeng-

ing. Currently, a silicon photonics systems designer often has to begin development from the physical component level [10]. They have to individually modify each component at each layout layer level, down to the shape of the structures. In the phased array example, this means individually sizing phase elements of each optical nanoantenna and simulating the far-field patterns from each one. Thus, a silicon photonics system will typically take a long time to design and may not be robust against manufacturing variations.

One approach to the problem of manufacturing large-scale light-based systems is to create better simulation models. This approach has proven useful in the past; indeed, this is one reason why the semiconductor industry has been successful. These simulation models are bundled into a Process Design Kit (PDK) that is then sent to circuit designers to use. This effectively separates the tasks that must be done to design, model, and fabricate these individual devices from the circuit design task. Circuit designers use the PDKs to create and debug their designs and layouts; the designs are then sent to foundries to realize the designs [10]. This is the design approach that the field of silicon photonics is moving towards. To date, initial simplified or compact models for various silicon photonics structures have been constructed in MATLAB and Verilog-A and have shown good accuracy [11, 13]. However, little work has been done to demonstrate the creation of photonic device and circuit simulation models with manufacturing variation in mind.

In order to create effective photonic circuit designs, variation effects have to be incorporated in the component models. So far, there are only a few research studies that quantify how manufacturing variations have an effect on the operation of silicon-based photonic structures. As an example, consider the microring resonator structure. These structures are designed so that light with certain wavelengths, or modes, will transmit through the structure; light with shorter or larger wavelengths will not transmit. One metric that measures how well only the desired wavelengths of light transmit through the microring is the quality factor. In one study, it is reported that imperfections in Silicon-on-Insulator microring resonator structures can cause the quality factor to vary widely; for the structures considered,

the quality factor can vary from 20000 to 50000 [14]. Another statistical study found that the resonant wavelengths in both TE and TM modes can change when the microring thickness and waveguide lateral widths are subjected to variations [15]. As part of the design process, it is necessary to analyze these effects in order to quantify and account for them.

The goal of this thesis is to take some of the predictive and statistical modeling techniques already developed for modeling manufacturing variations in transistor and electronic designs and apply them to silicon photonics devices. These modeling techniques will allow for the creation of simplified variation compact models that can be used to simulate variations in large-scale photonics systems. The work described in this thesis aims to combine these techniques to develop a methodology for the creation of variation-aware simulation models for silicon photonics.

In Chapter 2 we discuss the necessary background in experiment design and photonic devices that will be used throughout the thesis. Two variation-aware modeling methods are suggested in this thesis. The first, described in Chapter 3, is a method to create worst-case photonics device corner models in simulation. The second method, explained in Chapter 4, describes the development of a parametric compact model that can be used in conjunction with random sampling to estimate the impact of random variations. This method is based on the response surface modeling method that is commonly used in evaluation and optimization of manufacturing processes [18, 19]. Simulation results obtained in developing the device corner model can also be used to develop an estimate of the underlying functional relationship; this estimate is then used to predict the effects of random process perturbations on photonic device and circuit performance.

Chapters 3 and 4 explain the modeling methods and provide examples of device models. Chapter 5 builds upon the methods by applying the variation compact models to photonic circuit simulation. Mach-Zehnder Interferometers composed of Y-branch and directional couplers are analyzed using the corner and statistical device compact models demonstrated in this thesis. Chapter 6 provides a summary of the thesis and discusses some future directions

for silicon photonics.

# Chapter 2

# Background

This chapter gives an overview of the background concepts and device operation that are used throughout the thesis. In particular, the methods for designing systematic test sets of variation, known as the Design of Experiments, are described in Section 2.1. A description of the Silicon-on-Insulator (SOI) process used to created photonic integrated circuits is provided in Section 2.2. Then, in Section 2.3, the typical behavior of a few key fundamental photonic devices is explained. These devices are used to demonstrate the variation-aware compact modeling methods developed in this thesis, in part because of their simple integration into more complex circuits. As one photonic circuit example, the Mach-Zehnder Interferometer (MZI) can be made using only Y-branches and waveguides [11]. MZI circuits can also be made using directional couplers and waveguides [16], and with additional components, such as controlled phase elements, they can be the basis for photonic signal modulation. The application of variation compact models developed in Chapters 3 and 4 will be illustrated for a simple MZI in Chapter 5. Finally, Section 2.4 will summarize the key ideas of this chapter.

## 2.1 Design of Experiments

In the methods that are described in this thesis, a set of process variations are defined as the "inputs" to the fabrication of a photonic device or system; the responses or changes in behavior of the device as a result of these variations are taken to be the "outputs" of the system. The procedure for systematically exploring the output behavior of a device or process based on a set of inputs that are hypothesized to recreate real process variations in said device is called the Design of Experiments (DoE) [18]. In a design of experiments, the number of input parameters is controlled, as well as the amount that the input parameters are allowed to change. Combinations of these input parameter values are selected as testing points that the system is evaluated at. These testing points are typically chosen by a predetermined scheme such that a predictive simulation model can be constructed from their outputs. This provides a systematic method to evaluate the effects of different process variations on a particular device. In this section, the DoE designs used for the creation of variation-aware compact models are discussed.

### 2.1.1 Factorial Design

A design of experiments involves choosing a set of preconditions, or input design variables, that are hypothesized to cause changes in the output. These input variables are then perturbed around a central test case, usually called the "nominal" test case, by predefined amounts. The magnitude of each variation is determined based on the range of validity desired for the model, or on the expected range of variation in the physical fabrication process. For example, a typical approach or rule of thumb is that variation parameters can change by $\pm 5\%$ of their nominal value. Using the factorial design method, a single variation parameter can be tested at two or more different values; often the nominal value is also chosen as a testing parameter. With multiple input design variables, it is possible and important to evaluate the output behavior with respect to combinations of different parameters when

interaction between these parameters might exist. The extent of the information that can be extracted from a design of experiments is dependent on choosing the set of combinations of input parameters to test. Generally, as more combinations of input parameters are tested, more information from the underlying output behavior of a device can be extracted, and more sophisticated models can be fit or generated.

One important DoE design is the $2^k$ (or $2^k + 1$) factorial design. We let $k$ be the number of input parameters or control variables that are under consideration in each experiment. We first define a central test case for each parameter tested, known as the "nominal" case. We next define two levels for each control variable that represent a positive and negative deviation from the nominal case [18]. We can code these levels using a linear transformation:

$$x_{i,coded} = \frac{x_i - 2(x_{i,+dev} + x_{i,-dev})}{x_{i,+dev} - x_{i,-dev}}, \tag{2.1}$$

where $x_{i,+dev}$ is the positive deviation in $x_i$ and $x_{i,-dev}$ is the negative deviation in $x_i$. If a symmetric deviation is chosen, then the positive deviation in $x_i$ is thus coded to be $x_{i,coded,pos} = +1$ and the negative deviation in $x_i$ is coded to be $x_{i,coded,neg} = -1$. In the $2^k$ factorial design, all possible combinations of the positive and negative deviations for the $k$ parameters are considered. The $2^k + 1$ design also adds the nominal case, coded as $x_{i,coded,nom} = 0$. In general, for any number of input variables $k$, a $2^k$ factorial design has the following design matrix:

$$D_{2^k} = \begin{bmatrix} x_{1,coded,pos} & x_{2,coded,pos} & \cdots & x_{k,coded,pos} \\ x_{1,coded,pos} & x_{2,coded,pos} & \cdots & x_{k,coded,neg} \\ x_{1,coded,pos} & x_{2,coded,neg} & \cdots & x_{k,coded,pos} \\ \vdots & \vdots & \vdots & \ddots \\ x_{1,coded,neg} & x_{2,coded,neg} & \cdots & x_{k,coded,neg} \end{bmatrix} \tag{2.2}$$

Note that every possible combination of the positive and negative deviation for every single

input variable case is included in the $2^k$ design matrix; the nominal values are ignored. For $k = 2$, a $2^k$ factorial design has the following design matrix:

$$D_{2^k} = \begin{bmatrix} 1 & 1 \\ 1 & -1 \\ -1 & 1 \\ -1 & -1 \end{bmatrix} \tag{2.3}$$

There are $2^2 = 4$ rows in this design matrix. For $k = 3$, the number of rows in the design matrix increases to $n = 8$, and $k = 4$ has $n = 16$ rows. Note also that the number of columns in the matrix is equal to the number of input variables that are being changed.

Selecting combinations of the two levels alone is sufficient to characterize the system as a first-order model, with first order interactions. This is enough to investigate how multiple input variations applied simultaneously can affect the output. However, it is often desired to incorporate the effects of higher order powers or combinations of variables in a compact model. An experiment design that utilizes combinations of three design levels instead of two is called a $3^k$ factorial design [18, 19]. Three levels for each control variable are defined instead of two: a positive deviation, a negative deviation, and a "nominal" value that is considered to be the central case. If a parameter coding scheme is applied and a symmetric deviation is chosen, then the corresponding values of the coded variable are $x_{i,coded,pos} = +1$, $x_{i,coded,neg} = -1$, and $x_{i,coded,nom} = 0$, respectively. In general, for any number of input

variables $k$, a $3^k$ factorial design has the following design matrix:

$$D_{3^k} = \begin{bmatrix} x_{1,coded,pos} & x_{2,coded,pos} & \cdots & x_{k,coded,pos} \\ x_{1,coded,pos} & x_{2,coded,pos} & \cdots & x_{k,coded,nom} \\ x_{1,coded,pos} & x_{2,coded,pos} & \cdots & x_{k,coded,neg} \\ \vdots & \vdots & \cdots & \vdots \\ x_{1,coded,nom} & x_{2,coded,nom} & \cdots & x_{k,coded,pos} \\ x_{1,coded,nom} & x_{2,coded,nom} & \cdots & x_{k,coded,nom} \\ x_{1,coded,nom} & x_{2,coded,nom} & \cdots & x_{k,coded,neg} \\ \vdots & \vdots & \vdots & \ddots \\ x_{1,coded,neg} & x_{2,coded,neg} & \cdots & x_{k,coded,neg} \end{bmatrix} \tag{2.4}$$

Note that every possible combination of the three design levels for every single input variable case is included in the design matrix. For example, if $k = 2$, a $3^k$ factorial design has the following design matrix:

$$D_{3^k} = \begin{bmatrix} 0 & 0 \\ 0 & 1 \\ 0 & -1 \\ 1 & 0 \\ 1 & 1 \\ 1 & -1 \\ -1 & 0 \\ -1 & 1 \\ -1 & -1 \end{bmatrix} \tag{2.5}$$

There are $3^2 = 9$ rows in this design matrix. For $k = 3$, the number of rows in the design matrix increases to $n = 27$, and $k = 4$ has $n = 81$ rows. Note also that the number of columns is still equal to the number of input variables that are being changed. For testing the effects of larger numbers of variables on a system, this DoE method requires more experiments and

results in a higher cost.

### 2.1.2 Modified Factorial Design

The cost of the $3^k$ factorial DoE design for higher quantities of control variables is mitigated by modifying the DoE. Choosing to run parts of the overall factorial DoE is a compromise between model/DoE accuracy and speed, in general. A common compromise when $k$ is larger than two or three is to use the $2^k + 1$ design, or related designs such as a central composite design that combines axial and corner points. These still allow low-order models to be developed but with reduced number of cases compared to a $3^k$ experiment.

We are interested in "corner models" that measure the effects of variations in combinations of the different input variables; often "multivariate variation" cases can cause the largest deviation from desired operation, more so than variations from only a single variable. The multivariate cases will often produce the "worst-case" performance that is desired for identifying and bounding the worst-case behavior of a particular device. Thus, $2^k$ factorial DoEs are often used to find corners, while extended $2^k$ or modified $3^k$ factorial DoE designs can be constructed by adding additional test cases in addition to (and reusing) the $2^k$ corner points, for the purposes of more detailed model fitting.

Furthermore, in testing of larger designs, it is often desired to understand the effect that one variable may have on every component in a photonic system. An example is the scenario where every waveguide in the photonic circuit has the desired cross-sectional width but all deviate from their nominal thickness by -5%. This could be caused by a situation where the manufacturing process does not deposit enough silicon on a given wafer during the silicon fabrication step of the SOI process; the wafer then results in photonic integrated circuits where all of the waveguide thicknesses are modified from their nominal thickness in the same way. In the worst-case, perhaps corresponding to some known bound on this deviation, this waveguide thickness might be 5% less than what the typical manufacturing process produces. To account for this situation, a photonic circuit simulation should be

run where every component has this smaller waveguide thickness. The corner model for each component used in the simulation would thus have to account for cases where only a single control variable changes. These may be called the "univariate variation cases" and are automatically included in a $3^k$ factorial DoE design. However, a full $3^k$ design may include many more combinations than are needed, when $k$ is large. Instead, a central composite design consisting of a $2^k + 1$ design augmented by univariate axial cases is a modified DoE design that enables both single parameter and parameter-combination corners to be evaluated, with reasonable cost.

In the corner analysis method described in Section 3.1, the DoE used is a combination of the $2^k$ multivariate cases, the $2k$ univariate cases, and a nominal design case, all as described here. This takes into account the worst cases for variations across combinations of multiple control variables (the multivariate variations) as well as the worst cases for changes in a single control variable (the univariate variations). These designs are also sufficient for building polynomial response surface models.

## 2.2 Silicon Photonics Process

In silicon photonics, waveguides formed from silicon are a fundamental and core element of both passive and active devices. Waveguide dimensions are defined by the manufacturing process in which they are made. In a typical manufacturing process, silicon waveguides are made on a Silicon-on-Insulator wafer [11]. The silicon layer resides in between two layers of silicon dioxide, the oxide layer of the starting wafer below the silicon layer, and an oxide layer subsequently deposited above and around the silicon waveguide. Silicon is used as a waveguide material due to its high refractive index ($n_{Si} = 3.4$ to $3.5$); the refractive index difference between silicon and silicon dioxide ($n_{Oxide} = 1.444$) is high, allowing for light to be confined within the waveguide [24].

A typical silicon photonics device process is made using the following cross-sectional

measurements. A typical 200 $mm$ area Silicon-on-Insulator wafer consists of a 725 $\mu m$ silicon substrate as the bottom layer. On top of that layer, a 2 $\mu m$ thick silicon dioxide layer is formed; this is known as the buried oxide layer. A 220 $nm$ thick layer of crystalline silicon is formed on top of the buried oxide layer, resulting in the "starting" SOI wafer for subsequent wafer fabrication. This layer is shaped using lithographic and etching processes to remove excess silicon; it is this process step that forms the photonic waveguides. This lithography and etching process is responsible for the waveguide widths; a typical silicon slab waveguide width is 500 $nm$. Any variations in the etching process can result in a variation in the widths of each manufactured waveguide. After the desired waveguide shapes are formed, a second (e.g., 2 $\mu m$ thick) layer of silicon dioxide is deposited across the entire wafer [11]. Subsequent processing may form other structures above the silicon layer, including silicon nitride waveguides, as well as metal wiring, photodetectors, etc.

It is desired to choose variations for analysis based on the photonics process; the simulation models are meant to approximate the effects of such process variations on manufactured photonics components. The devices considered in this thesis are formed in simulaton software assuming the SOI process described above. A silicon thickness of 220 $nm$ is chosen as a nominal value for all of the examples. This silicon thickness is a standard used by many SOI photonics wafer foundries [11, 22]. Past research has found that a variation range of $\pm$ 5 $nm$ in silicon-layer thickness is possible from wafer to wafer [22, 23].

## 2.3 Device Operation

In order to understand and model the effects of possible variation sources in a given device, it is first necessary to understand how that device is supposed to operate normally. In this section, the nominal operation is described for both the Y-branch device and the directional coupler device. Both of these devices are passive. In other words, they only require light to operate in normal conditions; they do not use any extra powered electrical compo-

nents to modify the device behavior. These two photonic components are chosen because they have multiple geometric parameters that can be tested as sources of manufacturing variation; examples of variations that can be tested are thickness and widths of different device waveguide branches, as well as material properties (index of refraction) in the device.

### 2.3.1 Y-Branch

A top view of the Y-branch device is shown in Figure 2.1a. In the "forward" direction, this device is designed to propagate and split light into two different waveguides. When operated in the "reverse" direction, this same geometry can serve as a combiner. As a splitter, light passes through the single waveguide on the left side and passes into a shaped waveguide taper structure. The taper structure gradually gets wider along its length to create a slight perturbation in the modes of light [11, 25]. This perturbation forces the input power of the light to split between the two output branches.

In a perfect device, each output branch would transmit the same amount of power; i.e., half of the power of the input branch. This is not necessarily true in an imperfect Y-branch device. One reason why the Y-branch is used in this thesis to develop and demonstrate variation modeling methods is because of the simplicity of the effects that process variations have on the device. If there is asymmetry in the geometric layout due to variation, the device operation will reflect this, for example.

The particular Y-branch shape shown in Figure 2.1a is selected for its low insertion loss. The shape of the taper has previously been optimized so that the Y-branch will have an insertion loss that is less than 0.3 dB, and backscatter is minimized [11, 25]. This design serves as an excellent example to illustrate the unbalancing effects that process variations can have on a photonic device and to demonstrate the modeling methods used to generate variation-aware compact models.

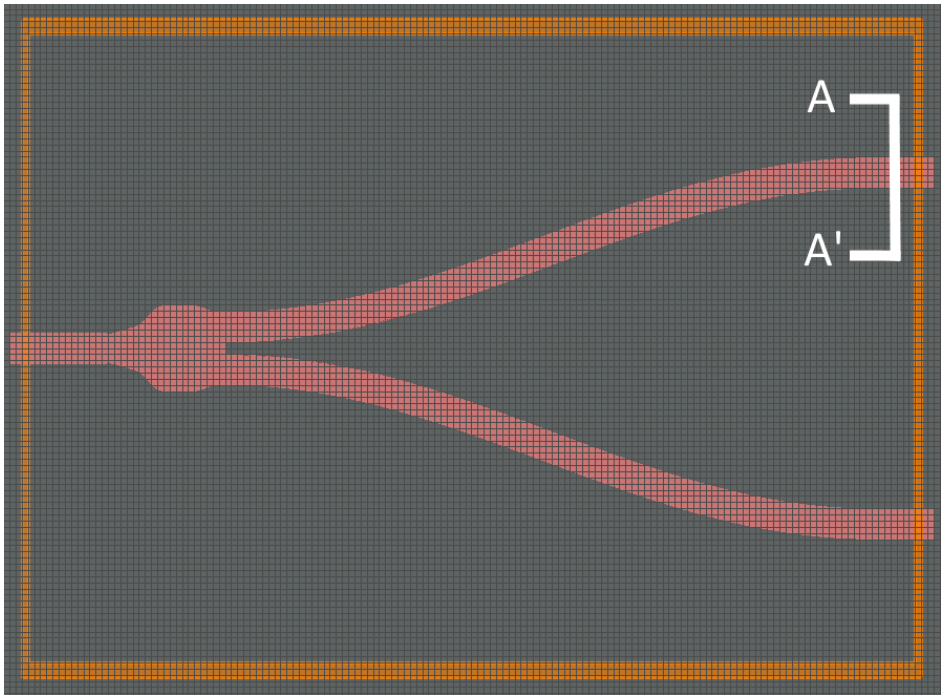


(a) Location of the cross-sectional slice.

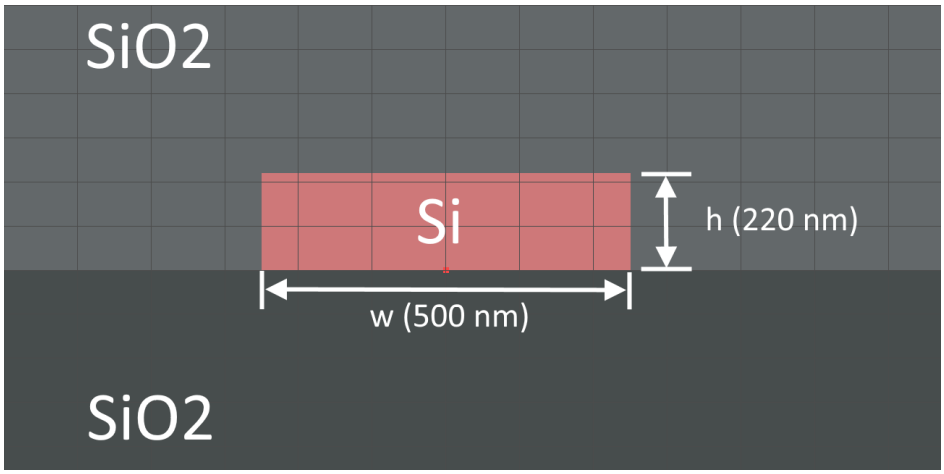


(b) Cross-sectional slice (from A to A') and identified parameters.

Figure 2.1: Top and cross sectional views of the Y-branch device. The process variations that this thesis focuses on are identified in Figure 2.1b.

Since the Y-branch component design is complicated due to its shape and function, there are multiple geometric parameters that can vary in this Y-branch structure. We consider a number of these parameters in this thesis; these are indicated in Figure 2.1b. The waveguide thickness can vary, and each of the output branch waveguide widths can also vary. It is also possible for the input waveguide width to vary. Finally, the taper width can also change.

These geometric variations alone can yield five different input parameters to perturb in simulation. Any combination of these input parameters can change the device operation; a robust device or circuit design would take the worst cases of these perturbations into account to ensure proper operation across the range of these variations.

The device can be made using any photonic waveguide process. Since this thesis focuses on silicon photonics, a standard Silicon-on-Insulator process is used when creating the device in simulation. This process is described in Section 2.2.

### 2.3.2 Directional Coupler

A top view of the directional coupler device is shown in Figure 2.2a. Used as a splitter, his device is designed to propagate and split input light into two different waveguides. Unlike the Y-branch, which uses a specialized taper shape to split the light, the directional coupler device leaks light from one waveguide into the other. The two waveguides are laid out to be close together, and evanescent light couples from one waveguide to the other. This distance between waveguides is referred to as the coupling gap ($L_g$). As the light propagates between the two waveguides along a certain distance (known as the coupling length, $L_c$), the modes of light oscillate between the two waveguides. These oscillating modes of light are known as 'supermodes" [28]. The phase difference in the supermodes that oscillate between the two waveguides determines the amount of power that is coupled to the secondary waveguide. It is possible to change the intensity of the light that comes out of the secondary waveguide by changing the coupling length of the two waveguides and the coupling gap between the two [11]. The desired ratio of light splitting is achieved by selecting the coupling length as well as the coupling gap. More details on the device operation can be found in Section 3.3.2 as well as in Yamada, et al. [26].

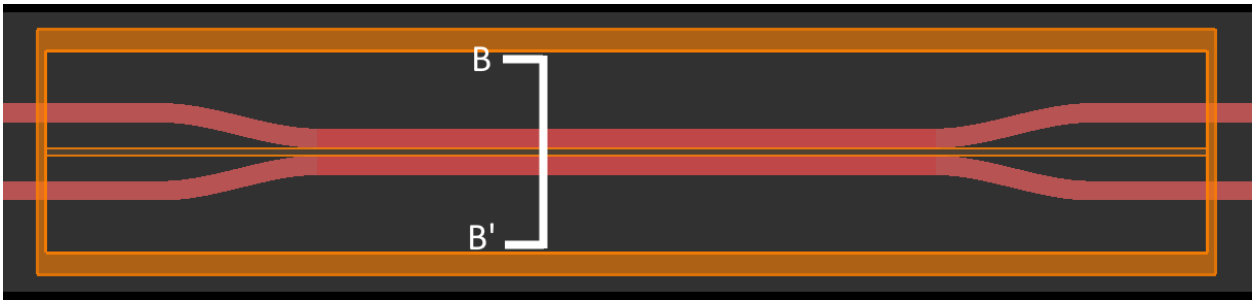


(a) Location of the cross-sectional slice.

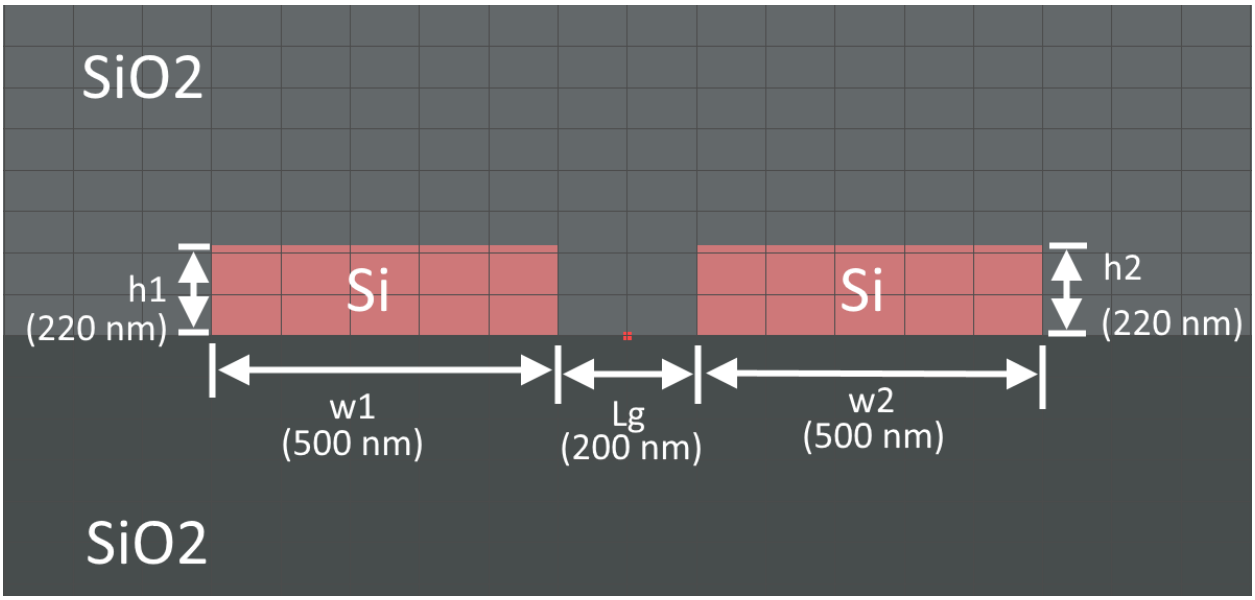


(b) Cross-sectional slice.

Figure 2.2: Top and cross sectional views of the directional coupler device. The process variations that this thesis focuses on are identified in Figure 2.2b.

The coupling length $L_c$ and coupling gap $L_g$ for our nominal coupler are chosen so that the device has a resonable power splitting ratio over the input free-space wavelength range of $\lambda = 1500$ to $1600\ nm$. For a given directional coupler design, the power splitting ratio is also a function of the input light wavelength. The 50/50 directional coupler device will only have an exact 50/50 splitting ratio at a certain wavelength, and it will deviate from this splitting ratio at other wavelengths. A device designer would choose the coupling length and coupling gap so that the 50/50 power splitting ratio is achieved at a desired operating wavelength. In our case, the nominal directional coupler seeks nearly 50/50 coupling at a wavelength of $1550\ nm$. This results in the following nominal values for these two parameters: $L_c = 16\ \mu m$

and $L_g = 200\ nm$.

There are multiple input parameters that can cause the directional coupler outputs to deviate from a desired power-splitting ratio. These parameters are identified in Figure 2.2. One parameter is the waveguide thickness. Since the directional coupler is created from two discrete waveguides, it is possible for both waveguide thicknesses to vary, either together or separately. The widths of each waveguide can also vary either together or separately. Finally, it is possible that the gap between the two waveguides can also vary. This variation can arise due to variations in the lithography and etching process used to form the waveguides. In the latter case, etching too much or too little of the silicon layer results in waveguides with different widths; for a fixed coupler layout, this also affects the coupling gap between the two waveguides. As with the Y-branch, we assume a nominal buried oxide thickness of 2 $\mu m$, and an overlying oxide with a planar surface and nominal thickness of 2 $\mu m$ over the exposed buried oxide.

## 2.4 Summary

This chapter has covered the necessary background knowledge to understand the compact modeling methods as applied to silicon photonics. The methods described in Chapters 3 and 4 depend on careful selection of variation test points. The design of experiments method is suggested as a systematic process for selecting the variation test cases; the experiment designs that are used in later chapters of this thesis are explained in detail. Further, background information on the Y-branch and directional coupler devices is presented. The basic device operation is explained; device parameters that can vary due to the manufacturing process are described. The devices explained in this chapter are used to demonstrate the compact modeling methods described in later chapters of this thesis.

# Chapter 3

# Compact Models Based on Corner Analysis Method

In order to create variation-aware compact simulation models, it is necessary to first construct a scheme for defining the variations that one will test. The aim is to describe a particular photonic device and/or the fabrication process for that device as a system. This system can be defined as having some inputs that affect the overall operation of the device at its outputs. This input-output system behavior can be described at some number of discrete combinations of inputs, or by way of parameteric or mathematical descriptions. By mathematical, we mean a functional relationship mapping process variations $p_i$, geometric or other device design variables $d_j$, and potentially photonic operating condition variables $x_u$ as inputs, to some output variables $y$ (such as field or power intensities at device ports). Some mathematical models may be quite complex and require numerical solutions. Other simplified compact models might be low order polynomial functions, as will be described in Chapter 4. In the former discrete inputs case, a set of tests are conducted where the inputs are chosen in a systematic way for each test. In manufacturing, a design of experiments typically determines the set of test points, usually to cover a desired range of parameter variations. The results of each test are taken to form a compact model in the form of a

finite set of input-output cases or points. The variations that cause the largest deviation from a desired behavior are considered the "worst cases." The subset of these cases can also be combined into or referred to as a variation compact model; using these multiple corner models, a photonic system design can be quickly evaluated for robustness to manufacturing variations.

The proposed design methodology of the corner analysis method is as follows:

1. Determine a set of parameters to test. Each parameter needs to affect device operation in some way. These are the variation test parameters. These might include process parameters $p_i, i = 1, ..., k$; device design parameters $d_j, j = 1, ..., m$; or operating inputs $x_u, u = 1, ...w$.

2. Determine the design of experiments to use based on the number of parameters being tested, the range of variation to be considered, and the expected relationship to device outputs.

3. Manufacture or simulate the experiments specified by the design of experiments to obtain the device responses with respect to the variation parameters chosen.

4. Depending on the design criteria, the entire set of experiment results can be used as a corner-based compact model; alternatively, the results from the largest deviations from the typical device operation (the "worst-case variations") can be used as a model.

## 3.1 Corner Analysis Method

The corner analysis method of compact modeling uses the design of experiments method outlined in Section 2.1.1 to define a set of simulation cases that explore or represent the worst-case operation of a device. These worst-case simulations are lumped together into a simulation model that can be used for further analysis, e.g., by running photonic compact circuit simulations at various selected corners or input-output cases.

There are two ways to define what the term "worst-case" means in the context of device compact models. The "worst-case" models can represent the worst possible *input* parameters and their respective output behavior. These corner models are referred to as the "worst-case input corners." There is another way to represent worst-case modeling; the "worst-case output corners" can represent the worst possible *output* behavior and the input parameters that cause them. Both models are desired in the simulation of larger systems. A photonic circuit design can be tested with the worst-case input corner models. This type of simulation informs the designer on whether or not the design is robust to the full range of possible process variations. Another simulation that uses the worst-case output corner models will produce a result that informs the designer on the overall worst-case operation of the design.

In both corner modeling cases, a design of experiments is carried out. Variation parameters that are hypothesized to affect device performance are selected to be modified. A central or nominal case is chosen to evaluate the device performance when no variation is present. This nominal case is then used as a point of comparison to measure the effects of variation, or output performance deviation with respect to the nominal. Each variation test point is determined using a variation estimate; for example, the variation parameters might change by $\pm 5\%$ of their nominal value. Then, the parameters of each variation test point are applied and the operation of the device is tested.

There are two ways to determine the output effects of the input variations on the device. One method is to construct the devices on a silicon wafer and test them. Each device can be manufactured to have intentional deviations from the nominal incorporated in their design. For example, a designer could create a test design that contains a set of devices that all have offsets in the designed parameters that mimic the possible combinations of deviation in that parameter. These offsets could be changes in waveguide thickness and waveguide width, for example. The design would then be manufactured, and the completed dies from the same manufacturing run would be tested. This method is advantageous because it will inform both the process engineers and device modeling engineers on the following:

1. which variations will affect the operation of the manufactured photonics devices,

2. the sensitivity of device operation to each variation, and

3. realistic measurements of device performance.

However, it is costly to fabricate wafers in the SOI process as of the time of this writing [22].

Another method to determine the effects of variations on a photonic device is to leverage computational power and simulate the operation of the photonics devices. In this thesis, it is desired to simulate the devices using Finite-Difference Time Domain simulation software. This software can simulate the electric and magnetic fields in the device by solving Maxwell's equations. One advantage is speed; an FDTD simulator can evaluate a DoE on a particular device in less time than a photonics wafer can be manufactured and prepared for testing. FDTD software can determine the output behavior of a device across a range of optical frequencies or wavelengths and express the results through the use of S-parameter descriptions. This simulation method is used to generate the results in this thesis and to demonstrate the compact modeling methods described here.

In either method, S-parameters are used as outputs for compact modeling of device variations. S-parameters are a linear, time-invariant description of the complex-valued electric and magnetic fields of a device at specified input and output port locations, and are appropriate for the passive devices considered in this thesis. S-parameters are defined in terms of their magnitude and phase because it is assumed that the electric and magnetic fields are in the form of complex exponentials. They are defined with respect to the electric and magnetic fields of a particular port. For example, if a device has two ports labeled 1 and 2, then $S_{12}$ describes the output of port number 2 with respect to port number 1. S-parameters can be used to simulate optical performance of a device in a photonic circuit simulator. Lumerical INTERCONNECT, a photonic circuit simulator that is used to create these compact models, can use S-parameter representations of photonic devices for simulation.

Each device has different geometric parameters that contribute to variation in the out-

put performance. In silicon photonics, the waveguide thickness and waveguide widths are common geometric parameters that affect performance. These parameters change the cross-section of the waveguide, which impacts the effective index of the waveguide [17].

A corner model formed using only the $2^k$ factorial design results is called a multivariate corner model. Another type of corner model that can be constructed uses the "one-at-a-time" variations or results from testing one parameter perturbation at a time. The resulting simulation compact model is referred to as a univariate corner model.

## 3.2 Y-Branch Model

The corner-based modeling method is demonstrated in this thesis for two different passive photonics devices. The Y-branch is the first device that the method is tested on, with the advantage that it is relatively simple to understand the effects that device variations have on the output. If the variations result in an imbalanced Y-branch geometry, then the device performance is also similarly imbalanced. The device is also modeled because it is a building block component used in the construction of many photonic circuits, inlcuding Mach-Zehnder Interferometers. The MZI is a simple photonic circuit that is used in examples in Chapter 5 to evaluate the effects of device variations on a larger design.

In this section, the procedure for creating a compact corner model for a Y-branch device is demonstrated. First, the simulation setup and the nominal device operation is described. Then, the results of simulation of the design of experiments are presented. Finally, the method of creating corner models for the Y-branch is demonstrated.

### 3.2.1 FDTD Simulation Setup

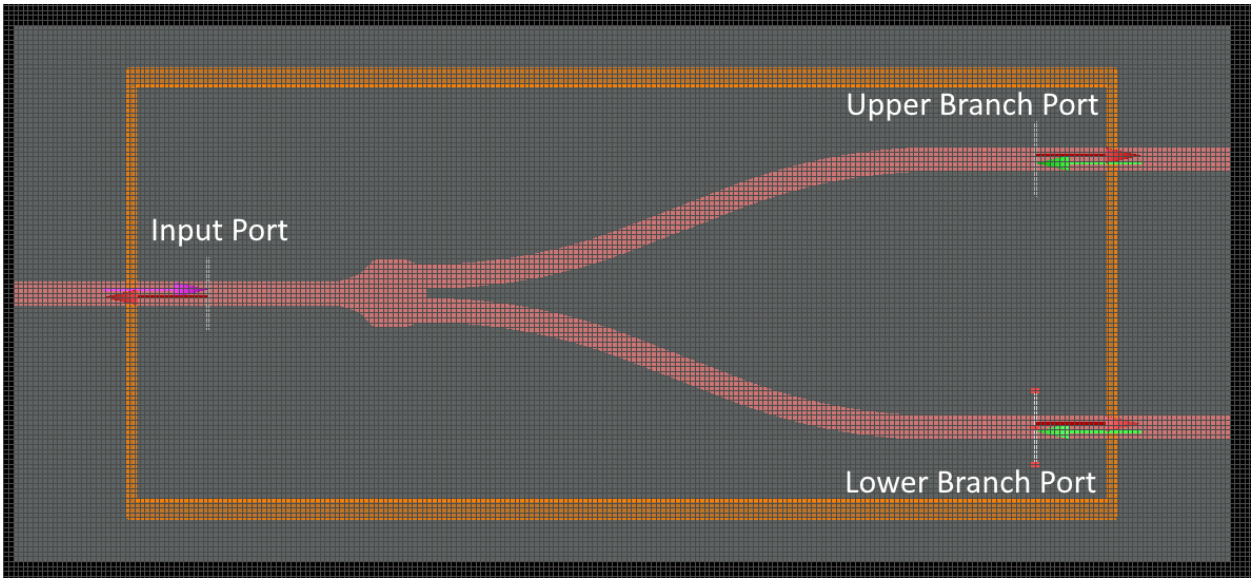


Figure 3.1: A typical Y-Branch device simulation configuration in Lumerical FDTD.

A typical FDTD simulation setup is shown in Figure 3.1. The Y-branch is a three port device. For the purposes of discussion, the ports are labeled as follows:

- The left port is called the "Input" port. Theoretically, any of the three ports can be chosen as a source of light. To simulate the Y-branch as a light-splitting device, the light source is placed here. The port is numbered as Port 1 in simulation.
- The top right port is called the "Upper Branch" port. This port measures the power that is transmitted through the top waveguide after light passes through the junction taper. The port is numbered as Port 2.
- The bottom right port is called the "Lower Branch" port. This port measures the power that is being transmitted through the bottom waveguide after light passes through the junction taper. The port is numbered as Port 3.

We use scripts in Phoenix OptoDesigner to implement the Y-branch. This enables different instantiations of the device geometry for each combination of parameters under consideration. These scripts generate GDS-II files with the desired changes in the output branch

waveguide widths. The modified layouts are then imported to Lumerical FDTD and the desired waveguide thickness is applied in the simulation setup. To automate the process of running multiple simulations, the S-parameter Sweep function is used in Lumerical FDTD. This function automatically runs a simulation for every port in the device; results from running all simulations are then exported as S-parameter files and/or as .mat files to be used in MATLAB. All device simulations are run with a mesh accuracy setting of 8 to obtain results with the highest simulation accuracy.

### 3.2.2 Nominal Device Operation

The nominal operation of a typical Y-branch device is demonstrated in Figure 3.2. The measured results in simulation is comparable to that of Zhang, et al. [25]. In the nominal case, the upper and lower branches transmit the same amount of power over the wavelength range of $\lambda = 1500$ to 1600 $nm$. In an ideal case, the transmitted power across both branches would be 0.5 across all wavelengths. However, there are power transmission losses due to light reflecting back to the input or scattering out of the structure. These losses come from the taper shape and cannot be completely eliminated in a realistic operating scenario. Nevertheless, the amount of power loss due to these back-reflections can be minimized by changing the shape of the taper. In [25], the particular taper shape is designed with this in mind; it is shaped so that the back-reflections of the device are minimized at $\lambda = 1550$ $nm$. One consequence is that the output power at each of the two ports will be roughly constant from the range of 1550 to 1600 $nm$. Silicon photonics typically uses light at a free-space wavelength of 1550 $nm$, so this nominal design serves as a reasonable starting point.

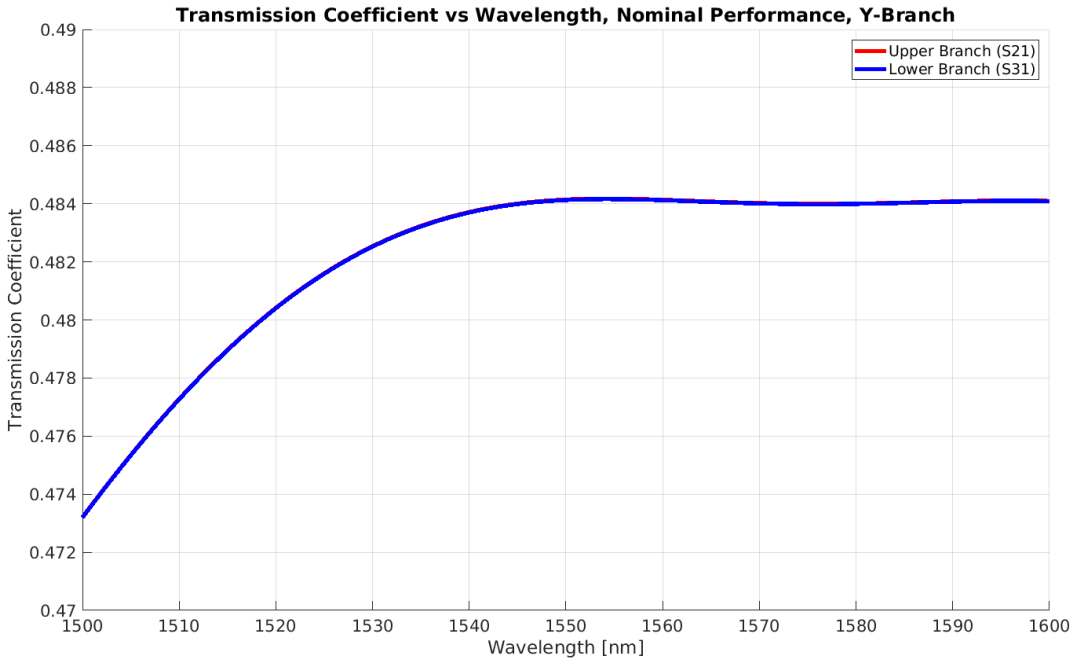


Figure 3.2: The power transmitted through the output ports of the nominal Y-branch device design, normalized to the input port power.

### 3.2.3 Results from DoE Simulation

For the Y-branch, three variation parameters are selected: waveguide thickness (denoted as $h$) and waveguide widths of the upper and lower output branches (denoted as $w_1$ and $w_2$, respectively). The waveguide thickness is varied across the entire device, while the modified waveguide widths are limited to only the specific waveguide branch that is perturbed. A central composite factorial design ($2^k$ corners, nominal, and axial cases), as described in Section 2.1.2 of the thesis, is used to determine the combinations of input variations to test. The parameters are modified using the variation scheme listed in Table 3.1. These variation schemes change the parameters by $\pm 5\%$ of the nominal value.

| Parameter | Low Value | Nominal | High Value |
|---|---|---|---|
| Upper Branch WG Width, $w_1$ | 475 nm | 500 nm | 525 nm |
| WG Thickness, $h$ | 209 nm | 220 nm | 231 nm |
| Lower Branch WG Width, $w_2$ | 475 nm | 500 nm | 525 nm |

Table 3.1: DoE parameters tested on Y-branch. Parameter variations are ±5% of the respective nominal value

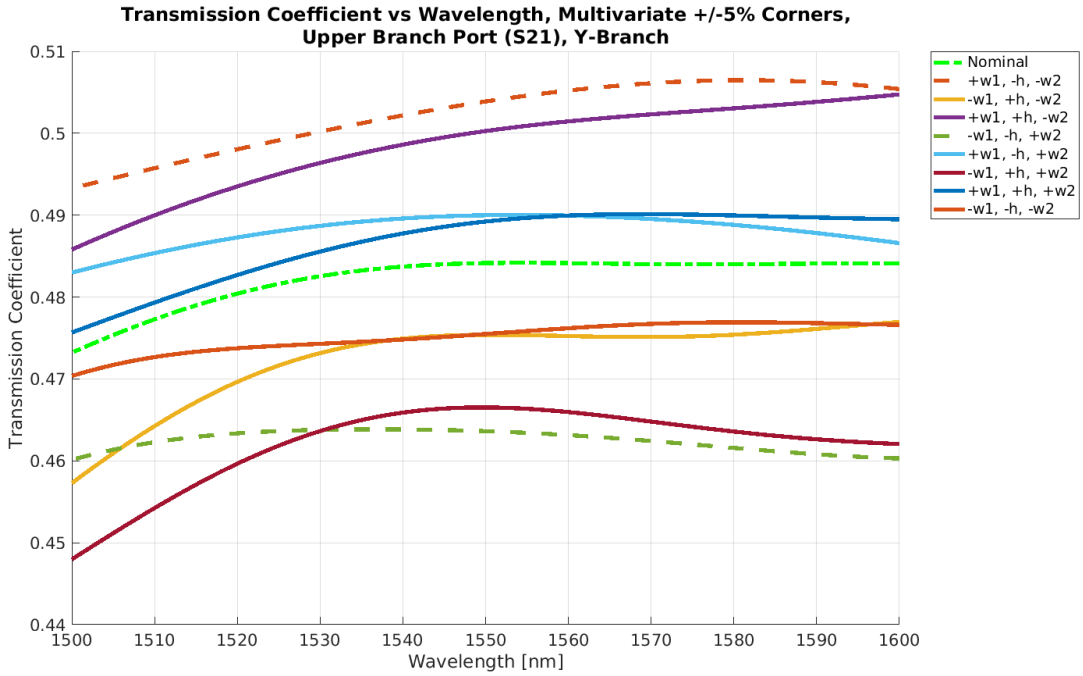


(a) Upper Branch.

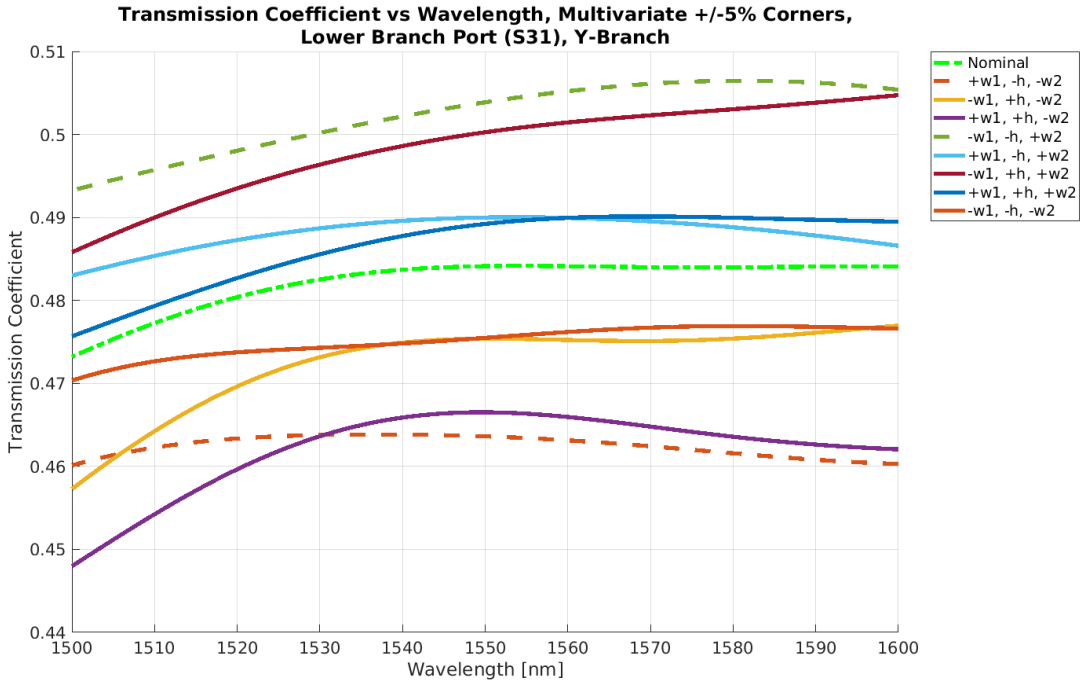


(b) Lower Branch.

Figure 3.3: The relative power transmitted through the branches of the Y-branch due to multiple variations applied at once. The specific values applied in each test are listed in Table 3.1, representing deviations that are ±5% of the nominal. Worst case outputs at 1550 nm are shown as dashed lines.

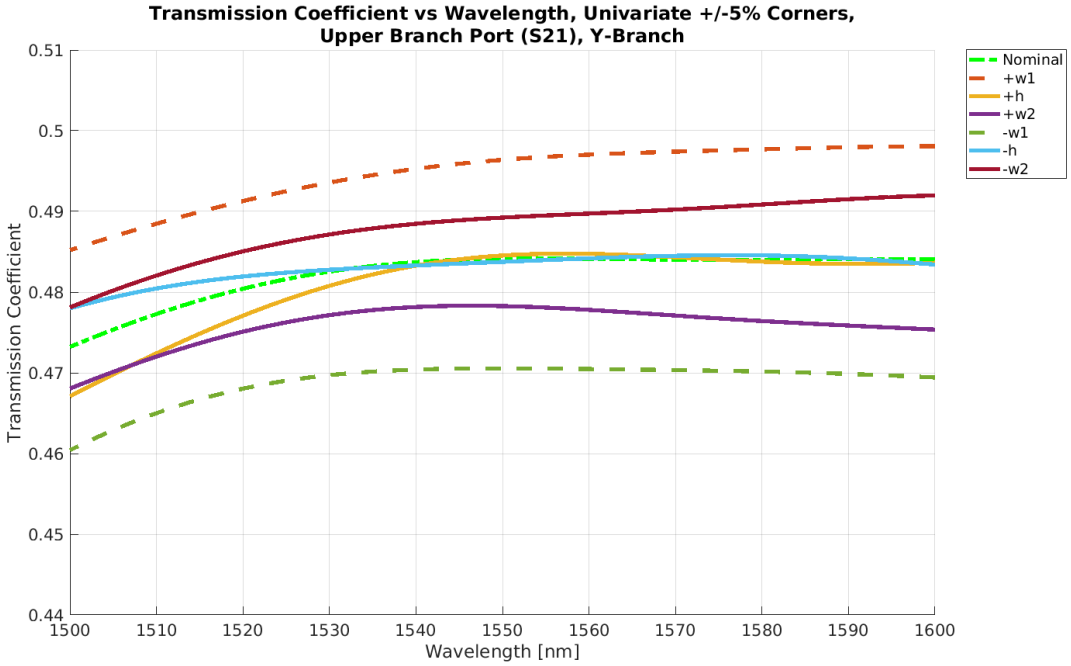


(a) Upper Branch.

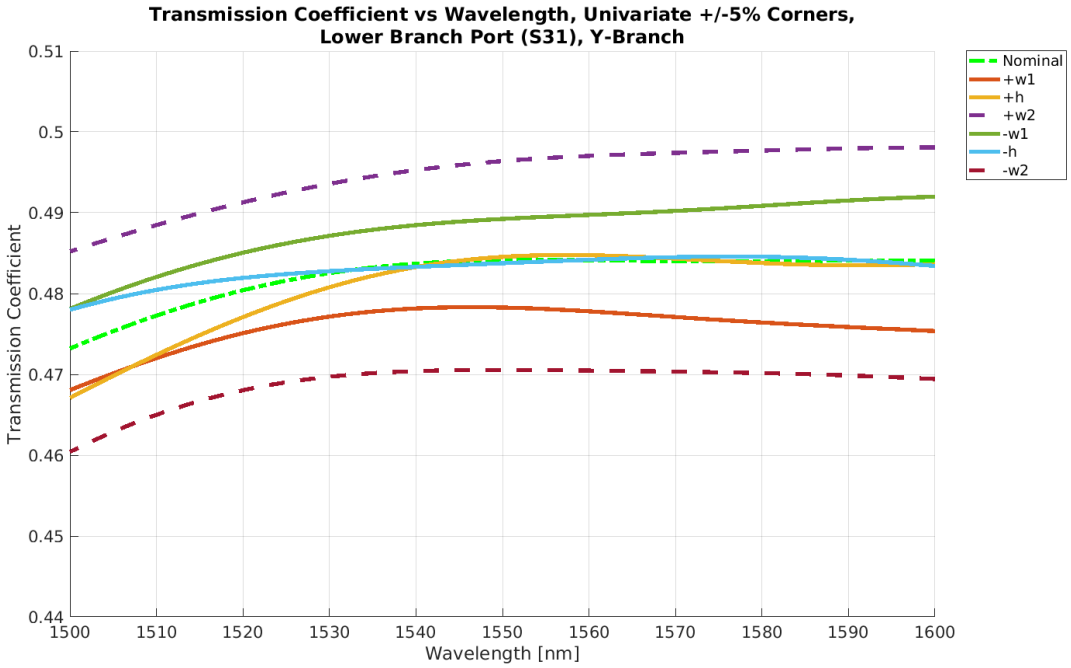


(b) Lower Branch.

Figure 3.4: The relative power transmitted through the branches of the Y-branch due to one variation applied at a time. The specific values applied in each test are listed in Table 3.1, representing deviations that are ±5% of the nominal. Note that the univariate worst cases (dashed lines) are within the ranges observed for multivariate worst cases seen in Figure 3.3.

The results of testing ±5% variations in these three parameters are shown in Figures 3.3 and 3.4. From these results, it is determined that the worst-case corners are the cases where $w_1 \neq w_2$ and $h = 209\ nm$. These are the cases that are on the upper and lower extremes of the transmission coefficient at 1550 $nm$, and are shown as dashed lines in the figures. For example, the case where $w_1 = 525\ nm$ and $w_2 = 475\ nm$ results in maximizing the output power coming out of the upper branch while simultaneously minimizing the output power coming out of the lower branch. This initial corner analysis confirms that the Y-branch output performance is affected by asymmetry between the two branches. This geometric asymmetry introduces an unbalancing effect where more light passes into the larger of the two branches. Increasing the thickness of the output waveguides helps mitigate the effects of asymmetry; in the cases where $h = 231\ nm$, the difference in output power between the two branches is reduced.

Figure 3.4 shows the effect of applying one variation at a time. In these test cases, the single input parameter that affects device performance the most is dependent on the branch that is being measured. In the upper branch (shown in Figure 3.4a), $w_1$ affects performance the most; this is the waveguide width of the upper branch. Changing the width of the lower branch results in a smaller power output change in the upper branch. Similarly, the lower branch performance (shown in Figure 3.4b) is affected the most by $w_2$, which is the corresponding waveguide width.

Table 3.2 summarizes the worst-case corners in each output of the Y-branch. The table lists the worst-case output performance corners as a function of the input corners. The term "H" corresponds to the input value taking on the larger of the two test values (in this case, this refers to the +5% value), and the term "L" corresponds to the value taking on the smaller of the two test values (in this case, this refers to the −5% value). These identified test cases are what would typically make up a worst-case output corner model.

| Output Performance Case | Value at $\lambda = 1550nm$ | $w_1$ | $h$ | $w_2$ |
|---|---|---|---|---|
| Upper Branch Port Transmission Max (H) | 0.504 | H | L | L |
| Upper Branch Port Transmission Min (L) | 0.464 | L | L | H |
| Lower Branch Port Transmission Max (H) | 0.504 | L | L | H |
| Lower Branch Port Transmission Min (L) | 0.464 | H | L | L |

Table 3.2: Summary of the worst-case output corners of the Y-branch. In this case, the number of parameters changed is three. Parameter variations are ±5% of the respective nominal value.

A tighter set of variations on the same three parameters is also tested. The DoE that is used is the same as in the previous section, but instead of varying each test parameter by ±5% of the nominal value, they are varied by ±1% of the nominal. These experiments are run to determine whether the specific parameters $p_i$ continue to have the same sensitivity impact $\frac{\delta y}{\delta p_i}$ on device performance. The variations chosen for this set are listed in Table 3.3.

| Parameter | Low Value | Nominal | High Value |
|---|---|---|---|
| Upper Branch WG Width, $w_1$ | 495 nm | 500 nm | 505 nm |
| WG Thickness, $h$ | 217.8 nm | 220 nm | 222.2 nm |
| Lower Branch WG Width, $w_2$ | 495 nm | 500 nm | 505 nm |

Table 3.3: DoE parameters tested on Y-branch. Parameter variations are ±1% of the respective nominal value.

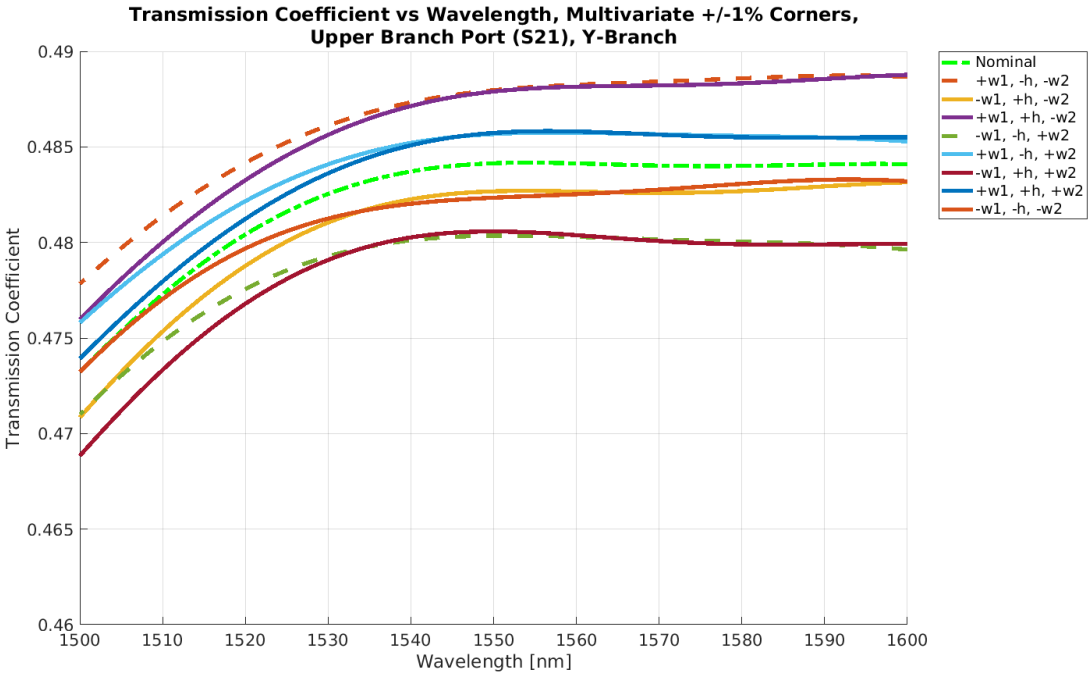


(a) Upper Branch.

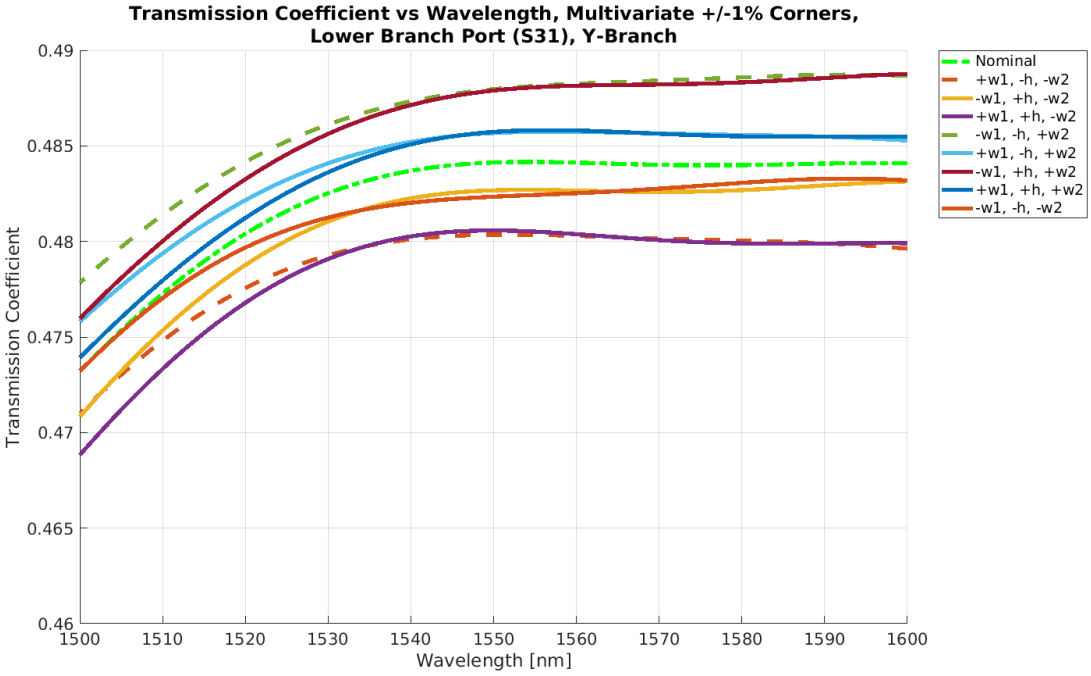


(b) Lower Branch.

Figure 3.5: The relative power transmitted through the output branches of the Y-branch due to multiple variations applied at once. The specific values applied in each test are listed in Table 3.3, now covering deviations that are ±1% of the nominal.

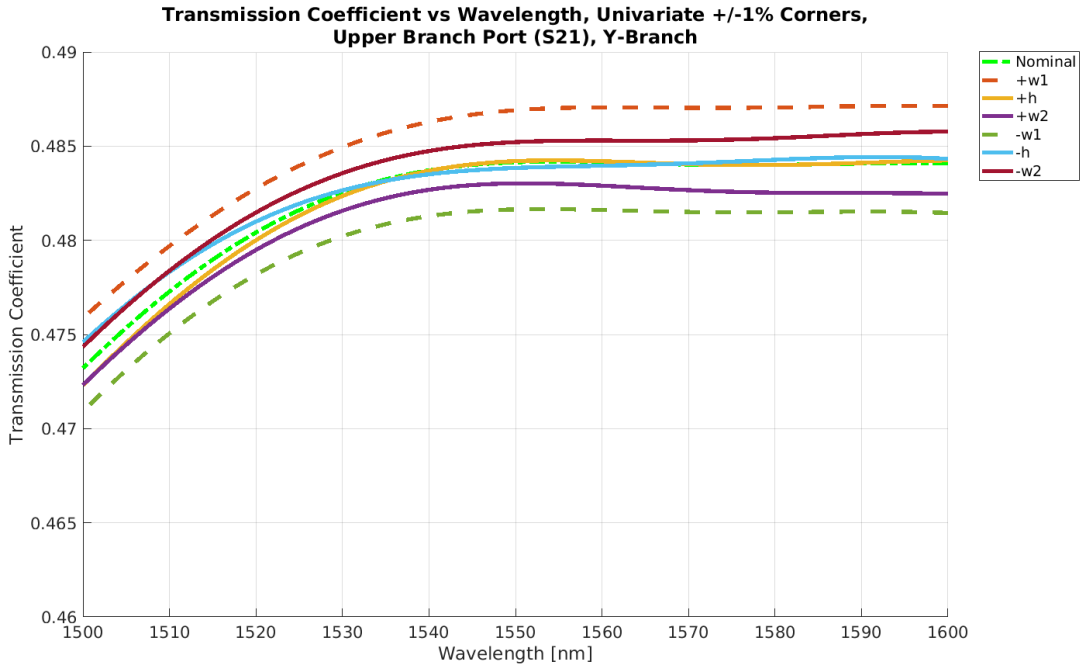


(a) Upper Branch.

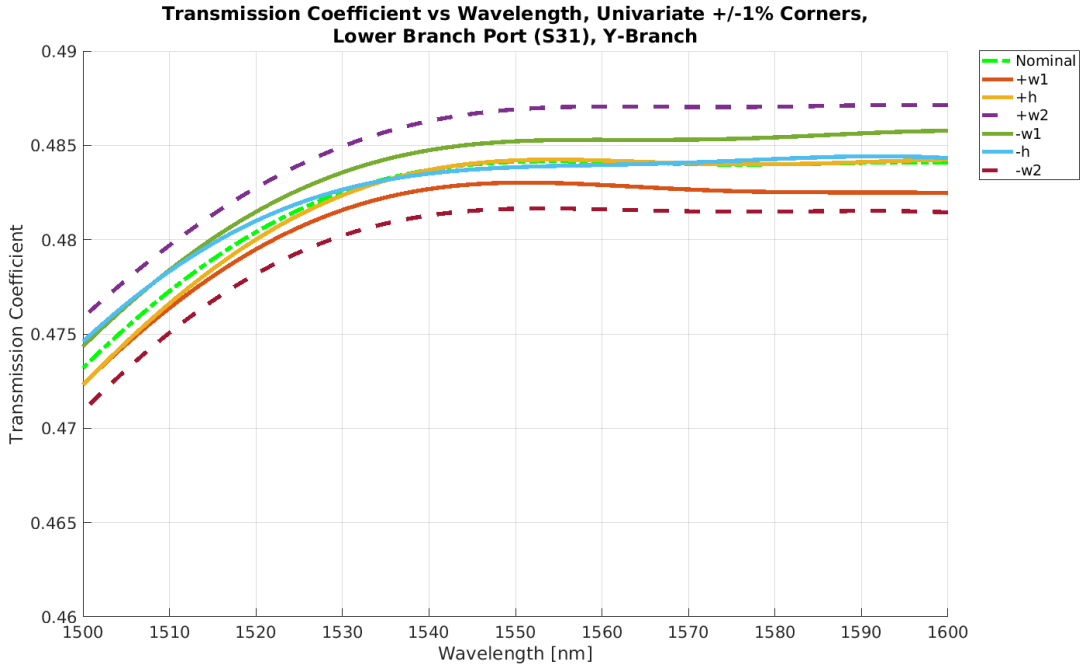


(b) Lower Branch.

Figure 3.6: The relative power transmitted through the branches of the Y-branch due to one variation applied at a time. The specific values applied in each test are listed in Table 3.3, now covering deviations that are ±1% of the nominal.

The results of testing the 1% variations are shown in Figures 3.5 and 3.6. From these

results, it is determined that the worst-case corners are again the cases where $w_1 \neq w_2$ and $h = 217.8\ nm$. These are the cases that are indicated as dashed lines in Figure 3.5. For example, the case where $w_1 = 505\ nm$ and $w_2 = 495\ nm$ results in maximizing the output power coming out of the upper branch while simultaneously minimizing the output power coming out of the lower branch. These correspond to the same worst-case corners as previously found in the ±5% design of experiments, which further supports the claim that the Y-branch output performance is affected by asymmetry between the two branches. As in the previous corner analysis case, increasing the thickness of the output waveguides helps mitigate the effects of asymmetry. In the experiment cases where $h = 222.2\ nm$, the difference in output power between the two branches is reduced.

Figure 3.6 shows the effect of applying one variation at a time. In these test cases, the input parameter that affects device performance the most is again dependent on the branch that is being measured. In the upper branch (shown in Figure 3.6a), $w_1$ affects performance the most; this is the waveguide width of the upper branch. As before, changing the width of the lower branch results in a smaller power output change in the upper branch. Similarly, the lower branch performance (shown in Figure 3.6b) is affected the most by $w_2$, which is the corresponding waveguide width.

Table 3.4 summarizes the worst-case corners in each output of the Y-branch, now for ±1% input variations. As in Table 3.2, we find that the same input combinations for the ±1% input variations cases result in the extremal outputs.

| Output Performance Case | Value at $\lambda = 1550nm$ | $w_1$ | $h$ | $w_2$ |
|---|---|---|---|---|
| Upper Branch Port Transmission Max | 0.488 | H | L | L |
| Upper Branch Port Transmission Min | 0.480 | L | L | H |
| Lower Branch Port Transmission Max | 0.488 | L | L | H |
| Lower Branch Port Transmission Min | 0.480 | H | L | L |

Table 3.4: Summary of the worst-case corners of the Y-branch. In this case, the number of parameters changed is three. Parameter variations are ±1% of the respective nominal value.

### 3.2.4 Sensitivity Analysis

In addition to constructing a worst-case compact model, the results of a corner analysis are typically used to determine and quantify how the Y-branch operation changes as the input parameters change. The corner analysis test cases examine operation changes at certain input test cases that are 5 to 25 $nm$ away from the nominal parameter values for thickness and branch widths. However, the exact values tested using that method may not be consistent with one another; the test widths that are $\pm 5\%$ from nominal (475 $nm$ and 525 $nm$) are differently spaced from the corresponding test thicknesses (209 $nm$ and 231 $nm$). A sensitivity analysis allows for a closer examination of the effect of changing the input process variations. To quantify these effects, we measure the sensitivity of the output performance of the device to each input, $\frac{\delta y}{\delta x_k}$, where $y$ denotes the output performance of the device and $x_k$ refers generically to any input parameter, whether process variation $p_i$, device design parameter $d_j$, or operating condition $x_u$. The univariate results are used to estimate this sensitivity by taking the discrete difference:

$$\left.\frac{\delta y}{\delta x_k}\right|_{+5\%} \approx \frac{y_{nom} - y_{+5\%}}{x_{k,nom} - x_{k,+5\%}}, \tag{3.1}$$

$$\left.\frac{\delta y}{\delta x_k}\right|_{-5\%} \approx \frac{y_{nom} - y_{-5\%}}{x_{k,nom} - x_{k,-5\%}}, \tag{3.2}$$

$$\left.\frac{\delta y}{\delta x_k}\right|_{+1\%} \approx \frac{y_{nom} - y_{+1\%}}{x_{k,nom} - x_{k,+1\%}}, \tag{3.3}$$

$$\left.\frac{\delta y}{\delta x_k}\right|_{-1\%} \approx \frac{y_{nom} - y_{-1\%}}{x_{k,nom} - x_{k,-1\%}}. \tag{3.4}$$

The discrete difference is found using responses to the positive and negative deviation points, at $\pm 5\%$ or $\pm 1\%$ of nominal, respectively. This will give insight on whether the sensitivity is constant across the parameter space. If the sensitivity is not constant, then it is possible that the relationship between that variation parameter and the output performance is better approximated with a polynomial representation. Chapter 4 provides more details on

modeling this input-output relationship using a response surface.

Figures 3.7 and 3.8 visualize the sensitivity of the output performance of the Y-branch with respect to $w_1$, $w_2$, and $h$, respectively. The particular power transmission output is measured at $\lambda = 1550\ nm$. Note that sensitivity with respect to $w_2$ is identical to that seen in Figure 3.7, except with the upper and lower branch roles swapped, due to the symmetry of the device.

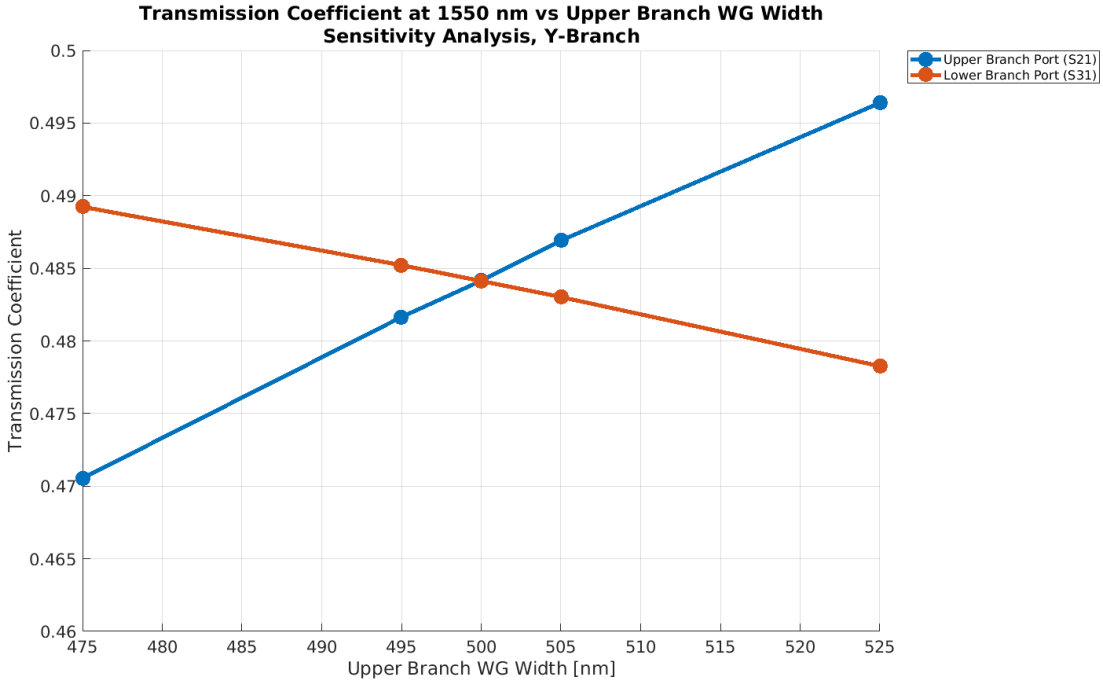


Figure 3.7: Sensitivity of Y-branch power transmission versus upper branch width measured at $\lambda = 1550\ nm$. The specific values applied in each test are listed in Tables 3.1 and 3.3.

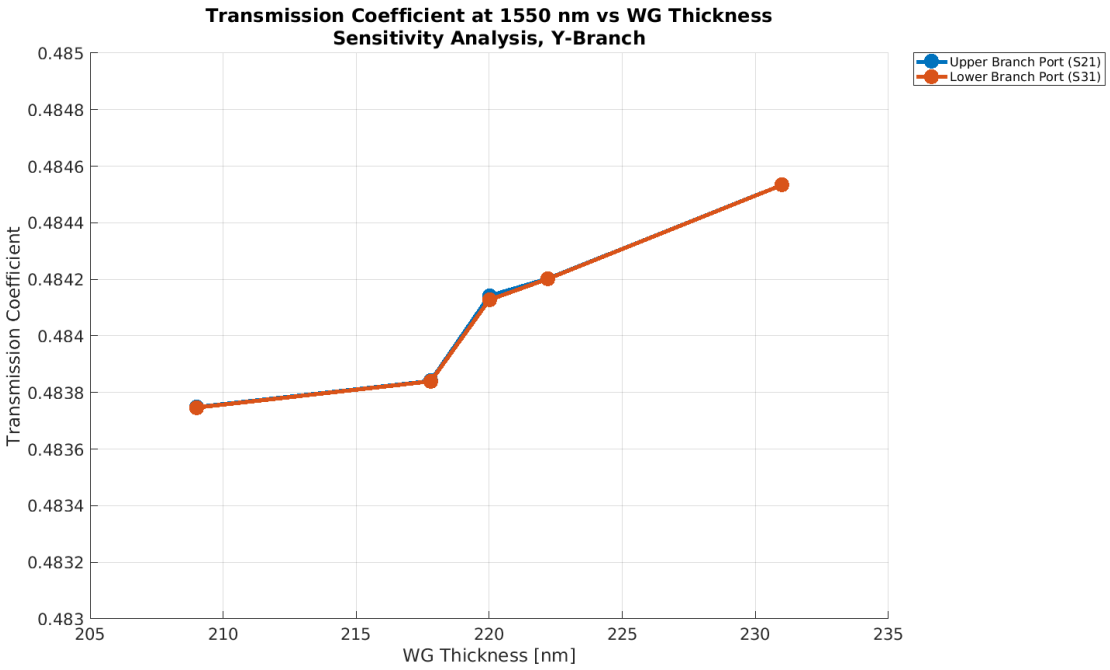


Figure 3.8: Sensitivity of Y-branch power transmission versus thickness measured at $\lambda = 1550\ nm$. The specific values applied in each test are listed in Tables 3.1 and 3.3.

| Sensitivity Parameter | -5% | -1% | +1% | +5% |
|---|---|---|---|---|
| $\frac{\delta\|S21\|^2}{\delta w_1}$ | $5.44 \cdot 10^{-4} \frac{1}{nm}$ | $5.00 \cdot 10^{-4} \frac{1}{nm}$ | $5.53 \cdot 10^{-4} \frac{1}{nm}$ | $4.90 \cdot 10^{-4} \frac{1}{nm}$ |
| $\frac{\delta\|S21\|^2}{\delta h}$ | $3.58 \cdot 10^{-5} \frac{1}{nm}$ | $1.37 \cdot 10^{-4} \frac{1}{nm}$ | $2.76 \cdot 10^{-5} \frac{1}{nm}$ | $3.56 \cdot 10^{-5} \frac{1}{nm}$ |
| $\frac{\delta\|S21\|^2}{\delta w_2}$ | $-2.04 \cdot 10^{-4} \frac{1}{nm}$ | $-2.15 \cdot 10^{-4} \frac{1}{nm}$ | $-2.24 \cdot 10^{-4} \frac{1}{nm}$ | $-2.35 \cdot 10^{-4} \frac{1}{nm}$ |

Table 3.5: Estimated sensitivity of the Y-branch due to the different parameters tested. Parameter variations are ±5% or ±1% of the respective nominal value.

Table 3.5 demonstrates estimates of the sensitivity of the power in each output branch with respect to the input parameter. The columns show which univariate case is used to calculate the corresponding sensitivity estimate. This can be thought of as the slope

between the two corresponding points in Figures 3.7 and 3.8. Note that due to device symmetry, $\frac{\delta|S31|^2}{\delta w_1} = \frac{\delta|S21|^2}{\delta w_2}$, $\frac{\delta|S31|^2}{\delta w_2} = \frac{\delta|S21|^2}{\delta w_1}$, and $\frac{\delta|S31|^2}{\delta h} = \frac{\delta|S21|^2}{\delta h}$. We see in Table 3.5 and in Figure 3.8 that waveguide thickness has substantial nonlinearity as a function of thickness (and resulting different sensitivites depending on the range of thickness deviation being considered). Methods for higher-order modeling to capture this dependence will be discussed in Chapter 4.

### 3.2.5 Compact Model Creation

A compact model is constructed after obtaining results from DoE simulation of the Y-Branch. This compact model is created using the Lumerical FDTD and INTERCONNECT software. An example illustrating the corner model in the context of a Mach-Zehnder Interferometer circuit is discussed further in Chapter 5.

## 3.3 Directional Coupler Model

In this section, the creation of compact corner models for a directional coupler device is discussed. First, the nominal device operation is demonstrated. Then, the results of DoE simulation are presented. Finally, the method of creating corner models for the directional coupler is demonstrated.

### 3.3.1 FDTD Simulation Setup

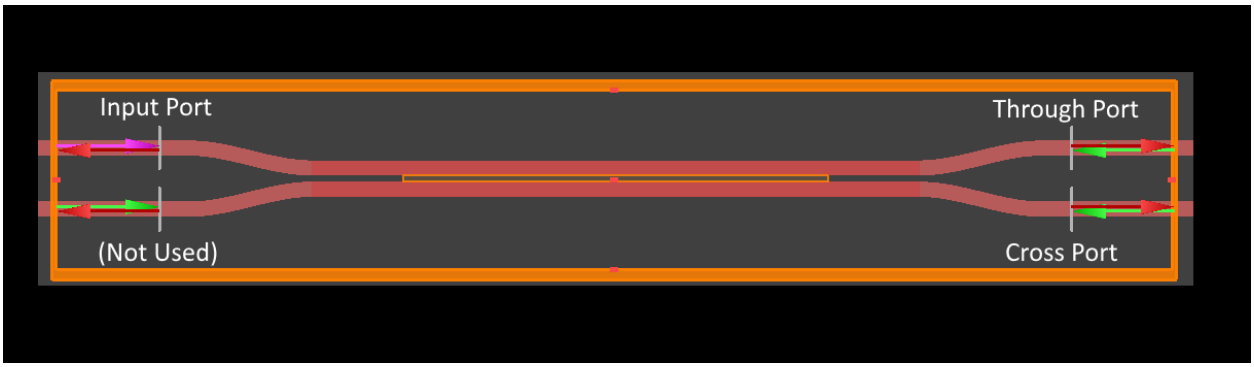


Figure 3.9: A typical directional coupler device simulation configuration in FDTD.

A typical FDTD simulation setup for the directional coupler is shown in Figure 3.9. For the purposes of discussion, the ports are labeled as follows:

- The top left port is called the input port. In simulating the device performance, any port can be chosen as a source of light because the device is symmetric. In simulation, this port is where the source of light is normally placed. The port is numbered as Port 1 in simulation.

- The bottom left port is a port that is normally not used when the directional coupler serves as a splitter. In simulation, a port is placed here to maintain the symmetry of the device. The port is numbered as Port 2 in simulation.

- The top right port is called the through port. This port measures the power that is being passed through the top waveguide via the input port. The port is numbered as Port 3.

- The bottom right port is called the cross port. The light from the top waveguide couples through the gap and into the bottom waveguide. Light from the coupling phenomenon can be measured at this port, numbered as Port 4.

As in Section 3.2, we use scripts in Phoenix OptoDesigner to implement the directional coupler, enabling different instantiations of the device geometry for each combination fo

parameters under consideration. As with the Y-branch simualtions in the previous section, to automate the process of running multiple simulations, the S-parameter Sweep function is used in Lumerical FDTD. This function automatically runs a simulation for every port in the device; results from running all simulations are then exported as S-parameter files and/or as .mat files to be used in MATLAB. All device simulations here are run with a mesh accuracy setting of 8 to obtain results with the highest simulation accuracy.

### 3.3.2 Nominal Device Operation

The nominal operation of the directional coupler is shown in Figures 3.10a and 3.10b. The device is broadband; the power splitting ratio changes as a function of the input light wavelength. A coupling length of $L_c = 16\ \mu m$ and a nominal coupling gap of $L_g = 200\ nm$ are selected so that the directional coupler has an even 50/50 power splitting ratio at a wavelength of $\lambda = 1560\ nm$. This means that 50% of the power from light at $\lambda = 1560\ nm$ will be transmitted in the through port, and the other 50% will be transmitted in the cross port, as indicated in Figure 3.10. Silicon photonics often uses light at a free-space wavelength of 1550 $nm$, so this nominal design serves as a reasonable starting point.

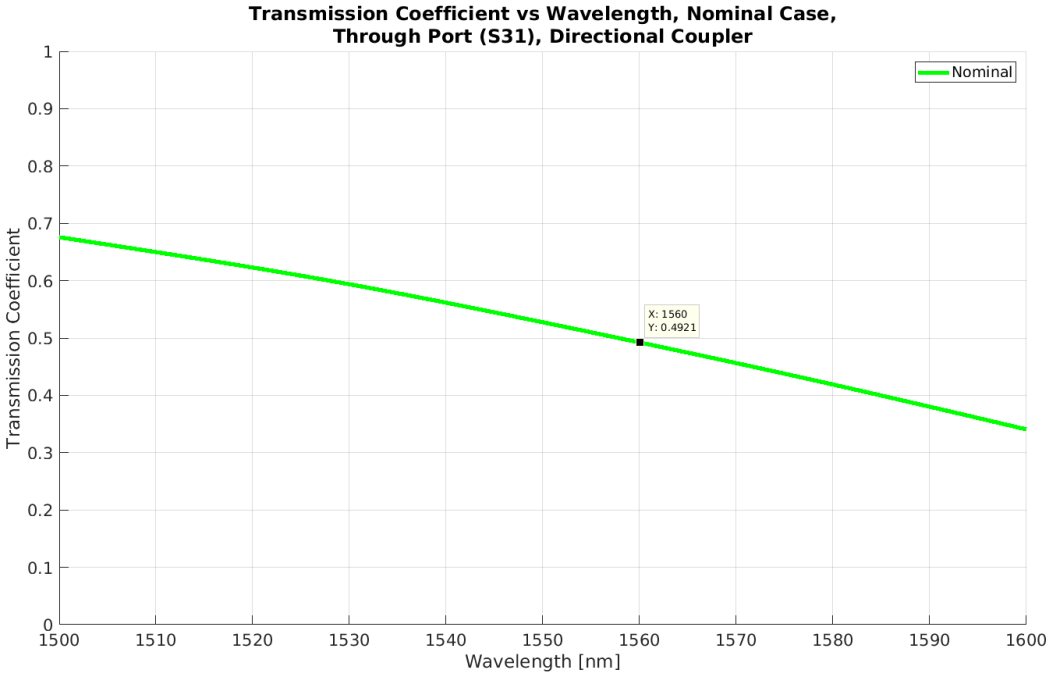


(a) Through port.

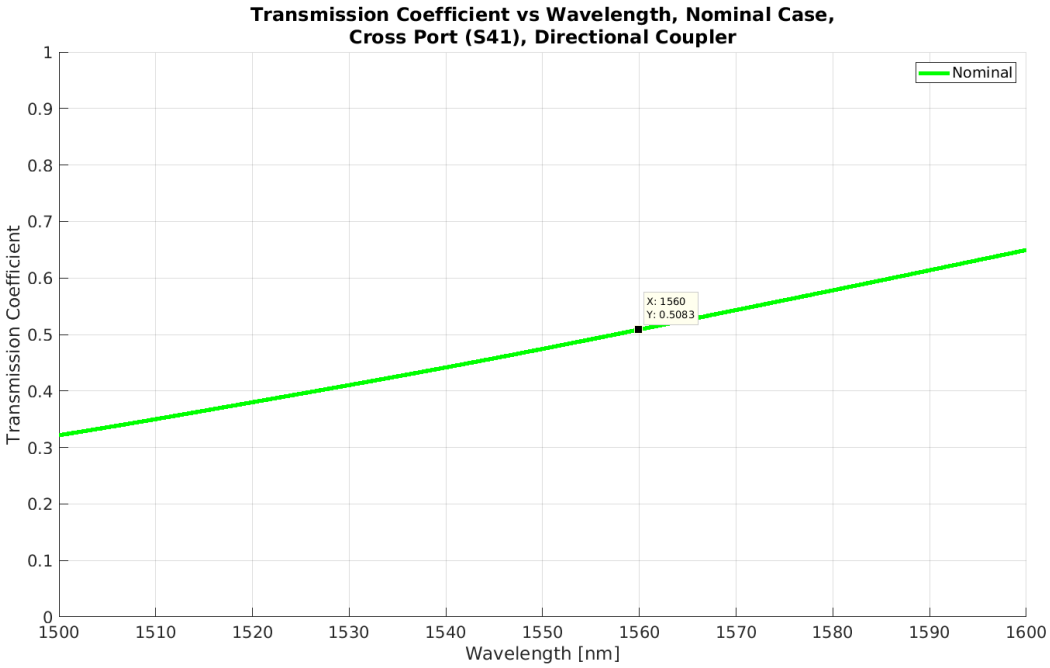


(b) Cross port.

Figure 3.10: The power transmitted through the different ports of the nominal directional coupler device design.

### 3.3.3 Results from DoE Simulation

This section discusses the results of various DoE corner simulations, applied to the directional coupler. A central composite design, as described in Section 2.1.2 of the thesis, is used to determine the combinations of input variations to test in each case of our directional coupler. The examples in this section cover two corner model cases where the number of input variations is modified. The first case, where the number of input variations is equal to three ($k = 3$), describes a directional coupler where the waveguide thickness and widths vary together; the parameters change together to simulate possible chip-to-chip variations. In the second DoE case, where the number of variations tested is equal to five ($k = 5$), the worst-case corners give rise to various possible cases of an asymmetrical directional coupler configuration.

#### Three-Parameter DoE

The parameters are first modified using the variation scheme listed in Table 3.6. This scheme assumes that process variations will result in larger or smaller waveguides. It also assumes that both waveguides within the coupler are affected by the changes simultaneously. In these cases, three parameters that define the geometry of the device are modified: waveguide thickness (denoted as $h$), waveguide width (denoted as $w$), and coupling gap (denoted as $L_g$).

| Parameter | Low Value (L, -) | Nominal | High Value (H, +) |
|---|---|---|---|
| Coupling Gap $L_g$ | 190 nm | 200 nm | 210 nm |
| WG Width $w$ | 475 nm | 500 nm | 525 nm |
| WG Thickness $h$ | 209 nm | 220 nm | 231 nm |

Table 3.6: DoE parameters tested on the directional coupler. In this case, three parameters defining the geometry of the device are changed. Parameter variations are ±5% of the respective nominal value.

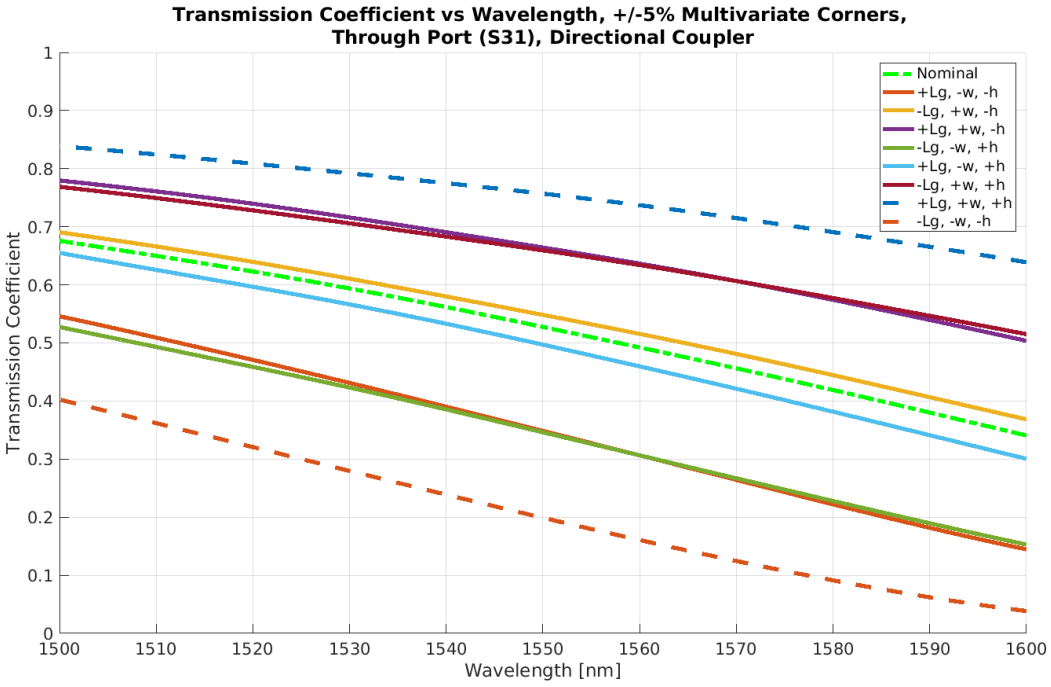


(a) Through port variations.

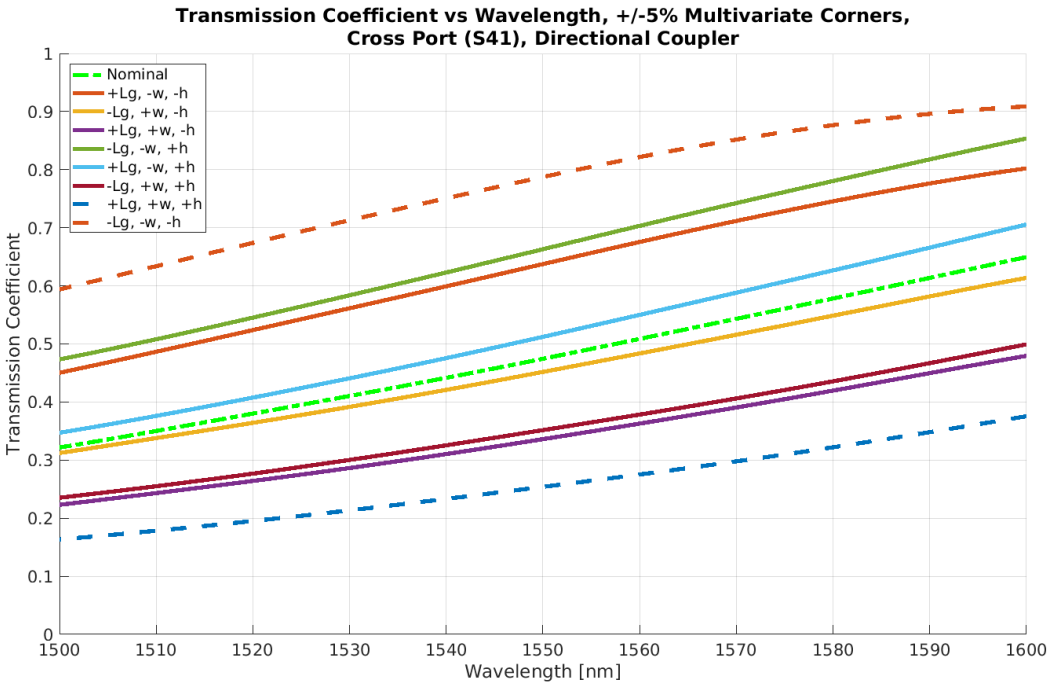


(b) Cross port variations.

Figure 3.11: The power transmitted in the ports of the directional coupler due to applying multivariate combinations of variations, as listed in Table 3.6, representing deviations that are ±5% of the nominal.

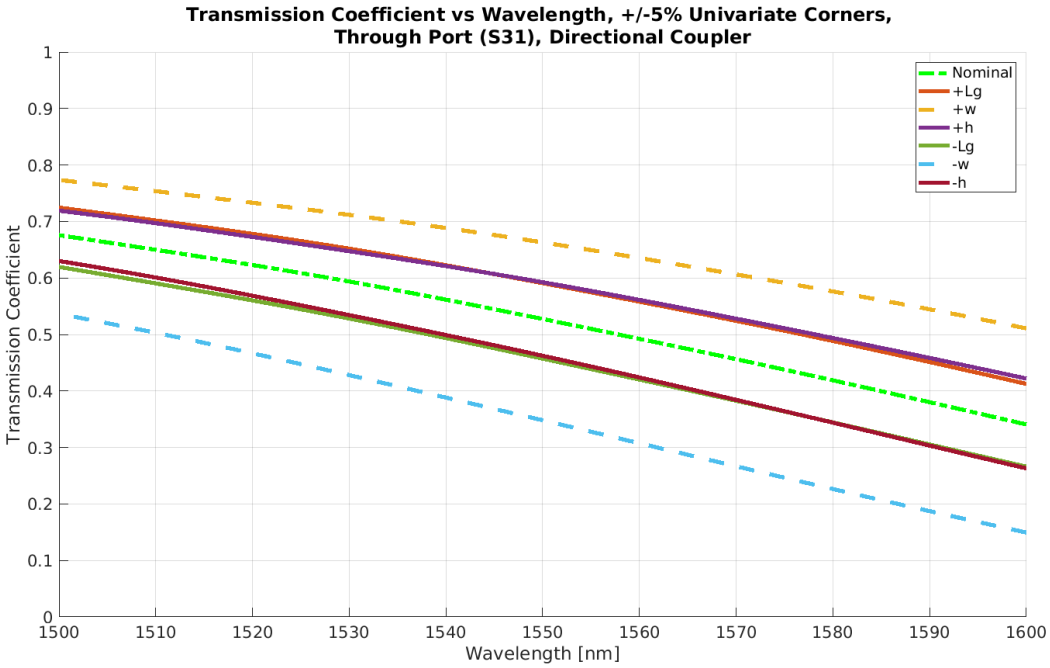


(a) Through port variations.

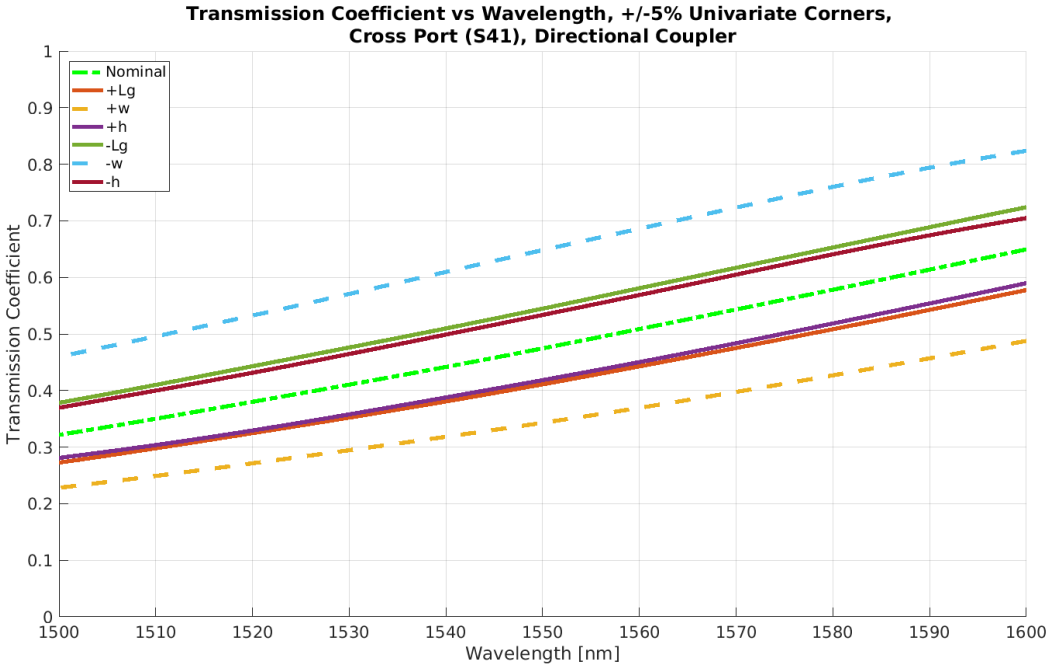


(b) Cross port variations.

Figure 3.12: The power transmitted in the ports of the directional coupler due to applying univariate combinations of the variations ("one-at-at-time" variations), as listed in Table 3.6, representing deviations that are ±5% of the nominal.

Figures 3.11 and 3.12 show the results of running the DoE with the values in Table 3.8.

Through Figure 3.11, we determine that combinations of changing $L_g$, $w$, and $h$ in the same direction (shown as dashed lines) results in the worst-case output performance across all possible combinations of variations in the three variables. Specifically, the combination of $L_g = 210\,nm$, $w = 525\,nm$, and $h = 231\,nm$ results in the least amount of power transfer from the input to the cross port. Also in Figure 3.11, we can see that the combination of $L_g = 190\,nm$, $w = 475\,nm$, and $h = 209\,nm$ results in the most power transfer to the cross port, with about 0.787 transmission at 1550 $nm$ rather than the nominal value of 0.52. These are the worst-case operation cases. Table 3.7 summarizes the results of the corner analysis by showing the input corner combinations that result in device performance extremes at the desired free-space operation wavelength of $\lambda = 1550\,nm$. The symbol "L" denotes the lower deviation value, while the symbol "H" denotes the higher deviation value.

Further, it is determined through Figure 3.12 that the waveguide width is the single variation parameter that affects device performance the most: the change in power transmission is larger when waveguide width is changed by 5% than when other variables undergo a similar change. Waveguide thickness and coupling gap have smaller and similar effects on directional coupler performance.

| Output Performance Case | Value at $\lambda = 1550nm$ | $L_g$ | $w$ | $h$ |
|---|---|---|---|---|
| Through Port Transmission Max | 0.766 | H | H | H |
| Through Port Transmission Min | 0.199 | L | L | L |
| Cross Port Transmission Max | 0.787 | L | L | L |
| Cross Port Transmission Min | 0.254 | H | H | H |
| Maximum Deviation in Split Ratio @ 1550 nm | 75:25 | H | H | H |

Table 3.7: Summary of the worst-case corners of the directional coupler. In this case, the number of parameters changed is five. Parameter variations are ±5% of the respective nominal value.

In a second corner analysis, the parameters are changed using the values in Table 3.8, representing ±1% of nominal deviations. The same modified $2^k$ factorial design is used,

consisting of the $2^k$ corner points, $2k$ axial points, and the nominal case. The same three variables are changed as in the previous example, and the same assumptions hold. In general, using an input variation that is a smaller percentage of the nominal value will cause a smaller fluctuation in the output performance. If it is found that manufacturing process variations are small with respect to the size of the device, then the magnitude of the worst-case output behavior can be reduced. This allows for tighter compact models to be constructed using the smaller output extremes that a 1% corner analysis captures.

| Parameter | Low Value (L, -) | Nominal | High Value (H, +) |
|---|---|---|---|
| Coupling Gap $L_g$ | 198 nm | 200 nm | 202 nm |
| WG Width $w$ | 495 nm | 500 nm | 505 nm |
| WG Thickness $h$ | 217.8 nm | 220 nm | 222.2 nm |

Table 3.8: DoE parameters tested on directional coupler. In this case, the number of parameters changed is three. Parameter variations are $\pm 1\%$ of the respective nominal value.

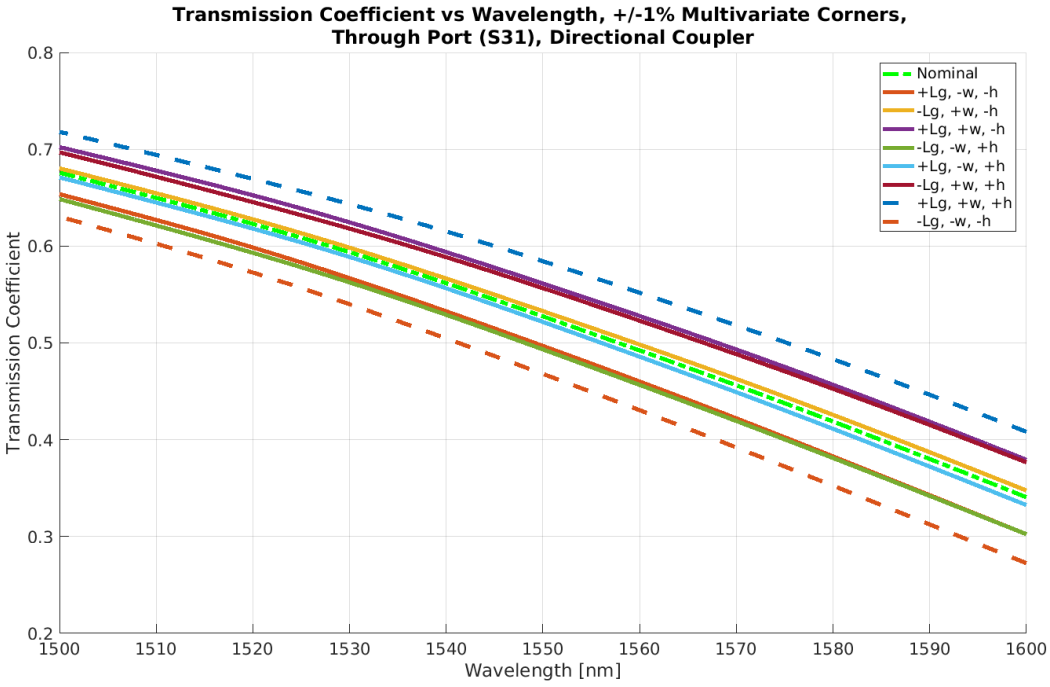


(a) Through port variations.

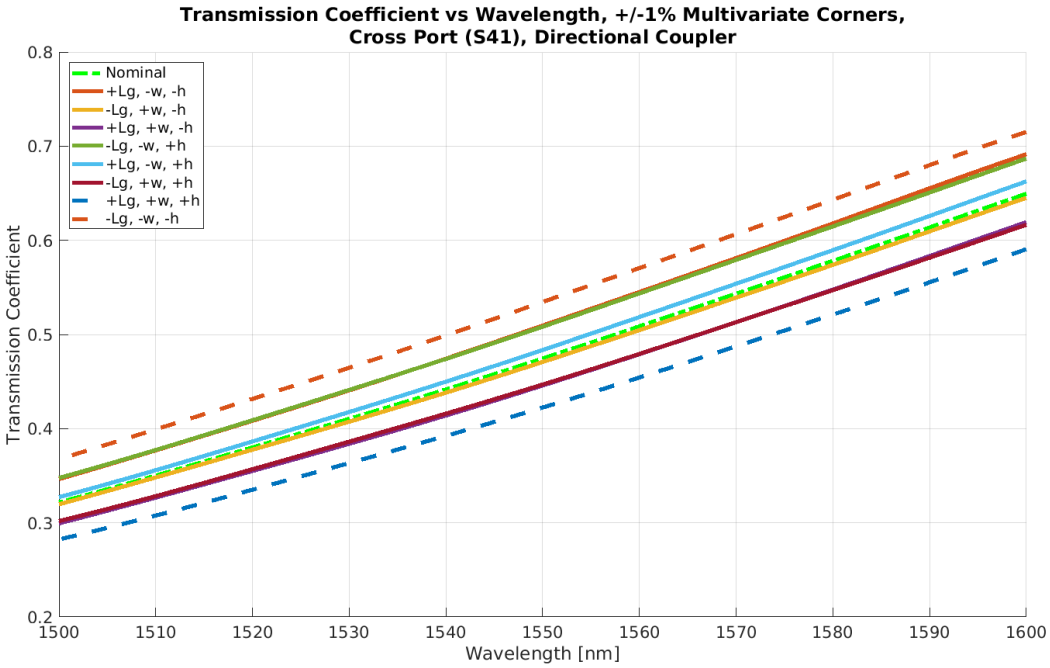


(b) Cross port variations.

Figure 3.13: The power transmitted in the ports of the directional coupler due to applying multivariate combinations of variations, as listed in Table 3.8, now covering deviations that are ±1% of the nominal.

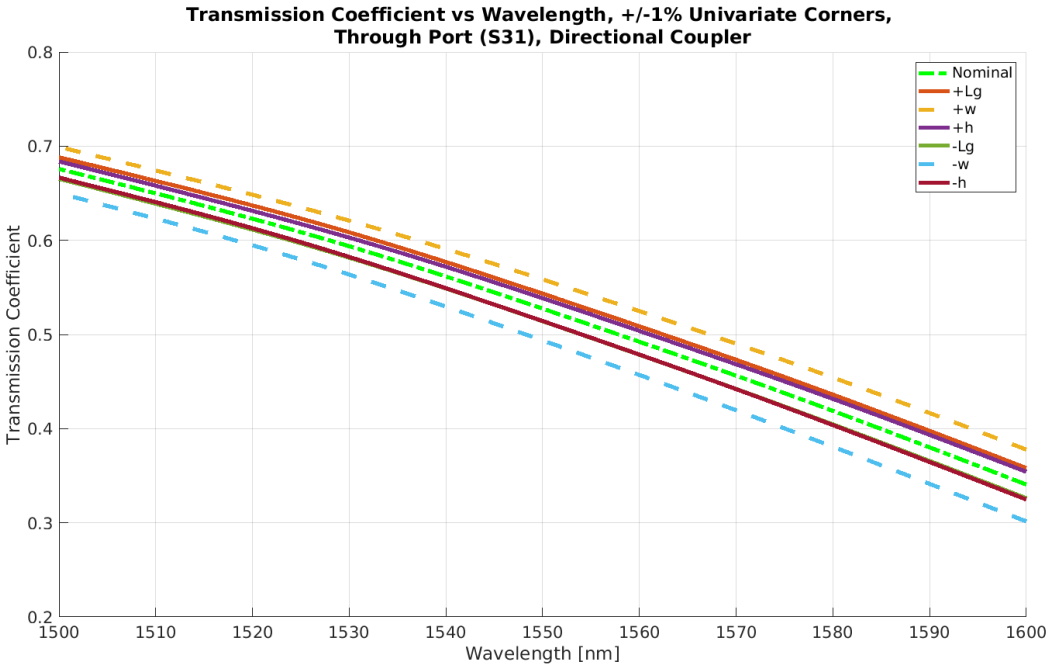


(a) Through port variations.

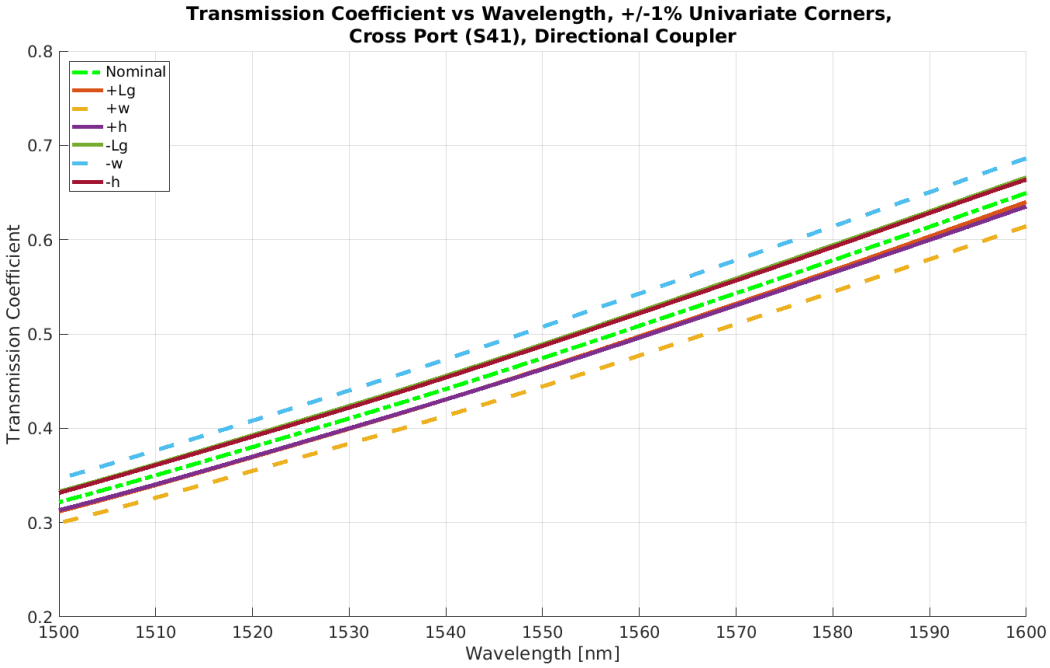


(b) Cross port variations.

Figure 3.14: The power transmitted in the ports of the directional coupler due to applying univariate combinations of the variations as listed in Table 3.8, now covering deviations that are ±1% of the nominal.

Figures 3.13 and 3.14 show the results of running the DoE with the values in Table 3.8.

Through Figure 3.13, we again see that the combination of all positive or all negative deviations in $L_g$, $w$, and $h$, result in the worst-case output performance across all possible combinations of corner variations in the three variables. Table 3.9 summarizes the results of the corner analysis by showing the subset of the input corner combinations that result in device performance extremes at the desired free-space operation wavelength of $\lambda = 1550\ nm$.

Further, Figure 3.14 supports the premise that the waveguide width is the variation parameter that affects device performance the most. As in the previous example, waveguide thickness and coupling gap have smaller effects on directional coupler performance. One other point to note is that the smaller 1% variations do not change the nature of the effects that input variations have on device performance; they only change the magnitude of the effects. This suggests a linear or low-order monotonically increasing trend in the effect of each parameter, which will be further explored in Section 3.3.4. This observation will be of greater relevance in Chapter 4, where we seek to construct response surface compact models.

| Output Performance Case | Value at $\lambda = 1550nm$ | $L_g$ | $w$ | $h$ |
|---|---|---|---|---|
| Through Port Transmission Max | 0.5842 | H | H | H |
| Through Port Transmission Min | 0.4678 | L | L | L |
| Cross Port Transmission Max | 0.5347 | L | L | L |
| Cross Port Transmission Min | 0.4225 | H | H | H |
| Maximum Split Ratio @ 1550 nm | 58:42 | H | H | H |

Table 3.9: Summary of the worst-case corners of the Directional Coupler. In this case, the number of parameters changed is three ($k = 3$). Parameter variations are $\pm 1\%$ of the respective nominal value.

### Five-Parameter DoE

A second set of simulations are run to determine dependencies on variations that cause asymmetry in the device. This requires that the widths and thicknesses of both waveguides in the directional coupler are modified separately. The corner analysis model developed from

this DoE will account for device asymmetry, with the number of parameters changed in the DoE increasing from three to five.

To incorporate device asymmetry, the following parameters are changed:

1. the coupling gap between the two waveguides (denoted as $L_g$,
2. the waveguide widths of the two output branches (denoted as $w_1$ for the top branch and $w_2$ for the bottom branch), and
3. the thickness of each waveguide (denoted as $h_1$ for the top branch and $h_2$ for the bottom branch).

Note that, when applying each process variation before simulation, the thickness and width is perturbed in each waveguide first; this is then followed by perturbing the coupling gap. By following these steps, the variations in coupling gap and waveguide widths are kept independent of one another. A coupling length of $L_c = 16\ \mu m$ and a nominal coupling gap of $L_g = 200\ nm$ are selected for the nominal directional coupler achieving In this way, the nominal performance of the directional coupler as described in Section 3.3.2. Note that the number of combinations of cases increases substantially; if we were to consider all possible combinations with a $3^k$ factorial design, then we have to run $3^5 + 1 = 274$ simulations. Our central composite design still requires $2^k + 2k + 1 = 43$ simulations. Approaches to avoid considering all cases in later photonic circuit evaluations will be discussed further in Chapter 5.

The device geometry is modified using different combinations of the values listed in Table 3.10. A central composite design, as described in Section 2.1.2, is the DoE scheme used to generate the different input test combinations.

| Parameter | Low Value (L, -) | Nominal | High Value (H, +) |
|---|---|---|---|
| Coupling Gap $L_g$ | 190 nm | 200 nm | 210 nm |
| WG Width $w_1$ | 475 nm | 500 nm | 525 nm |
| WG Thickness $h_1$ | 209 nm | 220 nm | 231 nm |
| WG Width $w_2$ | 475 nm | 500 nm | 525 nm |
| WG Thickness $h_2$ | 209 nm | 220 nm | 231 nm |

Table 3.10: DoE parameters tested on directional coupler. In this case, the number of parameters changed is five. Parameter variations are $\pm 5\%$ of the respective nominal value.

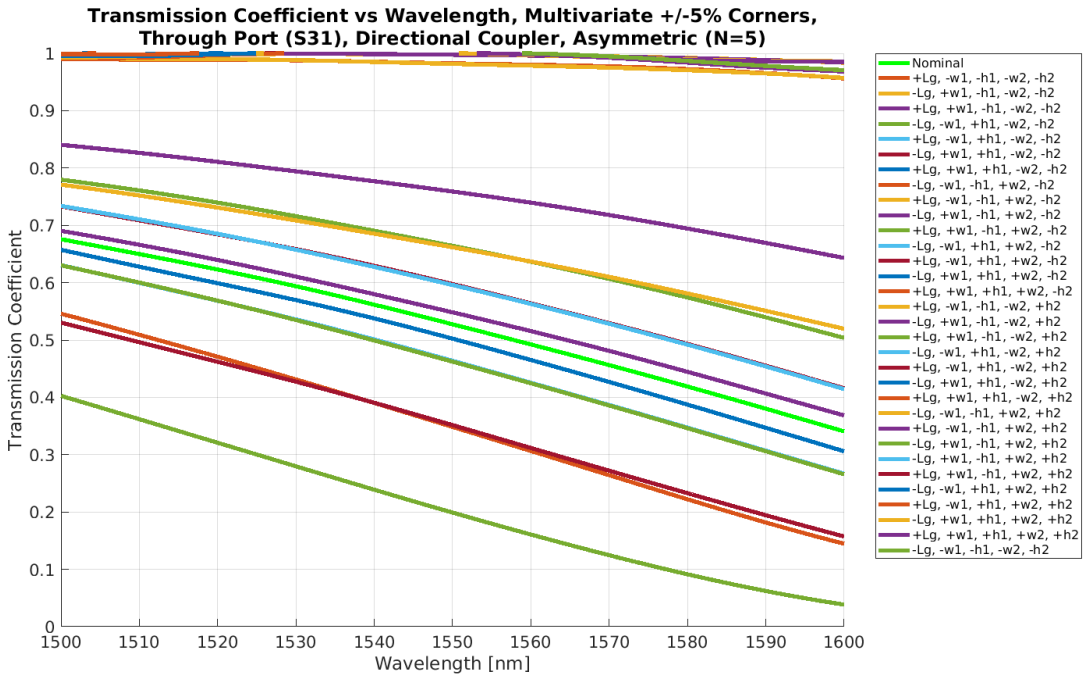


(a) Through port variations.

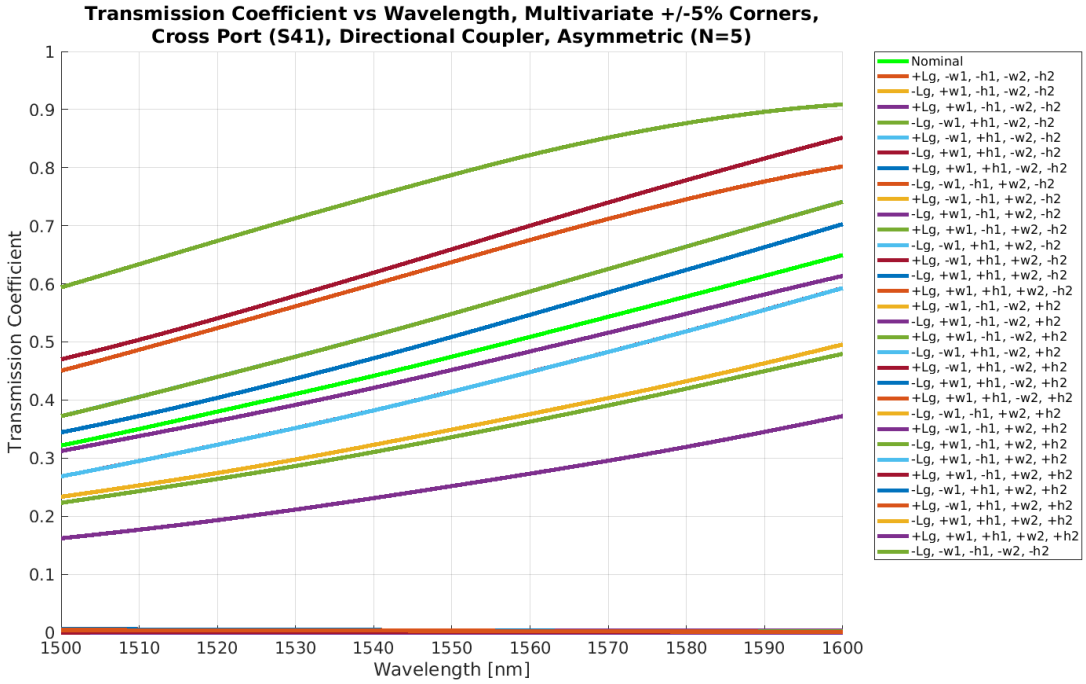


(b) Cross port variations.

Figure 3.15: The power transmitted in the ports of the directional coupler due to applying multivariate combinations of variations, as listed in Table 3.10.

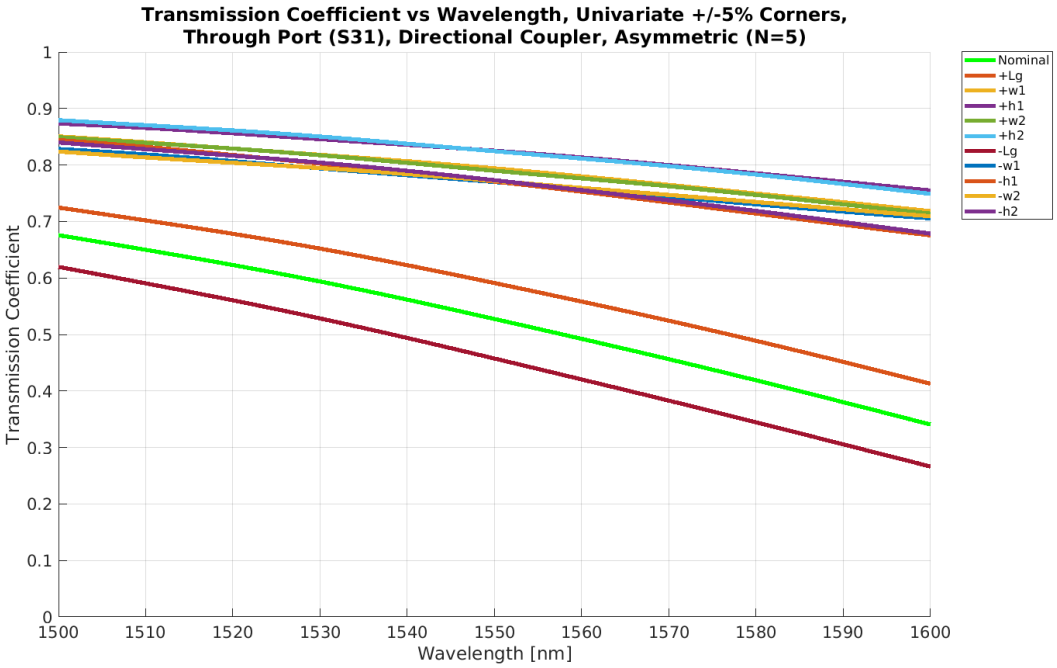


(a) Through port variations.

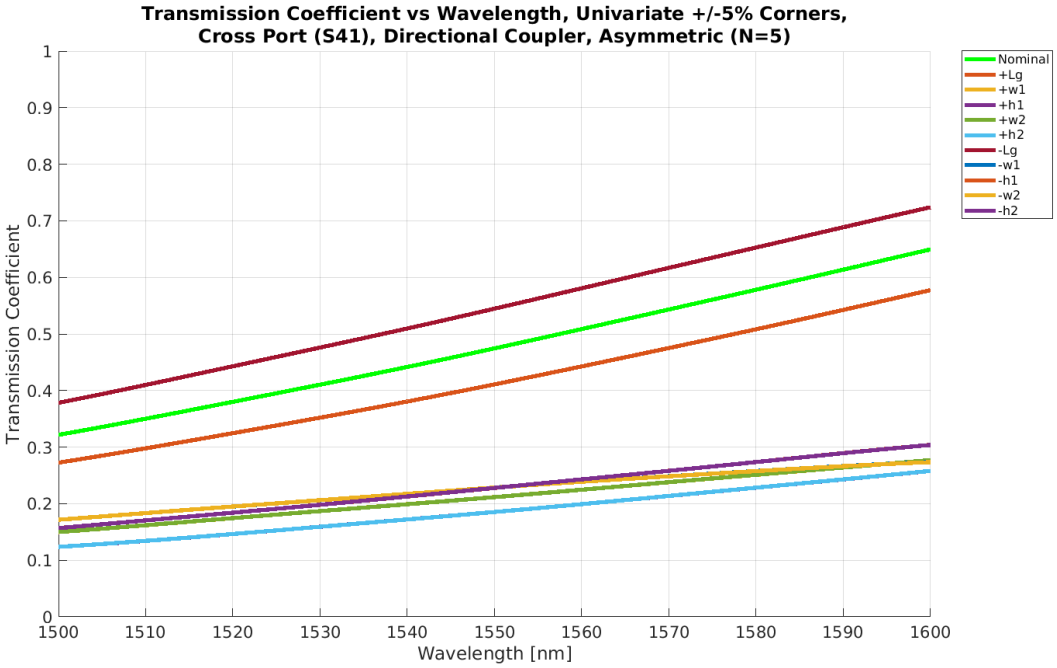


(b) Cross port variations.

Figure 3.16: The power transmitted in the ports of the directional coupler due to applying univariate combinations of variations, as listed in Table 3.10.

The results from the DoE simulations are demonstrated in Figures 3.15 and 3.16. Fig-

ure 3.15 shows the effects of applying combinations of multiple ±5% parameter variations at once. Figure 3.16 shows the effects of applying a single ±5% parameter variation at a time. From this asymmetric directional coupler corner analysis, it is clear that variations that result in an asymmetric geometry have an "unbalancing" effect on the directional coupler. In the cases where the asymmetry is largest, the device hardly couples any light from one waveguide to the other. In the other extreme, where the waveguides are of similar size, the amount of coupling is dependent on how large the waveguides are and their coupling gap. The resulting output variations in these balanced cases are identical to the three-parameter DoE case.

In a typical corner analysis, the worst-case corners are determined from the extremal device operation cases. In the previous examples, this was determined graphically; all that was needed was to compare the outputs from the multivariate cases and select the ones that resulted in the largest deviation from the nominal performance. In this example, where the number of parameters changed is increased to $k = 5$, there are multiple cases that result in zero power coupling between the two waveguides. Unlike the other cases described earlier in the chapter, it is difficult to identify unique worst-case corners from the device operation alone. Multiple large magnitude input variations cause the directional coupler operation to "break" from its intended performance. In such cases, it is proposed that a smaller change in the input variation parameters would facilitate the selection of the worst-case corners. To demonstrate this idea, in a second five parameter corner analysis, the parameters are changed by ±1% of the nominal instead of ±5%. Here, the parameters are changed using the values in Table 3.11, representing the ±1% of nominal deviations. The same central composite design is used. Again, Figures 3.17 and 3.18 show the results of running the DoE with the values in Table 3.8.

| Parameter | Low Value (-) | Nominal | High Value (+) |
|---|---|---|---|
| Coupling Gap $L_g$ | 198 nm | 200 nm | 202 nm |
| WG Width $w_1$ | 495 nm | 500 nm | 505 nm |
| WG Thickness $h_1$ | 217.8 nm | 220 nm | 222.2 nm |
| WG Width $w_2$ | 495 nm | 500 nm | 505 nm |
| WG Thickness $h_2$ | 217.8 nm | 220 nm | 222.2 nm |

Table 3.11: DoE parameters tested on Directional Coupler. In this case, the number of parameters changed is five. Parameter variations are $\pm 1\%$ of the respective nominal value.

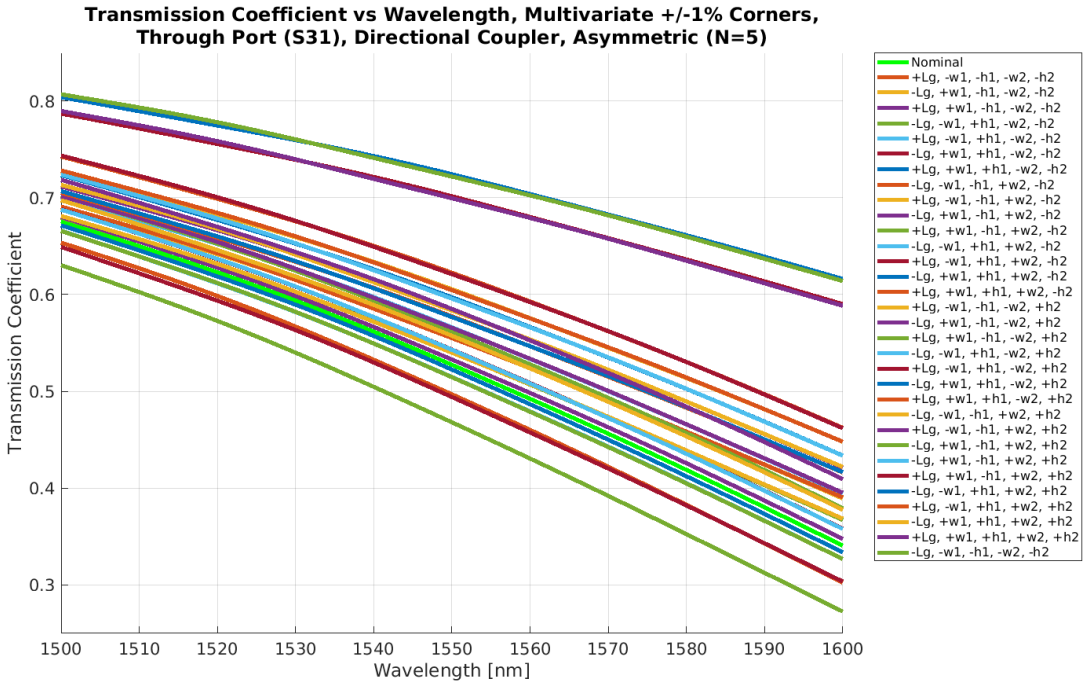


(a) Through port variations.

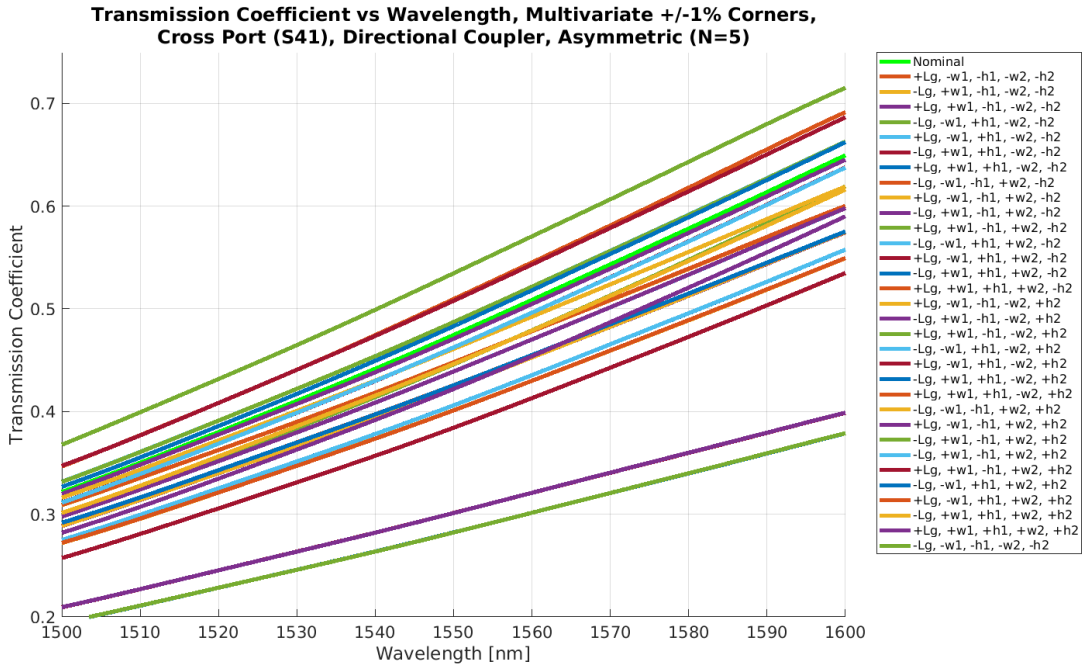


(b) Cross port variations.

Figure 3.17: The power transmitted in the ports of the directional coupler due to applying multivariate combinations of variations, as listed in Table 3.11. The cases that result in the largest variations in device performance are the $-L_g, -w_1, -h_1, -w_2, -h_2$ (lowest coupling) case and the $+L_g, +w_1, +h_1, +w_2, +h_2$ (highest coupling) case.

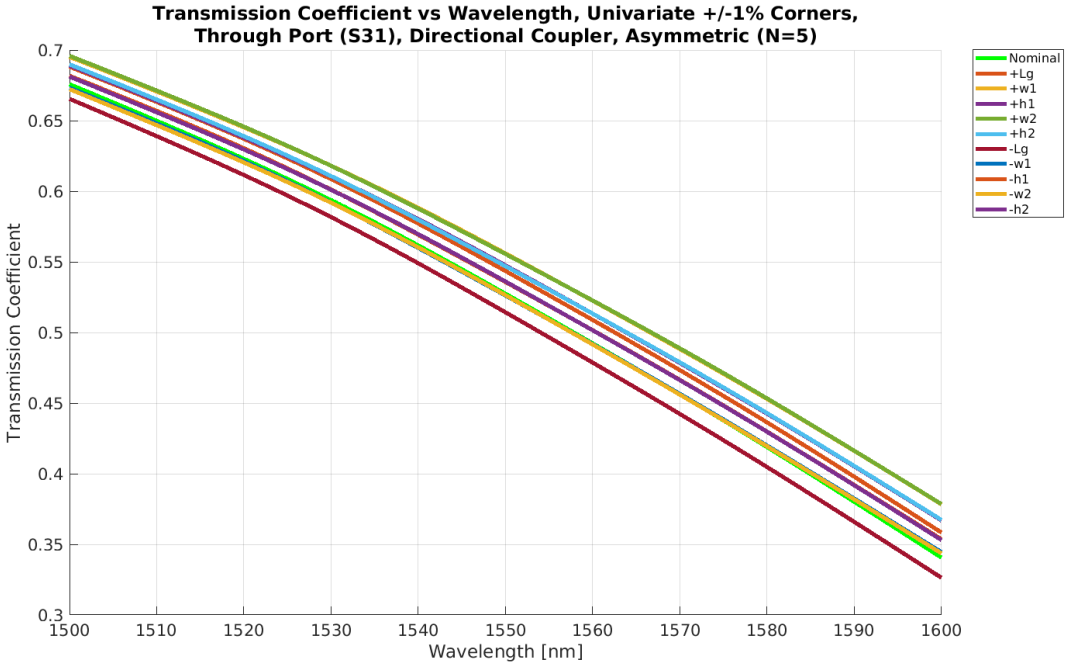


(a) Through port variations.

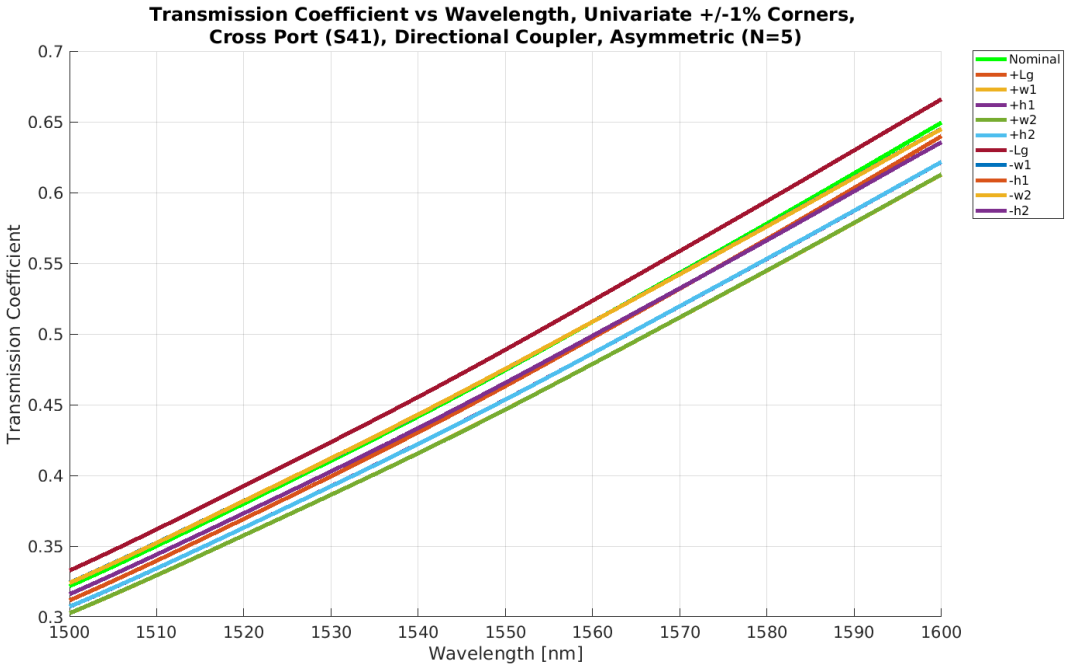


(b) Cross port variations.

Figure 3.18: The power transmitted in the ports of the directional coupler due to applying univariate combinations of variations, as listed in Table 3.11.

Through Figure 3.17, it is now simpler to determine the worst cases of performance in the asymmetric case. Specifically, the combination of $w_1 = 505\ nm$, $h_1 = 222.2\ nm$, $w_2 = 495\ nm$, $h_2 = 217.8\ nm$ and $L_g = 202\ nm$ results in the least amount of power transfer between the through and cross ports. The combination of $w_1 = 495\ nm$, $h_1 = 217.8\ nm$, $w_2 = 495nm$, $h_2 = 217.8\ nm$ and $L_g = 202\ nm$ results in the most amount of power transfer. Table 3.12 summarizes the resulting output worst-case corner subsets. Further, Figure 3.18 supports the premise that the waveguide width is the variation parameter that affects device performance the most. As in the previous example, waveguide thickness and coupling gap have smaller and similar magnitude effects on directional coupler performance.

| Output Performance Case | Value at $\lambda = 1550nm$ | $L_g$ | $w_1$ | $h_1$ | $w_2$ | $h_2$ |
|---|---|---|---|---|---|---|
| Through Port Transmission Max | 0.7241 | H | H | H | L | L |
| Through Port Transmission Min | 0.4678 | L | L | L | L | L |
| Cross Port Transmission Max | 0.5347 | L | L | L | L | L |
| Cross Port Transmission Min | 0.2823 | H | L | L | H | H |
| Split Ratio Max | 72:28 | H | H | H | L | L |

Table 3.12: Summary of the worst-case corners of the Directional Coupler. In this case, the number of parameters changed is five ($k = 5$). Parameter variations are $\pm 1\%$ of the respective nominal value.

### 3.3.4 Sensitivity Analysis

As noted in Section 3.2.4, in addition to constructing a worst-case compact model, the results of a corner analysis are typically used to determine and quantify how the directional coupler operation changes as the input parameters change. Using the approach previously introduced for the Y-branch, we perform sensitivity analysis here for the directional coupler. Figures 3.19, 3.20, and 3.21 visualize the sensitivity of the output performance of the directional coupler with respect to $L_g$, $w$, and $h$, respectively. The particular power transmission

output is measured at $\lambda = 1550\ nm$.

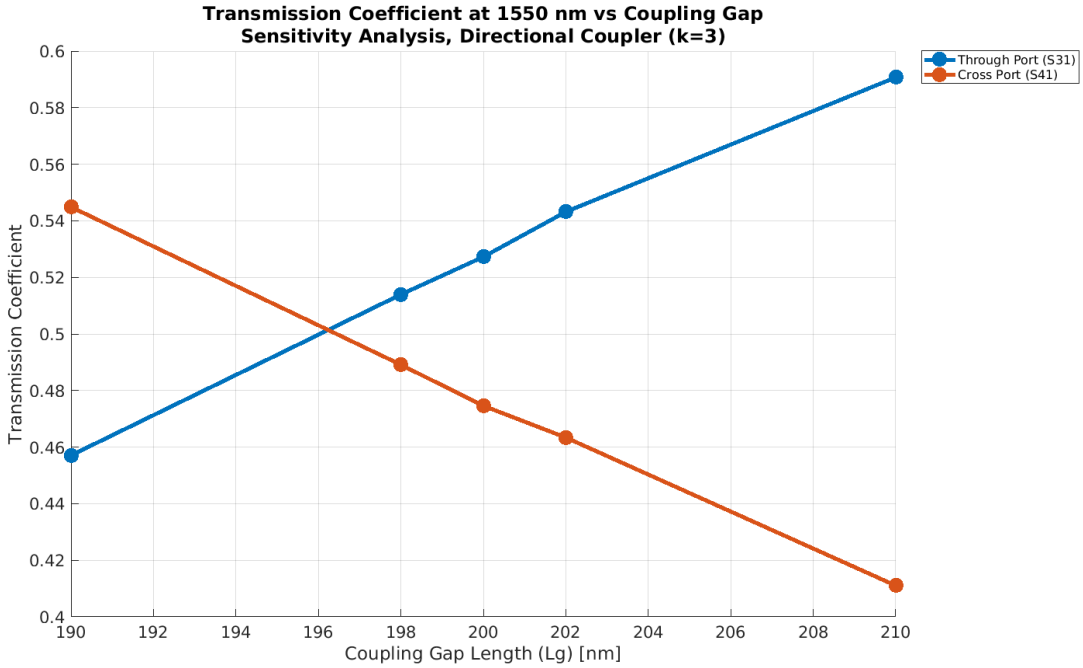


Figure 3.19: Sensitivity of directional coupler power transmission versus coupling gap length measured at $\lambda = 1550nm$. The specific values applied in each test are listed in Tables 3.6 and 3.8.

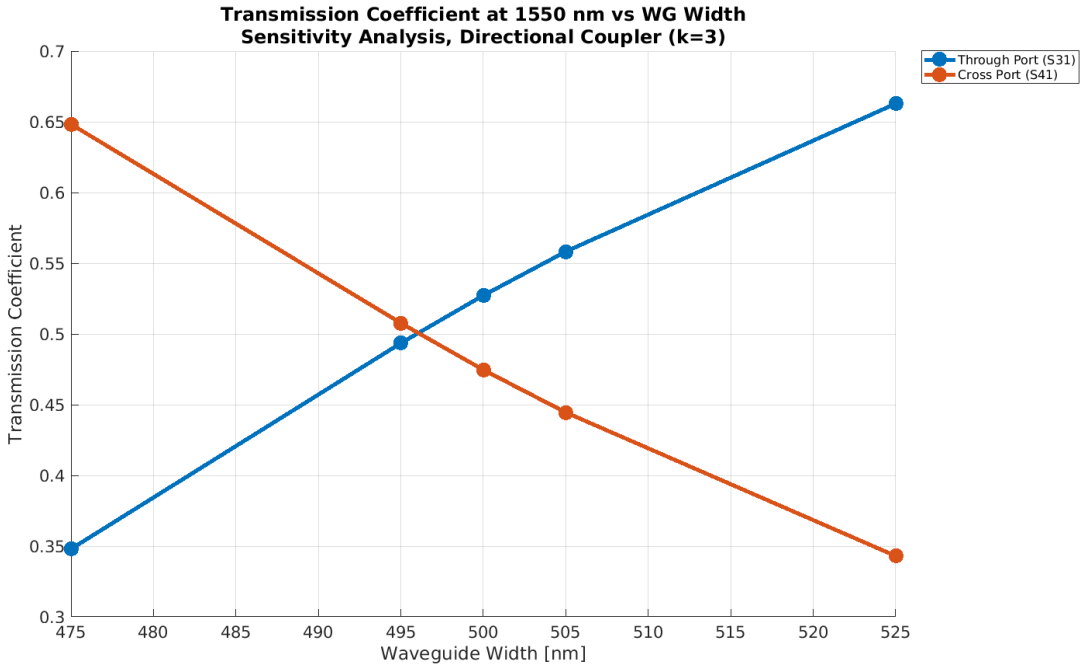


Figure 3.20: Sensitivity of directional coupler power transmission versus lower branch width measured at $\lambda = 1550nm$. The specific values applied in each test are listed in Tables 3.6 and 3.8.

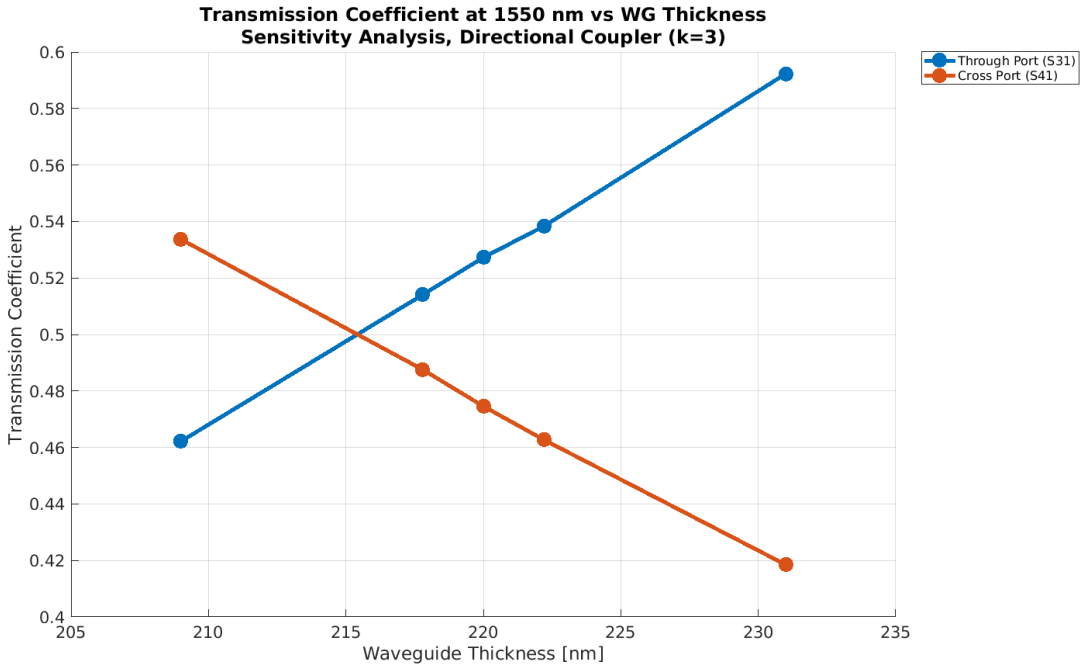


Figure 3.21: Sensitivity of directional coupler power transmission versus waveguide thickness measured at $\lambda = 1550nm$. The specific values applied in each test are listed in Tables 3.6 and 3.8.

| Sensitivity Parameter | -5% | -1% | +1% | +5% |
|---|---|---|---|---|
| $\frac{\delta\|S31\|^2}{\delta w}$ | $0.00717\frac{1}{nm}$ | $0.00675\frac{1}{nm}$ | $0.00620\frac{1}{nm}$ | $0.00542\frac{1}{nm}$ |
| $\frac{\delta\|S31\|^2}{\delta h}$ | $0.00592\frac{1}{nm}$ | $0.00598\frac{1}{nm}$ | $0.00502\frac{1}{nm}$ | $0.00591\frac{1}{nm}$ |
| $\frac{\delta\|S31\|^2}{\delta L_g}$ | $0.00702\frac{1}{nm}$ | $0.00666\frac{1}{nm}$ | $0.00796\frac{1}{nm}$ | $0.00634\frac{1}{nm}$ |
| $\frac{\delta\|S41\|^2}{\delta w}$ | $-0.00695\frac{1}{nm}$ | $-0.00661\frac{1}{nm}$ | $-0.00602\frac{1}{nm}$ | $-0.00526\frac{1}{nm}$ |
| $\frac{\delta\|S41\|^2}{\delta h}$ | $-0.00537\frac{1}{nm}$ | $-0.00589\frac{1}{nm}$ | $-0.00539\frac{1}{nm}$ | $-0.00510\frac{1}{nm}$ |
| $\frac{\delta\|S41\|^2}{\delta L_g}$ | $-0.00703\frac{1}{nm}$ | $-0.00726\frac{1}{nm}$ | $-0.00560\frac{1}{nm}$ | $-0.00635\frac{1}{nm}$ |

Table 3.13: Estimated sensitivity of the directional coupler due to the different parameters tested. $|S31|^2$ corresponds to the power transmitted through the through port normalized by the input power. $|S41|^2$ corresponds to the power transmitted through the cross port normalized by the input power. Input parameter variations are listed in Table 3.1 and 3.3.

Table 3.13 provides estimates of the directional coupler sensitivity to the input parameters (coupling gap, waveguide width and thickness). The columns indicate which univariate case is used to calculate the corresponding sensitivity estimate based on the slope between the two corresponding points in Figures 3.19, 3.20, and 3.21. From this information, we see that the directional coupler operation is sensitive to changes in any of the three parameters; for example, a 1 $nm$ change in coupling gap can cause power transmission in the ports to increase by 0.007958 or decrease by -0.007262. Even a 2 $nm$ change in $L_g$ is enough to modify the coupling ratio at a particular wavelength from 50:50 to 51:49 or 52:48. We also see that there is slight nonlinearity in the sensitivities, but that across our 1% and 5% range of deviations

in input, these are only modest. This supports the use of a single average sensitivity in these cases, as in a low-order response surface model as to be discussed in Chapter 4.

## 3.4 Summary

In this chapter, the corner analysis method for generating a variation-aware compact model of photonic devices has been demonstrated. Three examples of corner analysis models are discussed. The first example describes the procedure in the context of the Y-branch. The last two examples focus on the corner model of the directional coupler device and contrasts the effect of adding more variables to the corner model. Use of the completed corner models are demonstrated, understanding the subset of worst-case inputs corresponding to worst-case output performance of the device, as well as in understanding the sensitivity of performance with respect to individual input deviations. The method described here can be used to create compact models consisting of multiple discrete corners that can predict chip-to-chip variations and worst-case performance of a design. However, photonic devices can also vary on a device-by-device basis, and these variations are often random and on a smaller order than the worst-case performance. Chapter 4 describes the process of developing a parametric compact model that can capture these variations.

# Chapter 4

# Compact Models Based on Response Surface Modeling Method

Once a set of experiments is carried out and the worst-case behavior with respect to parameter variations is discovered, a compact model of the device can be made from this experimental data in the form of a set of discrete input and output corner cases. These corner models are often sufficient to evaluate the worst-case performance of a photonic circuit design. However, it is also often desired to understand the circuit's performance when hundreds or thousands of different designs – each with slight, randomized variations in device parameters – are realized. A stochastic simulation is carried out that generates a large number of different realizations of the design. These simulations can be used to estimate the manufacturing yield of an integrated circuit, photonic or electronic. In these types of design analysis, corner modeling of devices is not sufficient to estimate the manufacturing yield; device models that can estimate the effects of random variations are required.

## 4.1 Response Surface Modeling Method

The response surface modeling (RSM) method is one way to model the effects of parametric variations in a compact form, in a representation that can be used for statistical analysis

of random variations. This method takes the test cases measured from the DoE methods explained earlier and approximates the underlying function that describes the effects of variation on the device performance [18]. This function is an input-output relationship between the process or device variations and the resulting performance. A common way to approximate the underlying function is to use the least-squares fitting method to find the coefficients to a multivariate polynomial function. To test whether or not the fitting function can estimate the underlying behavior based on the test cases provided, an analysis of variance (ANOVA) is carried out [19, 20]. If the model does not capture the overall trend of variations effectively or has a high mean squared error, more variables can be added to the model if there is lack of fit. Hypothesis testing is carried out to eliminate dependencies and model parameters that do not contribute to the model to avoid overfitting.

The proposed design methodology is the following:

1. Carry out a corner analysis based on a predefined design of experiments, as in Chapter 3, to find the empirical points. These points will form the basis of the fitting function.

2. Use the least squares method to fit the simulated outputs for the empirical test points to a polynomial function in the number of variables modified in the DoE.

3. Run an analysis of variance to determine the goodness of fit of the function on the data, and to only retain significant model terms.

4. If the response surface is determined to be a good fit based on the data provided, then this function can serve as a compact model. Otherwise, repeat steps 2 and 3 until a good fit is achieved, either by adding more terms and coefficients, or by adding additional simulation data.

The basic procedure and key equations for steps 2 and 3 will be summarized here; more details are explained in Myers, et al., and Khuri, et al. [19, 20]. All of the response surface

models in this section are constructed using MATLAB software. MATLAB is chosen for its compatibility with the Lumerical software, which is used for both photonic device and circuit simulation. The results of DoE simulations in Lumerical FDTD are imported into MATLAB, enabling fitting to the polynomial response surface mode form.

### 4.1.1 Fitting to a Functional Form

The response surface modeling method uses the least-squares method from linear algebra to fit the data to a functional form [19]. It is desired to approximate the underlying data as a function of multiple variables:

$$y = f(x_1, x_2, x_3, \cdots, x_k) + \epsilon, \tag{4.1}$$

where $y$ are the output observations, $f(x_1, x_2, x_3, \cdots, x_k)$ is the form of the approximate modeling function, and $\epsilon$ is the modeling error and/or random variation in the data. The approximate modeling function can be any combination of the input variables $x_1, x_2, x_3, \cdots, x_k$, though here we will restrict consideration to polynomial functions in $x_1$ to $x_k$. Our polynomial function can include both diagonal terms ($x_k^2, x_k^3, etc.$) and cross terms ($x_2 x_3, etc.$) as long as the model is not an over-fit of the data. The process for determining the effectiveness of a response surface model is explained further in Section 4.1.2.

As an example, let the approximating function form be affine (linear plus added constant

term) in all the $x_k$ variables. Then, the input-output relationship can be written as

$$\begin{aligned} y &= \beta_0 + \beta_1 x_1 + \beta_2 x_2 + ... + \beta_k x_k + \epsilon \\ &= \begin{bmatrix} 1 & x_1 & x_2 & \cdots & x_k \end{bmatrix} \cdot \begin{bmatrix} \beta_0 \\ \beta_1 \\ \beta_2 \\ \vdots \\ \beta_k \end{bmatrix} + \epsilon \\ &= \boldsymbol{f(x)^T} \cdot \boldsymbol{\beta} + \epsilon, \end{aligned} \tag{4.2}$$

where $\boldsymbol{f(x)^T}$ is a vector describing the model relationship between $y$ and the $x_k$ terms, $\boldsymbol{\beta}$ is a vector that contains the model coefficients, and $\epsilon$ is the fitting error. Assume that there are $N$ observations of $y$ corresponding to different test combinations of the $x_k$'s. In the examples that will be discussed in later sections of this chapter, the observations are exactly the corner analysis results discussed in Sections 3.2.3 and 3.3.3. The first-order model can be expressed in a matrix equation representation as:

$$\begin{aligned} \boldsymbol{y} = \begin{bmatrix} y_1 \\ y_2 \\ y_3 \\ \vdots \\ y_N \end{bmatrix} &= \begin{bmatrix} 1 & x_{1,1} & x_{2,1} & \cdots & x_{k,1} \\ 1 & x_{1,2} & x_{2,2} & \cdots & x_{k,2} \\ 1 & x_{1,3} & x_{2,3} & \cdots & x_{k,3} \\ \vdots & \vdots & \vdots & \ddots & \vdots \\ 1 & x_{1,N} & x_{2,N} & \cdots & x_{k,N} \end{bmatrix} \cdot \begin{bmatrix} \beta_0 \\ \beta_1 \\ \beta_2 \\ \vdots \\ \beta_k \end{bmatrix} + \begin{bmatrix} \epsilon_1 \\ \epsilon_2 \\ \epsilon_3 \\ \vdots \\ \epsilon_N \end{bmatrix} \\ &= \boldsymbol{X} \cdot \boldsymbol{\beta} + \boldsymbol{\epsilon}, \end{aligned} \tag{4.3}$$

and the normal equations in 4.3 are solved to find $\boldsymbol{\beta}$, the vector representing the model coefficients using the least-squares method. The steps for finding $\boldsymbol{\beta}$ are shown here for reference:

$$\boldsymbol{X_T X \beta} = \boldsymbol{X^T y} \tag{4.4}$$

$$\boldsymbol{\beta} = (\boldsymbol{X^T X \beta})^{-1} \cdot \boldsymbol{X^T y}. \tag{4.5}$$

When fitting using the response surface model method, it is beneficial to "code" the particular values of each input variable with a linear transformation:

$$x_{i,coded} = \frac{x_i - 2(x_{i,max} + x_{i,min})}{x_{i,max} - x_{i,min}}, \tag{4.6}$$

where $x_i$,...,$x_k$ are values of the individual variables that one wants to fit. Let $x_{i,max}$,...,$x_{k,max}$ be the maximum value of $x_i$,...,$x_k$ in the data set, and $x_{i,min}$,...,$x_{k,min}$ be the minimum value of $x_i$,...,$x_i$ in the data set, respectively. The rationale for using coded variables is rooted in computation; this method results in a fitting matrix $\boldsymbol{X}$ where all of the values fall in between -1 and +1. This scheme makes sure that the $(\boldsymbol{X^T X \beta})^{-1}$ matrix is not close to a singular matrix and facilitates the analysis of variance process (details found in Section 4.1.2). This coding scheme is widely used in fitting models using the least-squares method [20].

### 4.1.2 Testing for Goodness of Fit

Once the test points are fit to a response surface in a certain number of variables, the numerical model is constructed. However, the model form might not be sufficient to be an accurate prediction of device performance. To test whether or not the constructed model is accurate and sufficient, an analysis of variance is performed. The important results are summarized here; further explanation can be found in Myers, et al. and Khuri, et al. [19, 20]. All ANOVA parameters are presented here using a matrix representation.

We let $N$ be the number of observations used in constructing the model and $p$ be the number of non-constant terms in the proposed response surface model. The total sum of squares (SST) measures the difference between the observations and the overall mean of the observations:

$$SST = \boldsymbol{y^T y} - \frac{(\boldsymbol{1^T \cdot y})^2}{N} \tag{4.7}$$

The sum of squares due to regression (SSR) is another parameter that is calculated in an ANOVA:

$$SSR = \boldsymbol{b^T}(\boldsymbol{X^T y}) - \frac{(\boldsymbol{1^T \cdot y})^2}{N}. \tag{4.8}$$

It measures how well the RSM represents the observations. The sum of squared errors of prediction (SSE) is a measure of the discrepancy between the model and the observations:

$$\begin{aligned} SSE &= \boldsymbol{y^T y} - \boldsymbol{b^T}(\boldsymbol{X^T y}) \\ &= SST - SSR. \end{aligned} \tag{4.9}$$

A small SSE compared to the SSR is one indicator of an accurate response surface model. The mean squared residuals (MSR) and mean squared error (MSE) are obtained from the SSR and the SSE, respectively.

$$MSR = \frac{SSR}{(p-1)} \tag{4.10}$$

$$MSE = \frac{SSE}{(N-p)} \tag{4.11}$$

The results from an analysis of variances are typically summarized in a table format for simple comparison.

| Analysis of Variances | | | |
|---|---|---|---|
| Source of Variation | Degrees of Freedom | Sum of Squares | Mean Square |
| Fitted Model | $p-1$ | $SSR$ | $MSR = \frac{SSR}{(p-1)}$ |
| Residuals | $N-p$ | $SSE$ | $MSE = \frac{SSE}{(n-p)}$ |
| Total | $N-1$ | $SST$ | |
| F-Ratio | $F = \frac{MSR}{MSE}$ | $F_{critical} = F_{p-1,N-p,0.95}$ | |
| P-Value | p-value | | |

Table 4.1: A typical analysis of variances results table for a response surface fit.

Once the ANOVA is calculated, it is possible to determine the parameters used to evaluate the goodness of fit of a response surface. The coefficient of determination, known as R-squared or $R^2$, is one such parameter. It is defined as the proportion of variance in the output variable that can be explained with the model:

$$R^2 = \frac{SSR}{SST} = 1 - \frac{SSE}{SST} \tag{4.12}$$

The coefficient of determination measures how well the response surface approximates the underlying relationship. It is a positive value that ranges zero to one; a model fit with R-squared value close to one represents a model fit that accurately predicts the underlying input-output behavior. It is often possible to increase the SSR by increasing the number of model coefficients. As a result, R-squared generally increases with the number of terms in the model. Thus, the R-squared parameter alone is not a good indicator of overfitting. For this reason, an adjusted R-squared parameter is used in conjunction with the R-squared parameter:

$$R^2_{adj} = 1 - (1 - R^2)\frac{n-1}{n-p-1} \leq R^2. \tag{4.13}$$

This parameter is always less than or equal to $R^2$, but penalizes for the use of additional parameters $p$. If a term is added to the RSM and an increase in $R^2$ is not followed by an increase in $R^2_{adj}$, then it is likely that the added term results in an over-fitted response surface.

If it is determined from the $R^2_{adj}$ value that the proposed functional form is overfitting to the data, then one or more terms can be eliminated from the model. Figuring out which terms to eliminate involves measuring the confidence intervals of each model coefficient. A confidence interval is a range of values that could serve as an estimate of the true model coefficient value. They are calculated using different methods; this thesis uses the Student's t-distribution to estimate parameter confidence intervals. For every RSM in this thesis, the 95% confidence intervals are calculated for every model coefficient. If the confidence interval

of a model coefficient contains zero, then the hypothesis that the true value of that coefficient is zero cannot be rejected. The added term is overfitting to the observations and does not accurately represent the underlying input-output relationship; it can safely be removed.

## 4.2 Y-Branch Response Surface Model

In this section, the procedure for creating a compact response surface model for a Y-branch device is discussed. First, the results of fitting the DoE simulation results to a response surface are presented. Next, the method of creating compact models for the Y-branch is demonstrated. The operation of a typical Y-branch is discussed earlier in Section 3.2.2. This section builds upon that discussion and the corner analysis results that are described in Section 3.2.3.

### 4.2.1 RSM Equation Model

For the Y-branch, three variation parameters are selected: waveguide thickness (denoted as $h$) and waveguide widths of the two output branches (denoted as $w_1$ and $w_2$). The waveguide thickness is varied across the entire device, while the modified waveguide widths are limited to only the specific waveguide that is perturbed. The DoE that was used to obtain the empirical results is described in detail in Section 2.1.2 and in Section 3.2.3. Here, we use the central composite design combining axial, corner, and center points already considered earlier for consistent surface fits across the different fitting parameters.In the set of experiments done to find the corner model, we changed these three parameters: $h$, $w_1$, and $w_2$. Further, the device operation was found for free-space wavelengths along the range of $\lambda = 1500$ to 1600 $nm$. Within this range of values for $\lambda$, 1000 evenly-spaced wavelength samples are taken from simulation results.

For each fitting parameter, we use the following coded variable representation for each

parameter tested:

$$\lambda_{coded} = \frac{\lambda - 2(1600nm + 1500nm)}{1600nm - 1500nm}, \tag{4.14}$$

$$w_{1,coded} = \frac{w_1 - 2(525nm + 475nm)}{525nm - 475nm}, \tag{4.15}$$

$$h_{coded} = \frac{h - 2(231nm + 209nm)}{231nm - 209nm}, \tag{4.16}$$

$$w_{2,coded} = \frac{w_2 - 2(525nm + 475nm)}{525nm - 475nm}, \tag{4.17}$$

This allows us to find a polynomial form for the device performance in terms of the four variables listed, including both device parameters ($h$, $w_1$, and $w_2$) and operating parameter $\lambda$. We thus create a hybrid process/input wavelength model of the form shown in Equations 4.19 - 4.21. For each RSM fit, the positive and negative confidence intervals for each term are presented in Tables 4.2 - 4.4.

S-parameters are complex-valued; they can be represented as a magnitude and phase for each parameter, or they can be represented using real and imaginary parts. In either configuration, each S-parameter has two sets of values to fit. In this thesis, response surfaces that fit the S-parameter magnitude are demonstrated; the same procedure can be applied to the phase. The Y-branch is a three port device, so it will have nine S-parameters in total (three for each port). However, six S-parameters are equivalent to one another:

$$\begin{aligned} S_{21} &= S_{12} \\ S_{31} &= S_{13} \\ S_{23} &= S_{32}. \end{aligned} \tag{4.18}$$

The number of S-parameters to fit is now reduced from nine to six.

The model equations are written in terms of the coded variables $\lambda_{coded}$, $w_{1,coded}$, $w_{2,coded}$ and $h_{coded}$ for brevity. The confidence intervals on every model coefficient are calculated for every model equation; these are listed in Tables 4.2 - 4.4.

$$
\begin{aligned}
|S_{11}|^2 \approx\ & 0.001309 + 7.1198 \cdot 10^{-4}\lambda_{coded} - 3.2315 \cdot 10^{-4}w_{1,coded} \\
& - 1.6140 \cdot 10^{-4}h_{coded} - 3.2337 \cdot 10^{-4}w_{2,coded} - 1.0604 \cdot 10^{-4}\lambda_{coded}w_{1,coded} \\
& + 1.3669 \cdot 10^{-5}\lambda_{coded}h_{coded} - 1.0593 \cdot 10^{-4}\lambda_{coded}w_{2,coded} + 3.3495 \cdot 10^{-5}\lambda_{coded}^2 \\
& - 3.5439 \cdot 10^{-4}\lambda_{coded}^3
\end{aligned}
\tag{4.19}
$$

| Results for $\lvert S_{11}\rvert^2$ Fit | | |
|---|---|---|
| Model Coefficient | Negative Conf. Interval | Positive Conf. Interval |
| Constant Term | 0.001306 | 0.001311 |
| $\lambda_{coded}$ | $7.0464 \cdot 10^{-4}$ | $7.1932 \cdot 10^{-4}$ |
| $w_{1,coded}$ | $-3.2523 \cdot 10^{-4}$ | $-3.2108 \cdot 10^{-4}$ |
| $h_{coded}$ | $-1.6348 \cdot 10^{-4}$ | $-1.5932 \cdot 10^{-4}$ |
| $w_{2,coded}$ | $-3.2545 \cdot 10^{-4}$ | $-3.2129 \cdot 10^{-4}$ |
| $\lambda_{coded}w_{1,coded}$ | $-1.0963 \cdot 10^{-4}$ | $-1.0244 \cdot 10^{-4}$ |
| $\lambda_{coded}h_{coded}$ | $1.0074 \cdot 10^{-5}$ | $1.7265 \cdot 10^{-5}$ |
| $\lambda_{coded}w_{2,coded}$ | $-1.0953 \cdot 10^{-4}$ | $-1.0234 \cdot 10^{-4}$ |
| $\lambda_{coded}^2$ | $-3.9178 \cdot 10^{-5}$ | $-2.7813 \cdot 10^{-5}$ |
| $\lambda_{coded}^3$ | $-3.6558 \cdot 10^{-4}$ | $-3.4321 \cdot 10^{-4}$ |

Table 4.2: Confidence intervals for Y-branch $|S_{11}|^2$ RSM fit.

$$
\begin{aligned}
|S_{21}|^2 \approx\ & 0.483396 + 0.002568\lambda_{coded} + 0.012862w_{1,coded} \\
& - 0.001016h_{coded} - 0.006095w_{2,coded} + 0.002120\lambda_{coded}w_{1,coded} \\
& - 0.001640\lambda_{coded}h_{coded} - 0.005704\lambda_{coded}^2 + 0.003025\lambda_{coded}^3
\end{aligned}
\tag{4.20}
$$

| Results for $\lvert S_{21}\rvert^2$ Fit | | |
|---|---|---|
| Model Coefficient | Negative Conf. Interval | Positive Conf. Interval |
| Constant Term | 0.483363 | 0.483428 |
| $\lambda_{coded}$ | 0.002475 | 0.002660 |
| $w_{1,coded}$ | 0.012836 | 0.012888 |
| $h_{coded}$ | $-0.001042$ | $-9.8942 \cdot 10^{-4}$ |
| $w_{2,coded}$ | $-0.006121$ | $-0.006069$ |
| $\lambda_{coded} w_{1,coded}$ | 0.002074 | 0.002165 |
| $\lambda_{coded} h_{coded}$ | $-0.001686$ | $-0.001595$ |
| $\lambda^2_{coded}$ | $-0.005775$ | $-0.005632$ |
| $\lambda^3_{coded}$ | 0.002884 | 0.003167 |

Table 4.3: Confidence intervals for Y-branch $\lvert S_{21}\rvert^2$ RSM fit.

$$\begin{aligned} |S_{31}|^2 \approx\ & 0.483393 + 0.0025696\lambda_{coded} - 0.006095 w_{1,coded} \\ & - 0.001016 h_{coded} + 0.012863 w_{2,coded} - 0.001641 \lambda_{coded} h_{coded} \\ & + 0.002119 \lambda_{coded} w_{2,coded} - 0.005702 \lambda^2_{coded} + 0.003024 \lambda^3_{coded} \end{aligned} \tag{4.21}$$

| Results for $\lvert S_{31}\rvert^2$ Fit | | |
|---|---|---|
| Model Coefficient | Negative Conf. Interval | Positive Conf. Interval |
| Constant Term | 0.483361 | 0.483425 |
| $\lambda_{coded}$ | 0.002477 | 0.002662 |
| $w_{1,coded}$ | $-0.006121$ | $-0.006069$ |
| $h_{coded}$ | $-0.001042$ | $-9.8979 \cdot 10^{-4}$ |
| $w_{2,coded}$ | 0.012836 | 0.012889 |
| $\lambda_{coded}h_{coded}$ | $-0.001686$ | $-0.001595$ |
| $\lambda_{coded}w_{2,coded}$ | 0.002073 | 0.002164 |
| $\lambda^2_{coded}$ | $-0.005773$ | $-0.005630$ |
| $\lambda^3_{coded}$ | 0.002883 | 0.003165 |

Table 4.4: Confidence intervals for Y-branch $\lvert S_{31}\rvert^2$ RSM fit.

$$\begin{aligned}|S_{22}|^2 \approx\ & 0.005965 + 5.8633 \cdot 10^{-3}\lambda_{coded} - 8.8242 \cdot 10^{-4}w_{1,coded} \\ & - 1.0408 \cdot 10^{-3}h_{coded} + 1.2469 \cdot 10^{-4}w_{2,coded} - 1.4114 \cdot 10^{-4}\lambda_{coded}w_{1,coded} \\ & + 8.8572 \cdot 10^{-4}\lambda_{coded}h_{coded} + 1.1081 \cdot 10^{-4}\lambda_{coded}w_{2,coded} - 1.0760 \cdot 10^{-3}\lambda^2_{coded} \\ & - 1.8324 \cdot 10^{-3}\lambda^3_{coded}\end{aligned} \tag{4.22}$$

| Results for $\lvert S_{22}\rvert^2$ Fit | | |
|---|---|---|
| Model Coefficient | Negative Conf. Interval | Positive Conf. Interval |
| Constant Term | 0.005953 | 0.005977 |
| $\lambda_{coded}$ | 0.005829 | 0.005898 |
| $w_{1,coded}$ | $-8.9215 \cdot 10^{-4}$ | $-8.7269 \cdot 10^{-4}$ |
| $h_{coded}$ | $-0.001051$ | $-0.001031$ |
| $w_{2,coded}$ | $1.1496 \cdot 10^{-4}$ | $1.3442 \cdot 10^{-4}$ |
| $\lambda_{coded} w_{1,coded}$ | $-1.5797 \cdot 10^{-4}$ | $-1.2431 \cdot 10^{-4}$ |
| $\lambda_{coded} h_{coded}$ | $8.6889 \cdot 10^{-4}$ | $9.0255 \cdot 10^{-4}$ |
| $\lambda_{coded} w_{2,coded}$ | $9.3977 \cdot 10^{-5}$ | $1.2764 \cdot 10^{-4}$ |
| $\lambda^2_{coded}$ | $-0.001103$ | $-0.001049$ |
| $\lambda^3_{coded}$ | $-0.001885$ | $-0.001780$ |

Table 4.5: Confidence intervals for Y-branch $\lvert S_{22}\rvert^2$ RSM fit.

$$\begin{aligned} |S_{23}|^2 \approx\ & 0.003546 + 0.005227\lambda_{coded} - 9.9732 \cdot 10^{-5} w_{1,coded} \\ & - 0.001367 h_{coded} - 9.5337 \cdot 10^{-5} w_{2,coded} + 6.7644 \cdot 10^{-5} \lambda_{coded} w_{1,coded} \\ & - 9.5153 \cdot 10^{-4} \lambda_{coded} h_{coded} + 9.0982 \cdot 10^{-5} \lambda_{coded} w_{2,coded} + 0.001750 \lambda^2_{coded} \\ & - 4.5282 \cdot 10^{-4} \lambda^3_{coded} \end{aligned} \tag{4.23}$$

| Results for $\lvert S_{23}\rvert^2$ Fit | | |
|---|---|---|
| Model Coefficient | Negative Conf. Interval | Positive Conf. Interval |
| Constant Term | 0.003542 | 0.003551 |
| $\lambda_{coded}$ | 0.005215 | 0.005240 |
| $w_{1,coded}$ | $-1.0328 \cdot 10^{-4}$ | $-9.6181 \cdot 10^{-5}$ |
| $h_{coded}$ | $-0.001370$ | $-0.001363$ |
| $w_{2,coded}$ | $-9.8889 \cdot 10^{-5}$ | $-9.1785 \cdot 10^{-5}$ |
| $\lambda_{coded} w_{1,coded}$ | $6.1501 \cdot 10^{-5}$ | $7.3787 \cdot 10^{-5}$ |
| $\lambda_{coded} h_{coded}$ | $-9.5767 \cdot 10^{-4}$ | $-9.4538 \cdot 10^{-4}$ |
| $\lambda_{coded} w_{2,coded}$ | $8.4839 \cdot 10^{-5}$ | $9.7125 \cdot 10^{-5}$ |
| $\lambda^2_{coded}$ | 0.001741 | 0.001760 |
| $\lambda^3_{coded}$ | $-4.7193 \cdot 10^{-4}$ | $-4.337 \cdot 10^{-4}$ |

Table 4.6: Confidence intervals for Y-branch $\lvert S_{23}\rvert^2$ RSM fit.

$$\begin{aligned} |S_{33}|^2 \approx\ & 0.005965 + 5.8610 \cdot 10^{-3}\lambda_{coded} + 1.2468 \cdot 10^{-4} w_{1,coded} \\ & - 1.0404 \cdot 10^{-3} h_{coded} - 8.8240 \cdot 10^{-4} w_{2,coded} + 1.1080 \cdot 10^{-4} \lambda_{coded} w_{1,coded} \\ & + 8.8651 \cdot 10^{-4} \lambda_{coded} h_{coded} - 1.3923 \cdot 10^{-4} \lambda_{coded} w_{2,coded} - 1.0767 \cdot 10^{-3} \lambda^2_{coded} \\ & - 1.8305 \cdot 10^{-3} \lambda^3_{coded} \end{aligned} \tag{4.24}$$

| Results for $\lvert S_{33}\rvert^2$ Fit | | |
|---|---|---|
| Model Coefficient | Negative Conf. Interval | Positive Conf. Interval |
| Constant Term | 0.005953 | 0.005977 |
| $\lambda_{coded}$ | 0.005827 | 0.005896 |
| $w_{1,coded}$ | $1.1495 \cdot 10^{-4}$ | $1.3442 \cdot 10^{-4}$ |
| $h_{coded}$ | $-0.001050$ | $-0.001031$ |
| $w_{2,coded}$ | $-8.9213 \cdot 10^{-4}$ | $-8.7267 \cdot 10^{-4}$ |
| $\lambda_{coded} w_{1,coded}$ | $9.3964 \cdot 10^{-5}$ | $1.2763 \cdot 10^{-4}$ |
| $\lambda_{coded} h_{coded}$ | $8.6968 \cdot 10^{-4}$ | $9.0335 \cdot 10^{-4}$ |
| $\lambda_{coded} w_{2,coded}$ | $-1.5606 \cdot 10^{-4}$ | $-1.2239 \cdot 10^{-4}$ |
| $\lambda^2_{coded}$ | $-0.001103$ | $-0.001050$ |
| $\lambda^3_{coded}$ | $-0.001883$ | $-0.001778$ |

Table 4.7: Confidence intervals for Y-Branch $\lvert S_{33}\rvert^2$ RSM fit.

Equations 4.19 - 4.24 are the response surface models found using the method. The model forms for $\lvert S_{21}\rvert^2$ and $\lvert S_{31}\rvert^2$ differ in their linear terms' model coefficients. The former fit, which corresponds to the relative power transmission in the upper branch, has a negative $w_2$ term; the latter fit, which describes the relative power transmission in the lower branch, has a negative $w_1$ term. Intuitively, we expect more relative power to be transmitted through the wider output branch. This behavior is captured by the negative terms; power transmitted in one branch is weakly dependent on the width of the other branch. The fits also differ in their cross terms. The $\lvert S_{21}\rvert^2$ RSM contains a $\lambda w_1$ term; in another fit, the $\lambda w_2$ term was found to be insignificant and was omitted. Similarly, $\lvert S_{31}\rvert^2$ contains a $\lambda w_2$ term, but the corresponding $\lambda w_1$ term was found to be insignificant to the model.

### 4.2.2 ANOVA Results

The analysis of variance results for each of the modeled S-parameters are demonstrated in Tables 4.8 - 4.13. We see that the models are all highly significant, with p-values less than $10^{-19}$.

| ANOVA Results for $\|S_{11}\|^2$ Fit | | | |
|---|---|---|---|
| Source of Variation | Degrees of Freedom | Sum of Squares | Mean Square |
| Fitted Model | 9 | 0.0369 | $4.1010 \cdot 10^{-4}$ |
| Residuals | 14990 | $1.6841 \cdot 10^{-4}$ | $1.1235 \cdot 10^{-8}$ |
| Total | 14999 | 0.0386 | |
| F-Ratio | $F = 36,503$ | $F_{critical} = 1.8805$ | |
| P-Value | $4.9038 \cdot 10^{-20}$ | | |

Table 4.8: ANOVA results for Y-branch $|S_{11}|^2$ RSM fit.

| ANOVA Results for $\|S_{21}\|^2$ Fit | | | |
|---|---|---|---|
| Source of Variation | Degrees of Freedom | Sum of Squares | Mean Square |
| Fitted Model | 8 | 2.2050 | 0.2756 |
| Residuals | 14991 | $2.6858 \cdot 10^{-2}$ | $1.7961 \cdot 10^{-6}$ |
| Total | 14999 | 2.2553 | |
| F-Ratio | $F = 153,836$ | $F_{critical} = 1.9390$ | |
| P-Value | $1.9060 \cdot 10^{-20}$ | | |

Table 4.9: ANOVA results for Y-branch $|S_{21}|^2$ RSM fit.

| ANOVA Results for $\lvert S_{31}\rvert^2$ Fit | | | |
|---|---|---|---|
| Source of Variation | Degrees of Freedom | Sum of Squares | Mean Square |
| Fitted Model | 8 | 2.2051 | 0.2756 |
| Residuals | 14991 | $2.6828 \cdot 10^{-2}$ | $1.7896 \cdot 10^{-6}$ |
| Total | 14999 | 2.2319 | |
| F-Ratio | $F = 154,018$ | $F_{critical} = 1.9390$ | |
| P-Value | $1.8971 \cdot 10^{-20}$ | | |

Table 4.10: ANOVA results for Y-branch $|S_{31}|^2$ RSM fit.

| ANOVA Results for $\lvert S_{22}\rvert^2$ Fit | | | |
|---|---|---|---|
| Source of Variation | Degrees of Freedom | Sum of Squares | Mean Square |
| Fitted Model | 9 | 0.1389 | 0.01543 |
| Residuals | 14990 | $3.6894 \cdot 10^{-3}$ | $2.4613 \cdot 10^{-7}$ |
| Total | 14999 | 0.1421 | |
| F-Ratio | $F = 62,685$ | $F_{critical} = 1.8805$ | |
| P-Value | $4.3033 \cdot 10^{-21}$ | | |

Table 4.11: ANOVA results for Y-branch $|S_{22}|^2$ RSM fit.

| ANOVA Results for $\lvert S_{23}\rvert^2$ Fit | | | |
|---|---|---|---|
| Source of Variation | Degrees of Freedom | Sum of Squares | Mean Square |
| Fitted Model | 9 | 0.1471 | 0.01634 |
| Residuals | 14990 | $4.9151 \cdot 10^{-4}$ | $3.2789 \cdot 10^{-8}$ |
| Total | 14999 | 0.1475 | |
| F-Ratio | $F = 498,299$ | $F_{critical} = 1.8805$ | |
| P-Value | $3.8225 \cdot 10^{-25}$ | | |

Table 4.12: ANOVA results for Y-branch $|S_{23}|^2$ RSM fit.

| ANOVA Results for $\lvert S_{33}\rvert^2$ Fit | | | |
|---|---|---|---|
| Source of Variation | Degrees of Freedom | Sum of Squares | Mean Square |
| Fitted Model | 9 | 0.1388 | 0.01542 |
| Residuals | 14990 | $3.6913 \cdot 10^{-3}$ | $2.4625 \cdot 10^{-7}$ |
| Total | 14999 | 0.1425 | |
| F-Ratio | $F = 62,627$ | $F_{critical} = 1.8805$ | |
| P-Value | $4.3212 \cdot 10^{-21}$ | | |

Table 4.13: ANOVA results for Y-branch $\lvert S_{33}\rvert^2$ RSM fit.

Table 4.14 shows the $R^2$ and adjusted $R^2$ values for each of the RSM fit equations. The fits for all of the S-parameters have an $R^2$ value very close to one; as a result, these fits can be used to accurately model device variations. The models each have an adjusted $R^2$ value that is equal to the corresponding $R^2$ value. The terms introduced in the model are all significant and do not overfit to the observations.

| $R^2$ Results for RSM Fit | | |
|---|---|---|
| S-Parameter RSM Fit | $R^2$ Value | Adjusted $R^2$ Value |
| $\lvert S_{11}\rvert^2$ | 0.956 | 0.956 |
| $\lvert S_{21}\rvert^2$ | 0.988 | 0.988 |
| $\lvert S_{31}\rvert^2$ | 0.988 | 0.988 |
| $\lvert S_{22}\rvert^2$ | 0.974 | 0.974 |
| $\lvert S_{23}\rvert^2$ | 0.997 | 0.997 |
| $\lvert S_{33}\rvert^2$ | 0.974 | 0.974 |

Table 4.14: $R^2$ Results for proposed Y-branch RSM Fit model.

### 4.2.3 Estimation of Effects of Random Variations

Now that the numerical model is constructed, it can be used to estimate the effects of randomized variations. To demonstrate the use of the model, 100 different simulations are run. The set of parameter values used for each simulation are chosen at random; each value is independently sampled from the following Gaussian distributions, where we have assumed the three-sigma deviations are 5% of the nominal (mean) values:

$$h_{sampled} \sim \mathcal{N}(\mu \ = \ 220 \ nm, \ 3\sigma \ = \ 11 \ nm) \tag{4.25}$$

$$w_{1,sampled} \sim \mathcal{N}(\mu \ = \ 500 \ nm, \ 3\sigma \ = \ 25 \ nm) \tag{4.26}$$

$$w_{2,sampled} \sim \mathcal{N}(\mu \ = \ 500 \ nm, \ 3\sigma \ = \ 25 \ nm) \tag{4.27}$$

A model prediction of the device performance is also evaluated at the operating points determined from the randomly-chosen parameter set.

We apply the Y-branch response surface model on a set of 100 random samples using the distributions described by Equations 4.25, 4.26, and 4.27. The relative power transmission predicted from modeling $|S_{21}|^2$ and $|S_{31}|^2$ is measured at $\lambda \ = \ 1550 \ nm$. Figure 4.1 summarizes the results in a quantile-quantile plot. The dashed line represents a Gaussian distribution.

Based on the set of random Monte-Carlo simulations here, we can estimate the Y-branch output statistical performance, corresponding to the input variations in Equations 4.25 to 4.27. We find that the relative transmitted power in the upper branch is approximately $T_{upper} \sim \mathcal{N}(\mu \ = \ 0.484, 3\sigma \ = \ 0.006)$ or with a $\pm 3\sigma$ range from 0.478 to 0.490. This can be compared to the worst-case output corners found in Section 3.2 for the Y-branch, where the minimum and maximum upper port transmissions in Table 3.2 were 0.464 and 0.504, respectively. Thus the worst case corners can be seen to be somewhat pessimistic compared to the jointly considered statistical model.

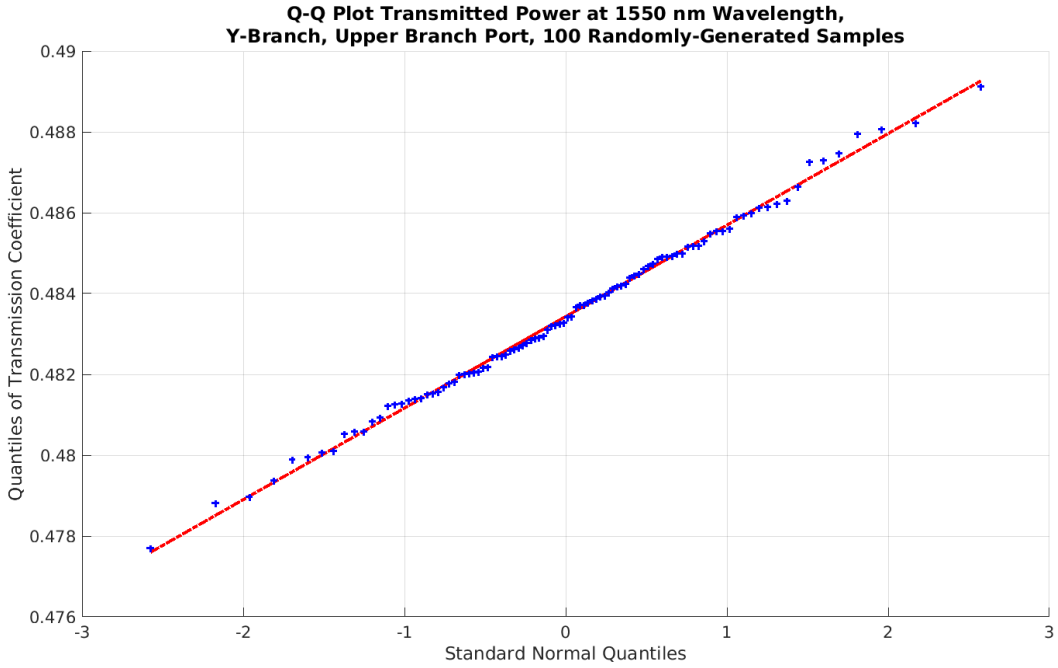


(a) Upper Branch QQ plot.

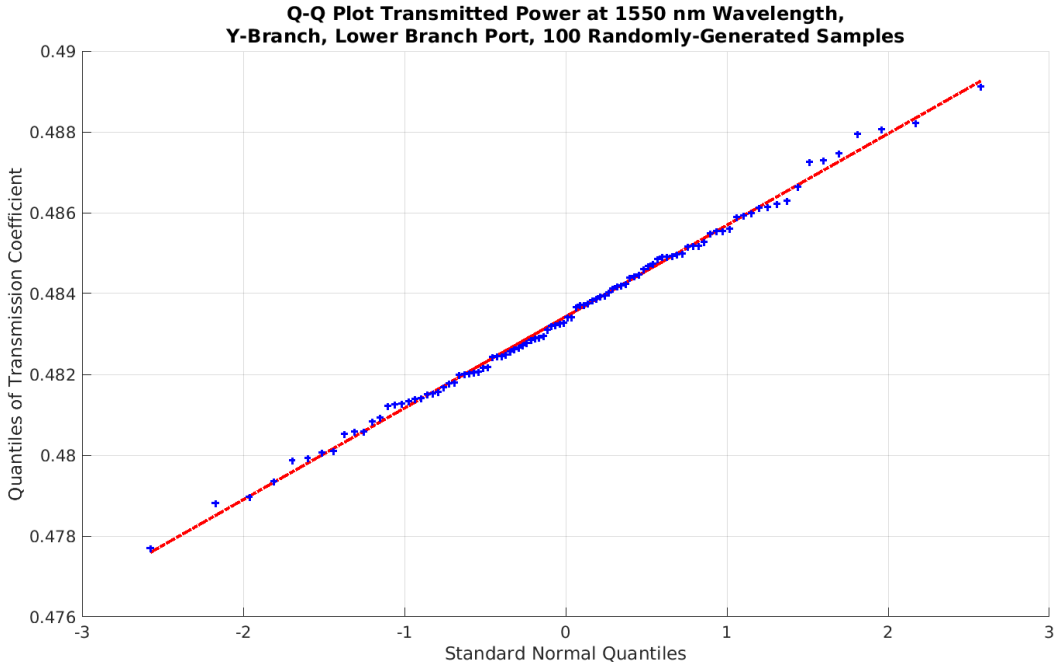


(b) Lower Branch QQ plot.

Figure 4.1: Results from testing 100 random samples on the Y-branch response surface model. The response at $\lambda = 1550\ nm$ is recorded for each sample.

In the example shown here, independent variations are assumed for $h$, $w_1$, and $w_2$. The

same statistical sampling approach can also be used in the case where some correlation structure exists between the input parameters. In such cases, for example, random samples of $h$, $w_1$, and $w_2$ can be generated based on a measured or assumed covariance matrix $\mathbf{\Sigma}$, and simulations run with those samples. Such correlated statistical simulations can be a powerful approach to reduce the potential pessimism in using independent worst case corner models.

It is also possible to simulate every random sample case in Lumerical FDTD, and perform this same analysis. However, this method would take thousands of times longer by using a response surface model, where results can be obtained from MATLAB and exported to INTERCONNECT in a few seconds. Further efficiencies can be gained by using advanced stochastic sampling approaches that require fewer sample points than standard Monte-Carlo [30, 31]. These approaches have great potential for silicon photonics.

### 4.2.4 Compact Model Creation

A parametric compact model can be constructed from the response surface model of the Y-branch, that is different from or complements the discrete corner-based compact model. In this case, the response surface model is in the form of a function or procedure (in MATLAB) that returns the respective S-parameter given the device geometry of interest. When augmented with statistics on the inputs (as in Equations 4.25 to 4.27) and potentially including covariance structure $\mathbf{\Sigma}$, we refer to this as a statistical compact model.

## 4.3 Directional Coupler Response Surface Model

In this section, the analogous process of creating a compact response surface model for a directional coupler device is discussed. The results of fitting the DoE simulation results to a response surface are discussed. Building upon the corner analysis results that are described in Section 3.3.3, RSM compact models for the directional coupler are presented. The results

can be contrasted to a nominal directional coupler; the operation is discussed earlier in Section 3.3.2.

### 4.3.1 RSM Equation Model

For the 50/50 directional coupler, the response surface model is formed using the results from the three-parameter DoE, as presented previously in Section 3.3.3. Four parameters are selected as the model fitting parameters: the free-space wavelength $\lambda$, the coupling gap between the two waveguides (denoted as $L_g$), the waveguide thickness $h$, and the waveguide width $w$. The waveguide thickness and waveguide width are perturbed across the entire device; both waveguides are modified simultaneously. The observations used to form the model are the results from the central composite design, as discussed in Section 2.1.2. This design is also used to form the input variations that correspond to those observations. Further, the device operation is found for free-space wavelengths along the range of $\lambda = 1500$ to $1600\ nm$. Within this range of values for $\lambda$, 1000 evenly spaced wavelength samples are taken from the simulation results.

For each fitting parameter, we use the following coded variable representation for each parameter tested:

$$\lambda_{coded} = \frac{\lambda - 2(1600nm + 1500nm)}{1600nm - 1500nm} \tag{4.28}$$

$$L_{g,coded} = \frac{L_g - 2(210nm + 190nm)}{210nm - 190nm} \tag{4.29}$$

$$h_{coded} = \frac{h - 2(231nm + 209nm)}{231nm - 209nm} \tag{4.30}$$

$$w_{coded} = \frac{w - 2(525nm + 475nm)}{525nm - 475nm}. \tag{4.31}$$

The directional coupler has 16 different S-parameters to fit on an individual basis; this number arises from applying the source light at the different ports available. However, only four of the 16 S-parameters actually need to be fit to construct a complete variation compact model. The three variations tested ($L_g$, $w$, and $h$) are applied to both waveguides, resulting

in a symmetric relationship between the S-parameters of the device:

$$\begin{aligned} S_{11} = S_{22} &= S_{33} = S_{44} \\ S_{21} = S_{12} &= S_{43} = S_{34} \\ S_{31} = S_{42} &= S_{13} = S_{24} \\ S_{41} = S_{32} &= S_{23} = S_{14} \end{aligned} \tag{4.32}$$

Each of these S-parameters are dependent on wavelength; an S-parameter is required for every wavelength point measured. Since the wavelength is a fitting parameter in the RSM, it is not necessary to construct a separate response surface for every single wavelength. Every measured wavelength point for every test case is included as an observation, so only one surface is required for each S-parameter. S-parameters are complex-valued, so it is necessary to model both the magnitude and phase. Thus, there are eight different response surfaces to construct.

In the case of modeling $|S_{11}|$ and $|S_{21}|$, the best that can be done is to model the amplitude of the S-parameter as an average linear dependence with respect to $L_g$ and $w$ [11]. In simulation, the measured values of these S-parameters are found to vary between $10^{-6}$ and $10^{-9}$ across the different $L_g$ and $w$ test cases in an oscillatory rather than strictly linear fashion. This range covers three orders of magnitude, but the values themselves are very small compared to those of $|S_{31}|$ and $|S_{41}|$. Because these S-parameters exhibit oscillatory behavior across $L_g$ and $w$, it is difficult to fit a response surface to this oscillatory behavior with only $\pm 5\%$ variations in $L_g$ and $w$. A more accurate response surface would incorporate the $\pm 1\%$ corner variations, together with the $\pm 5\%$ variations, to support even higher order model terms. Here, the $\pm 5\%$ variations only are used to ensure consistency in the model. However, the values themselves are small, and thus these small inaccuracies have a small effect on the overall performance in a compact model. Thus an average linear model for $|S_{11}|$ and $|S_{21}|$ with respect to $L_g$ and $w$ is adequate.

$$|S_{11}|^2 \approx 3.1868 \cdot 10^{-6} + 2.0585 \cdot 10^{-6}\lambda_{coded} - 7.2223 \cdot 10^{-7}w_{coded} + 2.2328 \cdot 10^{-6}h_{coded} - 1.1234 \cdot 10^{-6}\lambda_{coded}w_{coded} + 4.9320 \cdot 10^{-7}\lambda_{coded}h_{coded} \tag{4.33}$$

| Results for $\|S_{11}\|^2$ Fit | | |
|---|---|---|
| Model Coefficient | Negative Conf. Interval | Positive Conf. Interval |
| Constant Term | $3.1265 \cdot 10^{-6}$ | $3.1617 \cdot 10^{-6}$ |
| $\lambda_{coded}$ | $1.9889 \cdot 10^{-6}$ | $2.1316 \cdot 10^{-6}$ |
| $w_{coded}$ | $-7.7155 \cdot 10^{-7}$ | $-6.7285 \cdot 10^{-7}$ |
| $h_{coded}$ | $2.1835 \cdot 10^{-6}$ | $2.2822 \cdot 10^{-6}$ |
| $\lambda_{coded}w_{coded}$ | $-1.2087 \cdot 10^{-6}$ | $-1.0380 \cdot 10^{-6}$ |
| $\lambda_{coded}h_{coded}$ | $4.0790 \cdot 10^{-7}$ | $5.7861 \cdot 10^{-7}$ |

Table 4.15: Confidence intervals for directional coupler $|S_{11}|^2$ RSM fit.

$$|S_{21}|^2 \approx 8.4593 \cdot 10^{-8} + 2.4980 \cdot 10^{-8}\lambda_{coded} - 1.7383 \cdot 10^{-8}L_{g,coded} + 9.0173 \cdot 10^{-8}w_{coded} + 1.06527 \cdot 10^{-7}h_{coded} \tag{4.34}$$

| Results for $\|S_{21}\|^2$ Fit | | |
|---|---|---|
| Model Coefficient | Negative Conf. Interval | Positive Conf. Interval |
| Constant Term | $8.2462 \cdot 10^{-8}$ | $8.6725 \cdot 10^{-8}$ |
| $\lambda_{coded}$ | $2.1294 \cdot 10^{-8}$ | $2.8666 \cdot 10^{-8}$ |
| $L_{g,coded}$ | $-1.9991 \cdot 10^{-8}$ | $-1.4774 \cdot 10^{-8}$ |
| $w_{coded}$ | $8.7565 \cdot 10^{-8}$ | $9.2782 \cdot 10^{-8}$ |
| $h_{coded}$ | $1.0391 \cdot 10^{-7}$ | $1.0913 \cdot 10^{-7}$ |

Table 4.16: Confidence intervals for directional coupler $|S_{21}|^2$ RSM fit.

$$
\begin{aligned}
|S_{31}|^2 \approx\ & 0.5255 - 0.1637\lambda_{coded} + 0.06305L_{g,coded} \\
& + 0.1526w_{coded} + 0.06132h_{coded} + 0.006868\lambda_{coded}L_{g,coded} \\
& + 0.03045\lambda_{coded}w_{coded} + 0.01360\lambda_{coded}h_{coded} - 0.009573L_{g,coded}w_{coded} \\
& - 0.001654L_{g,coded}h_{coded} - 0.009712w_{coded}h_{coded} - 0.01397\lambda_{coded}^2 \\
& - 0.002492L_{g,coded}^2 - 0.01966w_{coded}^2
\end{aligned} \tag{4.35}
$$

| Results for $\lvert S_{31}\rvert^2$ Fit | | |
|---|---|---|
| Model Coefficient | Negative Conf. Interval | Positive Conf. Interval |
| Constant Term | 0.5252 | 0.5257 |
| $\lambda_{coded}$ | $-0.1639$ | $-0.1635$ |
| $L_{g,coded}$ | 0.06293 | 0.06319 |
| $w_{coded}$ | 0.1524 | 0.1527 |
| $h_{coded}$ | 0.06119 | 0.06145 |
| $\lambda_{coded}L_{g,coded}$ | 0.03022 | 0.007096 |
| $\lambda_{coded}w_{coded}$ | 0.006639 | 0.03067 |
| $\lambda_{coded}h_{coded}$ | 0.01337 | 0.01383 |
| $L_{g,coded}w_{coded}$ | $-0.009721$ | $-0.009426$ |
| $L_{g,coded}h_{coded}$ | $-0.001801$ | $-0.001506$ |
| $w_{coded}h_{coded}$ | $-0.009860$ | $-0.009565$ |
| $\lambda_{coded}^2$ | $-0.01433$ | $-0.01361$ |
| $L_{g,coded}^2$ | $-0.002757$ | $-0.002259$ |
| $w_{coded}^2$ | $-0.01993$ | $-0.01943$ |

Table 4.17: Confidence intervals for directional coupler $|S_{31}|^2$ RSM fit.

$$
\begin{aligned}
|S_{41}|^2 \approx\ & 0.4768 + 0.1585\lambda_{coded} - 0.06311L_{g,coded} \\
& - 0.1476w_{coded} - 0.05244h_{coded} - 0.006785\lambda_{coded}L_{g,coded} \\
& - 0.02604\lambda_{coded}w_{coded} - 0.003135\lambda_{coded}h_{coded} + 0.009573L_{g,coded}w_{coded} \\
& + 0.001596L_{g,coded}h_{coded} + 0.006203w_{coded}h_{coded} + 0.005947\lambda_{coded}^2 \\
& + 0.002613L_{g,coded}^2 + 0.01838w_{coded}^2 + 5.3829 \cdot 10^{-4}h_{coded}^2
\end{aligned}
\tag{4.36}
$$

| Results for $\lvert S_{41}\rvert^2$ Fit | | |
|---|---|---|
| Model Coefficient | Negative Conf. Interval | Positive Conf. Interval |
| Constant Term | 0.4765 | 0.4770 |
| $\lambda_{coded}$ | 0.1584 | 0.1587 |
| $L_{g,coded}$ | $-0.06324$ | $-0.06298$ |
| $w_{coded}$ | $-0.1477$ | $-0.1475$ |
| $h_{coded}$ | $-0.05257$ | $-0.05232$ |
| $\lambda_{coded}L_{g,coded}$ | $-0.007006$ | $-0.006565$ |
| $\lambda_{coded}w_{coded}$ | 0.02626 | $-0.2582$ |
| $\lambda_{coded}h_{coded}$ | $-0.003355$ | $-0.002914$ |
| $L_{g,coded}w_{coded}$ | 0.009430 | 0.009715 |
| $L_{g,coded}h_{coded}$ | 0.001454 | 0.001739 |
| $w_{coded}h_{coded}$ | 0.006061 | 0.006346 |
| $\lambda_{coded}^2$ | 0.005599 | 0.6296 |
| $L_{g,coded}^2$ | 0.002362 | 0.002864 |
| $w_{coded}^2$ | 0.01813 | 0.01863 |
| $h_{coded}^2$ | $2.8693 \cdot 10^{-4}$ | $7.8965 \cdot 10^{-4}$ |

Table 4.18: Confidence intervals for directional coupler $|S_{41}|^2$ RSM fit.

The proposed model equations for $|S_{31}|^2$ and $|S_{41}|^2$ consist of a linear term in $L_{g,coded}$, $w_{coded}$, and $h_{coded}$, but also includes cross terms between the geometric parameters. The model coefficients for each cross term are all an order of magnitude smaller than the smallest linear term, indicating that the cross terms, while significant, have a relatively small effect. This slight nonlinearity in the model was predicted in the sensitivity analysis performed in Section 3.3.4.

### 4.3.2 ANOVA Results

The analysis of variance results for each of the modeled S-parameters are demonstrated in Tables 4.19 - 4.22. Again, the models proposed here are all significant; the RSMs for these models all have p-values less than $10^{-6}$.

| ANOVA Results for $\|S_{11}\|^2$ Fit | | | |
|---|---|---|---|
| Source of Variation | Degrees of Freedom | Sum of Squares | Mean Square |
| Fitted Model | 9 | $8.0570 \cdot 10^{-8}$ | $1.6114 \cdot 10^{-8}$ |
| Residuals | 14990 | $9.5017 \cdot 10^{-8}$ | $6.3370 \cdot 10^{-12}$ |
| Total | 14999 | $1.7559 \cdot 10^{-7}$ | |
| F-Ratio | $F = 2,542.8$ | $F_{critical} = 2.2147$ | |
| P-Value | $9.1155 \cdot 10^{-9}$ | | |

Table 4.19: ANOVA results for directional coupler $|S_{11}|^2$ RSM fit.

| ANOVA Results for $\lvert S_{21}\rvert^2$ Fit | | | |
|---|---|---|---|
| Source of Variation | Degrees of Freedom | Sum of Squares | Mean Square |
| Fitted Model | 8 | $2.0093 \cdot 10^{-10}$ | $5.0233 \cdot 10^{-11}$ |
| Residuals | 14991 | $2.6555 \cdot 10^{-10}$ | $1.7709 \cdot 10^{-14}$ |
| Total | 14999 | $4.6648 \cdot 10^{-10}$ | |
| F-Ratio | $F = 2,836.5$ | $F_{critical} = 2.3725$ | |
| P-Value | $2.4849 \cdot 10^{-7}$ | | |

Table 4.20: ANOVA results for directional coupler $|S_{21}|^2$ RSM fit.

| ANOVA Results for $\lvert S_{31}\rvert^2$ Fit | | | |
|---|---|---|---|
| Source of Variation | Degrees of Freedom | Sum of Squares | Mean Square |
| Fitted Model | 13 | 448.38 | 34.4909 |
| Residuals | 14986 | 0.6776 | $4.5214 \cdot 10^{-5}$ |
| Total | 14999 | 449.06 | |
| F-Ratio | $F = 762,835$ | $F_{critical} = 1.7208$ | |
| P-Value | $5.9846 \cdot 10^{-37}$ | | |

Table 4.21: ANOVA results for directional coupler $|S_{31}|^2$ RSM fit.

| ANOVA Results for $\lvert S_{41}\rvert^2$ Fit | | | |
|---|---|---|---|
| Source of Variation | Degrees of Freedom | Sum of Squares | Mean Square |
| Fitted Model | 14 | 413.81 | 29.5580 |
| Residuals | 14985 | 0.8998 | $6.0044 \cdot 10^{-5}$ |
| Total | 14999 | 414.71 | |
| F-Ratio | $F = 492,273$ | $F_{critical} = 1.6924$ | |
| P-Value | $2.3390 \cdot 10^{-38}$ | | |

Table 4.22: ANOVA results for directional coupler $|S_{41}|^2$ RSM fit.

Table 4.23 shows the $R^2$ and adjusted $R^2$ values for each of the RSM fit equations. The response surface fits for $|S_{11}|^2$ and $|S_{21}|^2$ are poor, as the $R^2$ results are low. As explained in Section 4.3.1, the models can only describe an average value because of the oscillatory behavior of the two S-parameters. More accurate models can be constructed with more model coefficients, but the cost is added complexity. The actual values for these parameters are very small, so a tighter fit is not necessary. The fits for $|S_{31}|^2$ and $|S_{41}|^2$ have an $R^2$ value close to one and a matching adjusted $R^2$ value; as a result, these fits can be used to reliably model device variations.

| $R^2$ Results for RSM Fit | | |
|---|---|---|
| S-Parameter RSM Fit | $R^2$ Value | Adjusted $R^2$ Value |
| $\|S_{11}\|^2$ | 0.4587 | 0.4589 |
| $\|S_{21}\|^2$ | 0.4306 | 0.4307 |
| $\|S_{31}\|^2$ | 0.9985 | 0.9985 |
| $\|S_{41}\|^2$ | 0.9978 | 0.9978 |

Table 4.23: $R^2$ results for proposed directional coupler RSM Fit model.

## 4.4 Summary

In this chapter, the response surface method for generating a variation-aware compact model of photonic devices has been demonstrated. Building upon the corner analysis models in Chapter 3, two examples are discussed. The first example describes the procedure in the context of the Y-branch. The second example focuses on the modeling procedure as applied to the directional coupler device; here, only the three-parameter DoE results are considered as observations. The method creates variation-aware compact models that can predict device-to-device variations of a photonics design.

# Chapter 5

# Photonic Circuit Simulation Using Compact Modeling Methods

Chapters 3 and 4 demonstrated different methods to create variation compact models. This chapter demonstrates applications of the different device-level compact modeling techniques to the analysis of variation at the photonic circuit-level. For all of the examples in this chapter, the photonic circuits are described and simulated using Lumerical INTERCONNECT software.

## 5.1 Discussion of the Mach-Zehnder Interferometer

The Mach-Zehnder Interferometer is a photonic circuit that acts as a wavelength filter. It consists of an input waveguide that splits light into two branches. Light is carried some distance across the two branch waveguides; it is then recombined at the output. The circuit can thus be considered a single-input, single-output system. The filtering behavior at different wavelengths is determined by the amount of interference between the two branches as the light is recombined. Typical MZI designs can be unbalanced; in such designs, one branch is made longer than the other branch to introduce interference at (filter out) certain wavelengths of light. The MZI examples considered in this thesis are balanced; the splitting

branches are defined to be the same length. The splitting/recombination components of the circuit can be implemented using Y-branches or directional couplers; this thesis considers MZI circuit designs using either of the two components.

Figure 5.1 shows a nominal MZI circuit in INTERCONNECT using Y-branch components. Light is fed into the circuit through the input port of the left side Y-branch using the output of the Optical Network Analyzer (the "ONA_nominal") component. The right side Y-branch is used as a combiner and the light at the output is measured with the ONA at input 1. Because the Y-branch is passive and linear, reciprocity applies and the same S-parameter model can be used with careful handling of ports when the Y-branch is used as a combiner (at right in Figure 5.1) as when used as a splitter (at left in Figure 5.1). For use in INTERCONNECT, S-parameter models including both magnitude and phase are used, generate by the methods presented in Chapters 3 and 4.

Figure 5.2 shows the relative power transmission measured at the output of the nominal directional coupler MZI. In this configuration, the MZI response resembles a summation of the two output branches (see Figure 3.2). The relative transmitted power measured at the output port increases until around $\lambda = 1545\ nm$. For the range of $\lambda = 1545$ to $1600\ nm$, the output power is wavelength-dependent and oscillates around a mean value of 0.936. We contrast this with the relative power measured from the outputs of the nominal Y-branch design; over the same wavelength range, the output power is more nearly constant. This oscillatory behavior is due to the interference of light at the combiner Y-branch, based on wavelength-dependent phase and optical path lengths in the overall splitter-combiner structure.

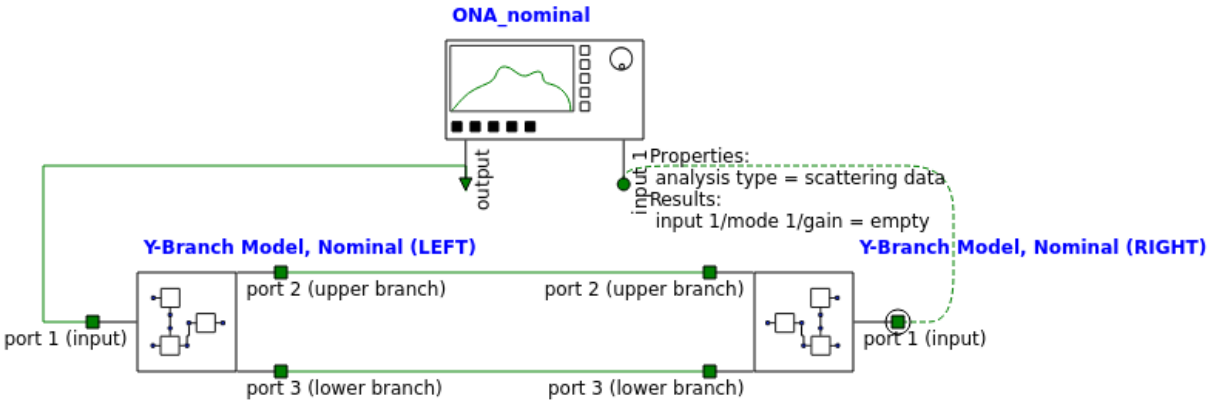


Figure 5.1: An MZI circuit simulation configuration using Y-branch compact models.

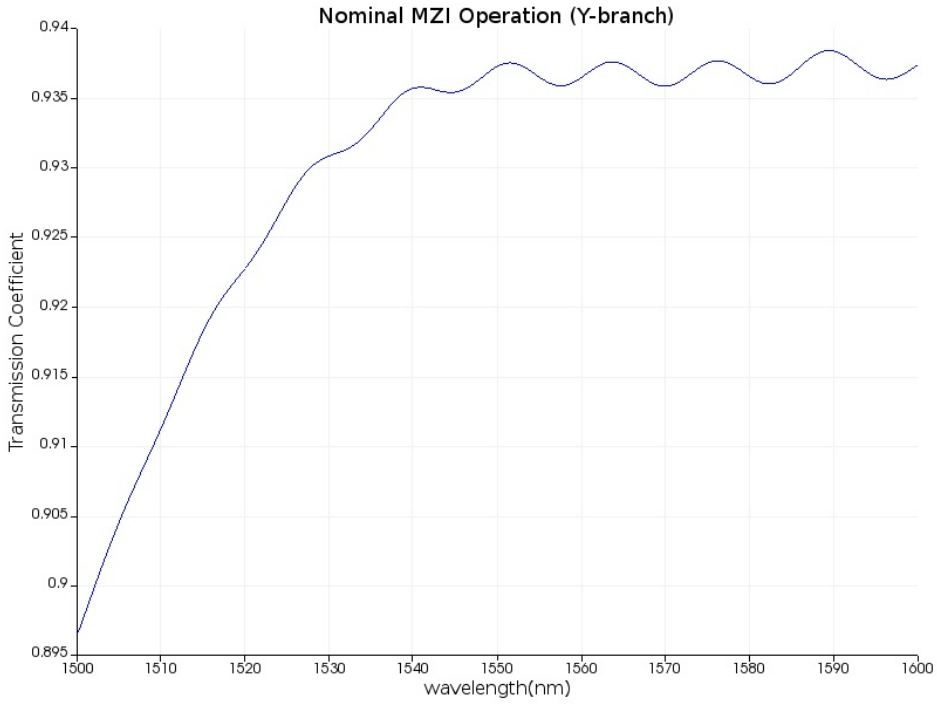


Figure 5.2: Nominal Y-branch MZI simulation results. The compact models used are the nominal Y-branch device discussed in Section 3.2.2. Relative transmitted power is measured at the output across the range of $\lambda = 1500$ to 1600 $nm$.

The MZI circuit can also be constructed using the directional coupler. Figure 5.3 shows a nominal MZI circuit using directional coupler components. Using the Optical Network Analyzer component ("ONA_nominal"), light is fed into the circuit through the input port of the left side directional coupler. The output light is measured by the ONA at the cross

port of the right side directional coupler. In the case of using the directional coupler as a combiner, port 2 of the device is important, and the S-paramerter models for magnitude and phase include this port also, again generated using the methods of Chapters 3 and 4.

Figure 5.4 shows the relative power transmission of the directional coupler MZI. In this balanced configuration, the MZI response resembles a very broad band-pass filter. The relative transmitted power measured at the output port peaks at around $\lambda = 1560\ nm$. This free-space wavelength is where the relative power transmitted across the through and cross ports of the nominal directional coupler design is equal. Unlike the Y-branch MZI, the balanced directional coupler MZI does not show frequency-dependent oscillation behavior through the $\lambda = 1500\ to\ 1600\ nm$ band. In conventional use, the MZI would be unbalanced and include an additional waveguide element in one branch of the MZI, designed to introduce path-length differences such that filtering is achieved at desired wavelengths. The same approach demonstrated here with the balanced MZI can be applied to the unbalanced and other MZI configurations.

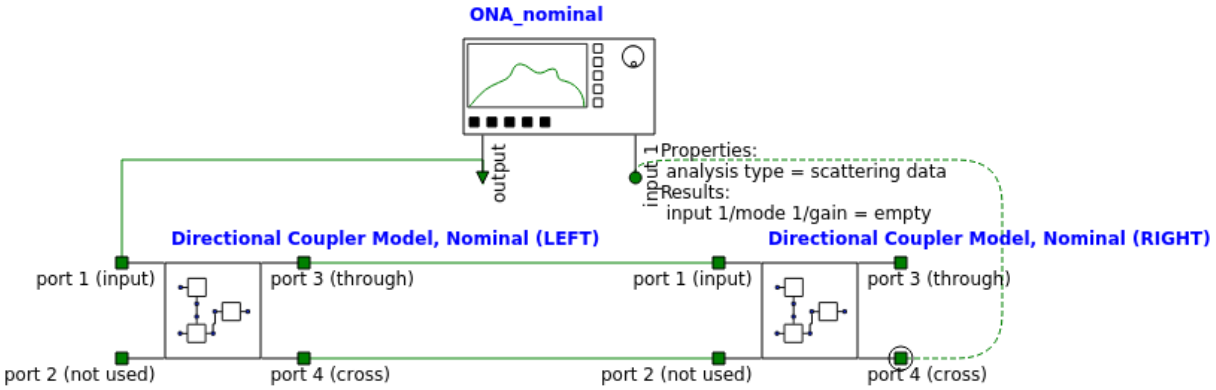


Figure 5.3: An MZI circuit simulation configuration using directional coupler compact models.

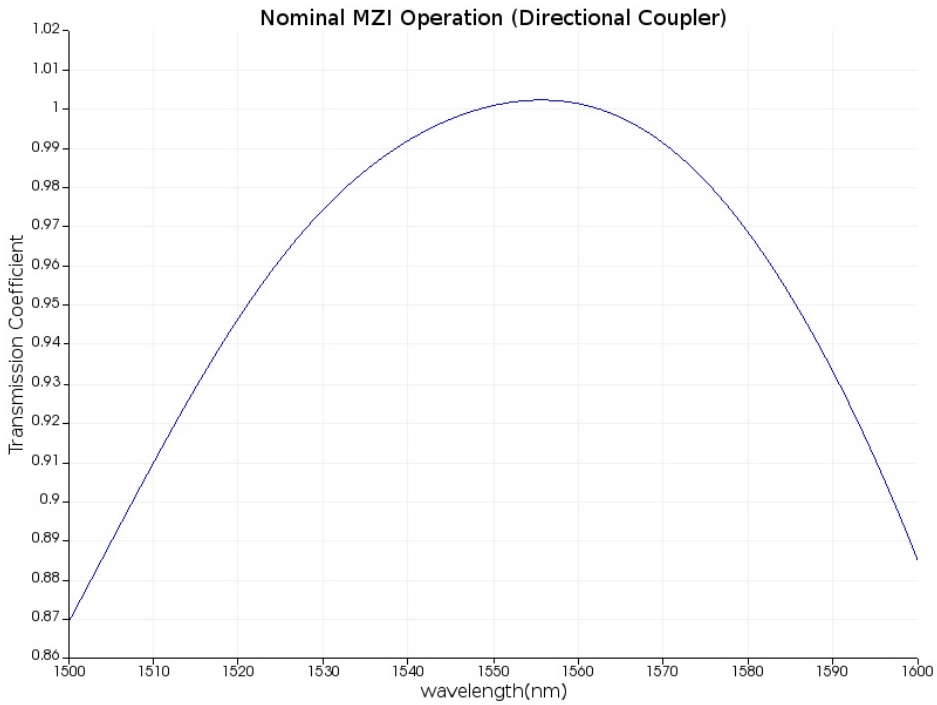


Figure 5.4: Results from simulating the nominal MZI circuit configuration composed of directional couplers in Lumerical INTERCONNECT. The compact models used are the nominal directional coupler device models discussed in Section 3.3.2. Relative transmitted power is measured at the output across the range of $\lambda = 1500$ to 1600 $nm$.

## 5.2 MZI Circuit Corner Analysis

In this section, we build upon the previous discussion of the Mach-Zehnder Interferometer and provide two photonic circuit examples. We construct the MZI using the corner compact models developed in Chapter 3. The first example is described in Section 5.2.1; here we demonstrate the operation of a Y-branch MZI using output worst-case corner models. The second example, in Section 5.2.2, demonstrates the operation of an MZI directional coupler where the components are replaced with input worst-case corner models.

### 5.2.1 Y-Branch MZI: Forming Output Corner Models

In these next examples, the Y-branch MZI is used to demonstrate the operation of output worst-case corner models. Figure **??** demonstrates the circuit setup that utilizes the output

worst-case corners of the Y-branch; the procedure for developing the corner compact model is discussed in Section 3.2. In the corner case shown in Figure 5.5, we indicate the specific corner (in the labels for the Y-branch components) as "HLL" indicating the ±5% low or high values for the respective variation parameters as given in Table 3.1. Specifically, this corresponds to the high value of $w_1$, the low value of $h$, and the low value of $w_2$.

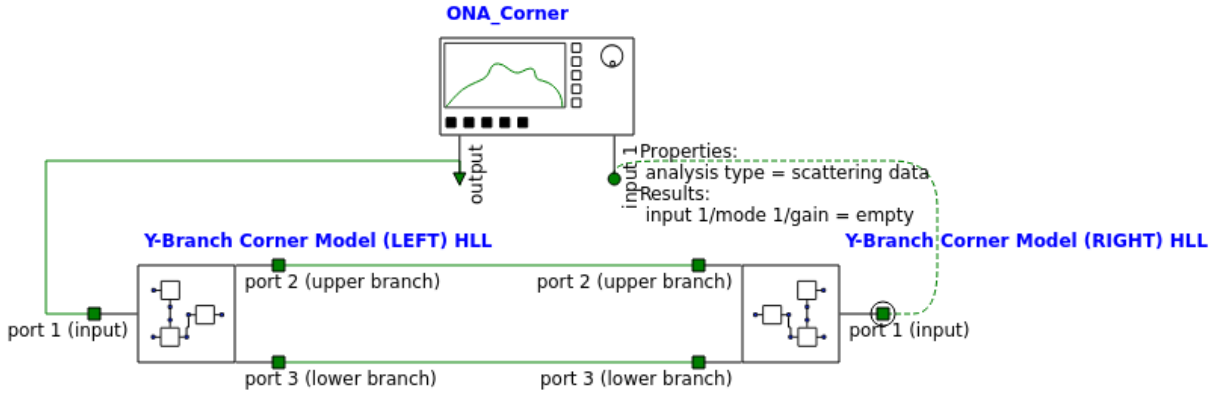


Figure 5.5: An MZI circuit simulation configuration using Y-branch compact corner models.

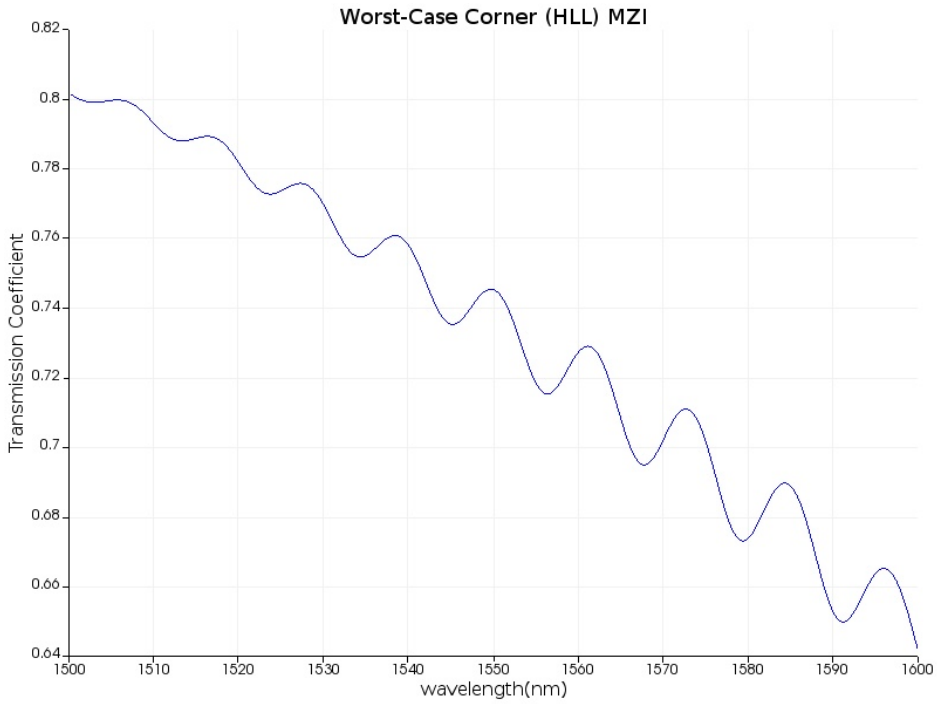


Figure 5.6: Results from simulating an MZI circuit configuration in Lumerical INTERCONNECT. The Y-branch device compact models used are the worst-case input HLL corner models.

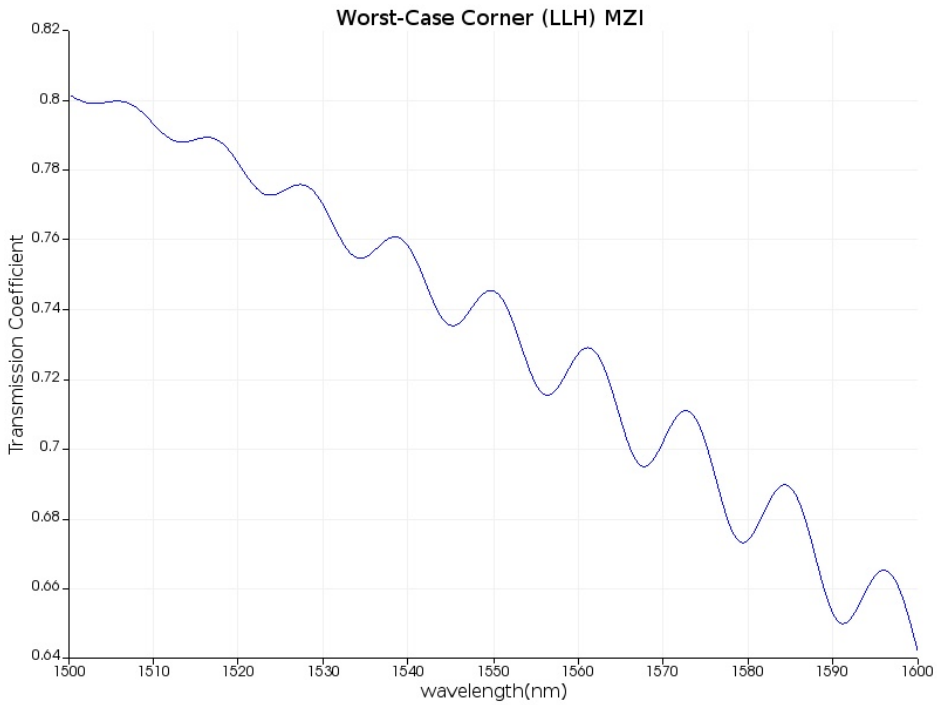


Figure 5.7: Results from simulating an MZI circuit configuration in Lumerical INTERCONNECT. The directional coupler device compact models used are the worst-case input LLH corner models. The device modeling procedure is discussed in Section 3.2.

For output worst-case corner analysis, we select only the subset of variation conditions leading to worst-case Y-branch performance, as summarized in Table 3.2. Two of these cases are shown here, for the HLL and LLH cases. Figures 5.6 and 5.7 show the results of the Y-branch output worst-case corner models in the context of the MZI circuit for these HLL and LLH cases, respectively. The corner models have significant effects on MZI operation compared to the nominal output in Figure 5.2. In both cases, the output power is significantly reduced; the wavelength-dependent oscillation in the output power is exacerbated. In the worst-case operation, the output power at 1550 $nm$ drops to about 0.75. Variations in the constituent components can cause dramatic shifts in MZI operation due to amplitude and phase sensitivity.

A further observation can be made about the HLL and LLH results shown in Figures 5.6 and 5.7. We see that in fact these two worst-case device corners produce identical MZI output deviations. This makes sense due to the symmetry of our balanced MZI configu-

ration: low upper branch widths with high lower branch widths will have the same impact as high upper branch widths with low lower branch widths. In this case, if we were to capture the results for the MZI circuit in an MZI-level variation-aware compact model, only one worst case output corner would need to be included for matched device corner analysis.

### 5.2.2 Directional Coupler MZI: Forming Input Corner Models

The Mach-Zehnder Interferometer can also be created with directional couplers. In these examples, a balanced directional coupler MZI is used to demonstrate the operation of input worst-case corner models. Figure 5.8 shows the directional coupler MZI circuit layout in INTERCONNECT, with an example input worst-case corner model, in this case the HHH corner. The input worst-case corners are based on the three-parameter ±5% corner analysis from Section 3.3.3, corresponding to parameter value deviations in Table 3.6. Specifically, input corner HHH ($L_g = 210\ nm$, $w = 525\ nm$, $h = 231\ nm$) and input corner LLL ($L_g = 190\ nm$, $w = 475\ nm$, $h = 209\ nm$) are the parameters for the cases tested. In these simulations, both couplers in the MZI are subjected to the same corner; this represents a chip-to-chip (or wafer-to-wafer) variation where all devices in the circuit share the same process deviation from the nominal.

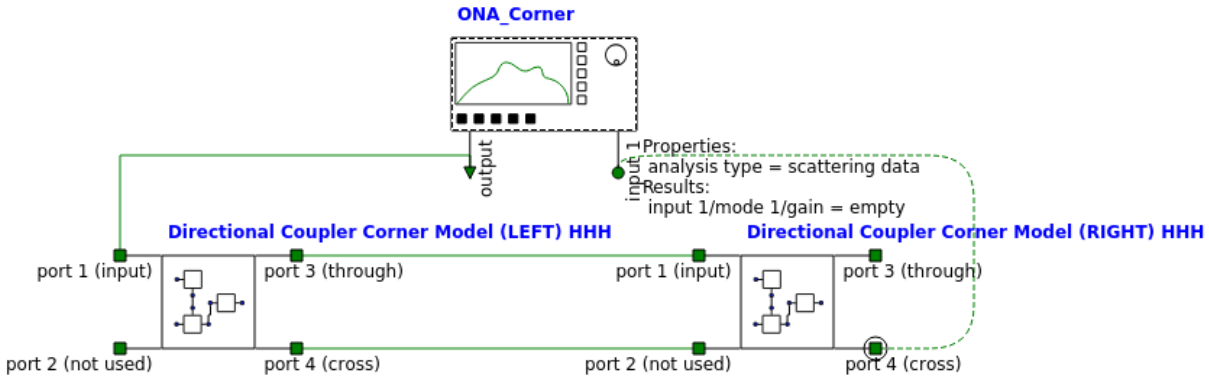


Figure 5.8: An MZI circuit simulation configuration using directional coupler compact models.

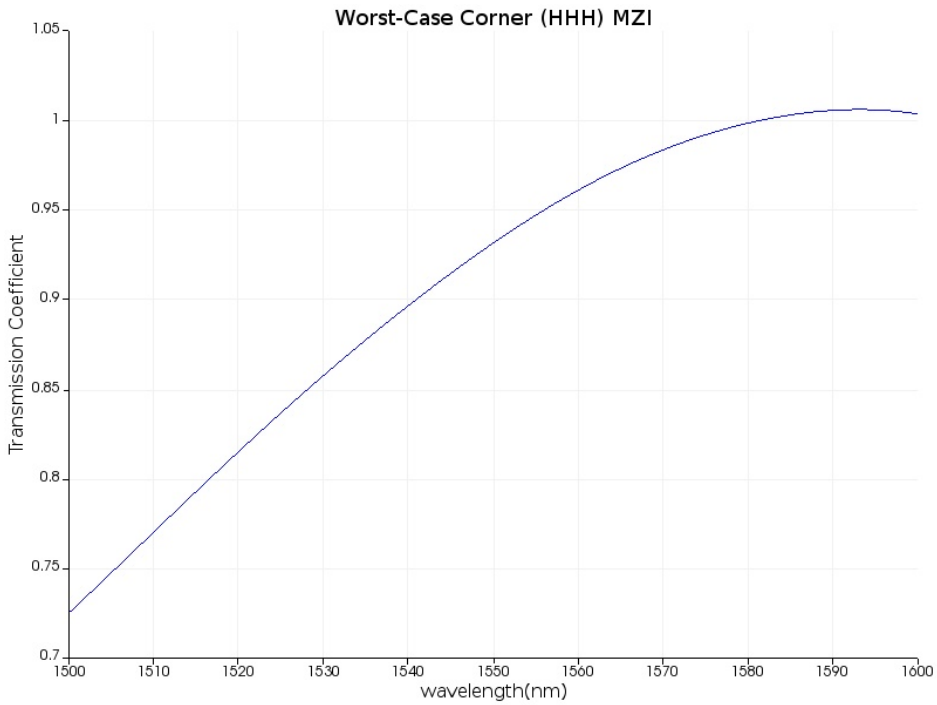


Figure 5.9: Results from simulating an MZI circuit configuration in Lumerical INTERCONNECT. The directional coupler device compact models used are the worst-case input HHH corner models.

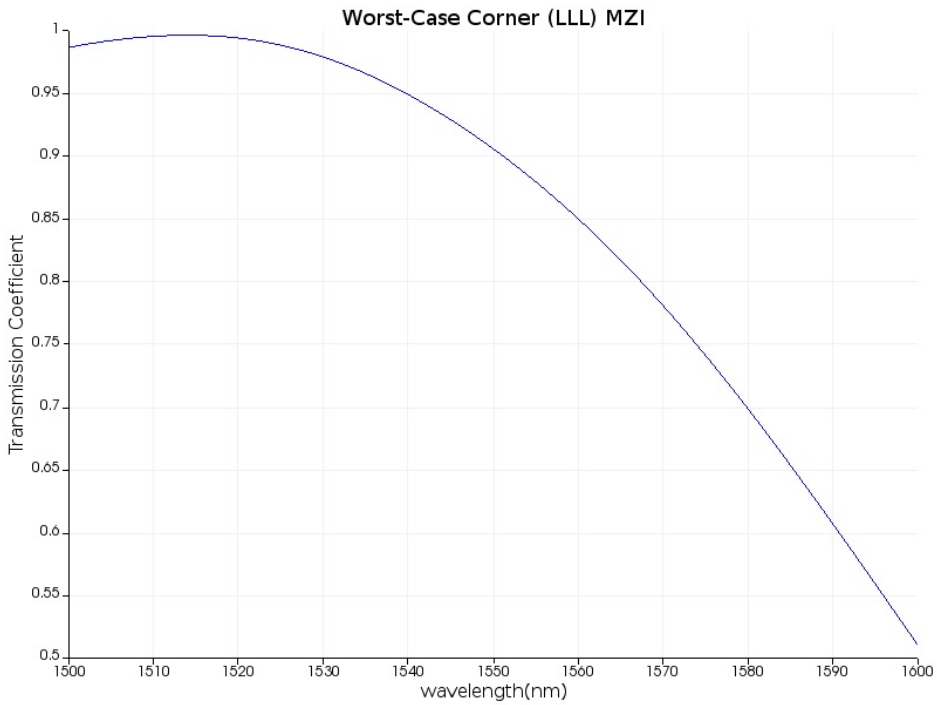


Figure 5.10: Results from simulating an MZI circuit configuration in Lumerical INTERCONNECT. The directional coupler device compact models used are from an input worst-case corner analysis (LLL corner).

Figures 5.9 and 5.10 show the results of using the input HHH worst-case corner and the input LLL worst-case corner, respectively. The corner model variations have significant effects on MZI operation. In the input HHH worst-case corner case, the peak wavelength shifts from 1560 $nm$ to about 1590 $nm$. In the MZI configuration using all LLL worst-case corners, the peak wavelength shifts from 1560 $nm$ to about 1515 $nm$. If the MZI circuit is used in a larger design, this change in behavior must be taken into account.

## 5.3 MZI Circuit Simulation Using RSM-based Compact Models

We next discuss a simulation example using compact models for the Y-branch devices that is based on the response surface method discussed in Chapter 4. This section builds upon the variation-aware compact modeling method in order to predict the behavior of the

Y-branch MZI when the individual components are subjected to statistical variations.

Figure 5.11 shows the circuit simulation configuration used. It is similar to the circuit in Figure 5.1, but the Y-branch models are now based on the response surface model developed in Section 4.2. The "LEFT" and "RIGHT" device parameter values for $w_1$, $h$, and $w_2$ are sampled at random using the same Gaussian distributions described in Section 4.2.3, specifically Equations 4.25 - 4.27. The response surface model is used to estimate the device performance for each set of randomly-sampled input parameters.

The MZI circuit is evaluated for two different scenarios. For each scenario, 100 different circuit simulations are run, and each simulation uses a different set of randomly-sampled input parameters. In the first example, both Y-branch parameter values are the same. The device performance within a single simulation instance is identical for both Y-branches, but each simulation has different Y-branch instantiations. This emulates chip-to-chip or circuit-to-circuit variations, where each circuit is different due to variations, but the components within the circuit remain matched. In the second example, each Y-branch has different parameter values; every Y-branch in every instance and simulation is completely different from the other.

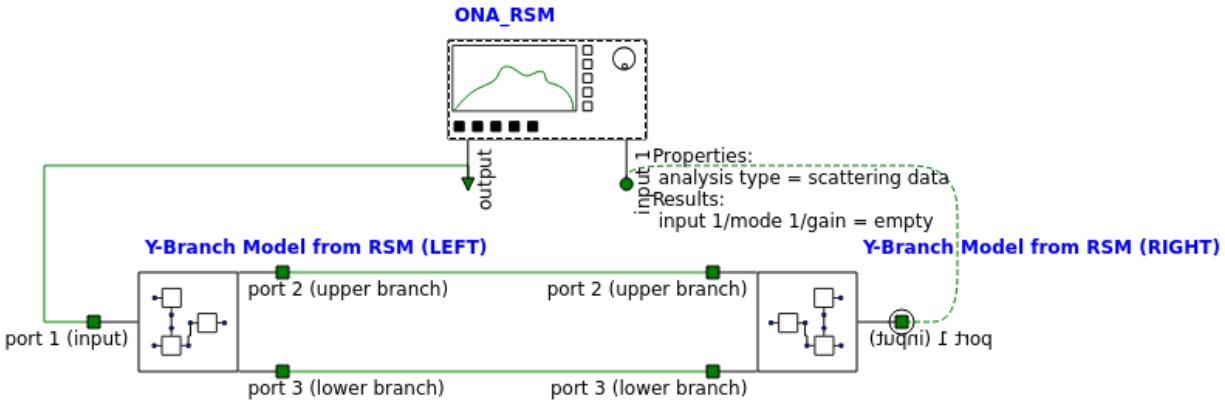


Figure 5.11: An MZI circuit simulation configuration using Y-branch RSM compact models.

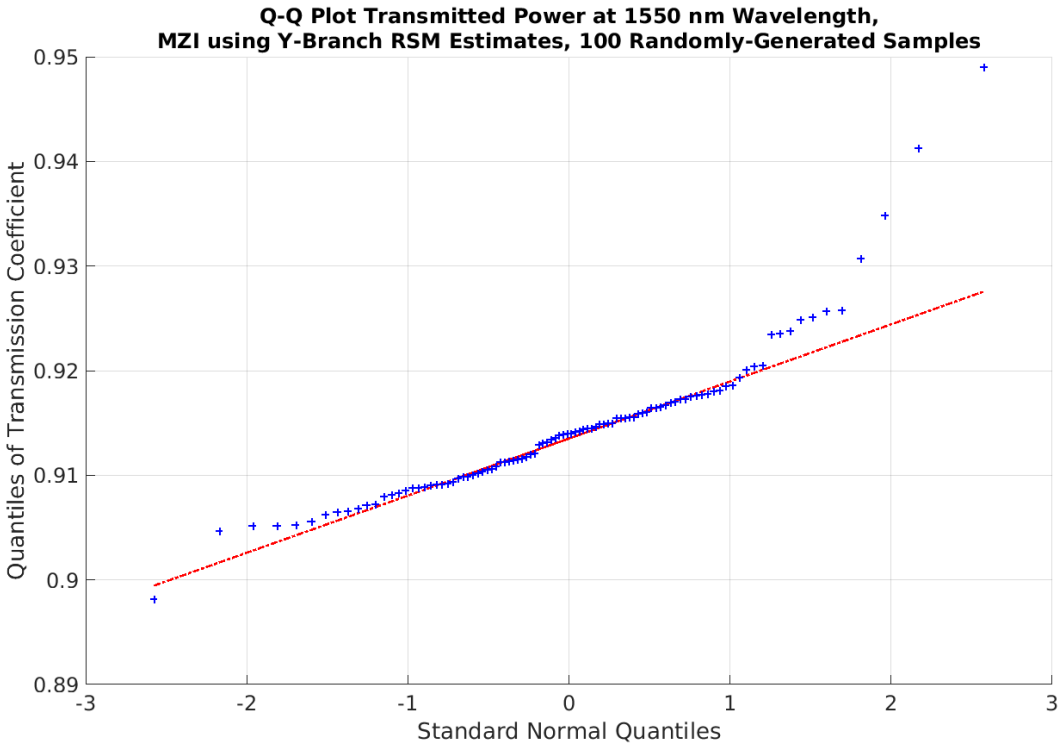


Figure 5.12: Results from measuring the relative transmitted power of the MZI at 100 random samples. Both Y-branches are randomly sampled using the distributions in Equations 4.25 - 4.27. In each MZI instance, the Y-branches use identical input parameters. Each response is generated using the Y-branch RSM compact model developed in Section 4.2. The response at $\lambda = 1550\ nm$ is recorded for each sample.

Figure 5.12 is a quantile-quantile plot that demonstrates the MZI performance when the Y-branches have identical input variations. The dashed line indicates a Gaussian distribution. We see that the resulting transmission distribution is non-Gaussian, with the low and high tails having somewhat larger transmission values than a Gaussian distribution would expect, particularly at the positive end. This may be due to the "matched" deviations in this scenario, where both components deviate in the same direction.

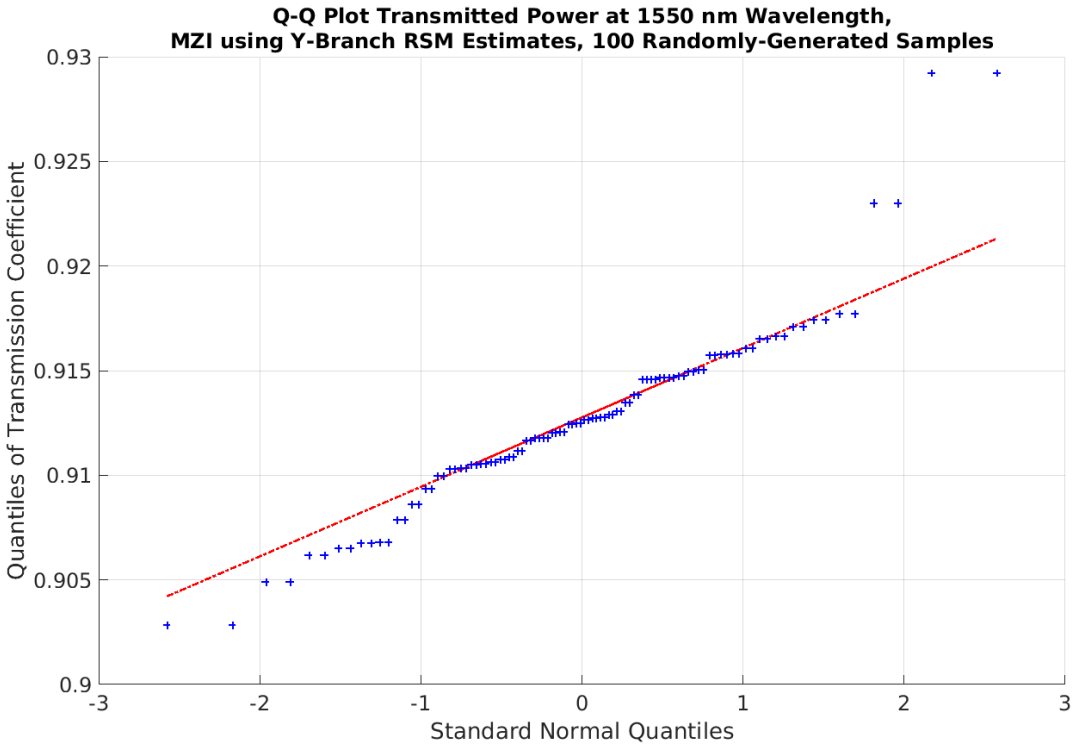


Figure 5.13: Results from measuring the relative transmitted power of the MZI at 100 random samples. Both Y-branches are randomly sampled using the distributions in Equations 4.25 - 4.27. In each MZI instance, the Y-branches use different sampled input parameters (mismatched). Each response is generated using the Y-branch RSM compact model developed in Section 4.2. The response at $\lambda = 1550\ nm$ is recorded for each sample.

Figure 5.13 is a quantile-quantile plot that summarizes the MZI performance when the Y-branches have different sampled input parameters. Again, the points are compared to a Gaussian distribution which is indicated by a dashed line. In this scenario, the distribution is again somewhat non-Gaussian, but now with increased transmission losses at the lower end compared to the Gaussian. In addition, we see that in general the distribution has somewhat lower transmission in this mismatch scenario than in the earlier match variation scenario.

These results motivate the use of response surface models for stochastic sampling simulations. It is not the case that one can simply estimate the variance in the output as $var(y) = \sum_i \left(\frac{\delta y}{\delta p_i}^2\right) \cdot var(p_i)$. This would hold if there was a simple linear relationship and no interaction among $p_i$'s, resulting in a Gaussian output distribution. In the response surface models developed for the Y-branch, interaction and higher-order terms are included,

capturing important nonlinearities that impact circuit performance distributions.

## 5.4 Summary

In this chapter, we demonstrate applications of the models developed using the modeling procedures from Chapters 3 and 4 in the context of photonic circuit simulation. The Mach-Zehnder Interferometer circuit is used as a simple but representative composite circuit. The first example presents worst case input and output corner analyses, in the context of the Y-branch and directional coupler devices. The second example demonstrates statistical analyses using random sampling in conjunction with the response surface compact models for the Y-branch. Together, these examples demonstrate the use of variation-aware compact models to predict circuit-to-circuit and device-to-device variations of a photonics design.

# Chapter 6

# Conclusions and Future Work

The field of silicon photonics continues to grow and expand; the systems being developed now are ever growing in complexity. However, photonic integrated circuits can suffer from variations. Some photonic devices can be very sensitive to process variations, and this sensitivity makes developing mass-producible photonic integrated circuit designs difficult. Multiple devices fabricated on a chip will, by nature of the manufacturing process, be constructed differently from the intended nominal device design. With each one carrying its own device performance, the overall performance of the photonic circuit may become compromised if it is not designed with manufacturing variation in mind. Thus, it is necessary for simulation models to quickly evaluate the robustness of a photonic circuit simulation to manufacturing process variations.

Further, the manufacturing process continues to improve and change, so the device simulation models will have to change with the process. Rather than creating compact models that may be obsoleted due to manufacturing process changes and improvements, the work in this thesis has attempted to address this problem by suggesting a methodology to create variation-aware compact models in simulation that can be quickly revised as fabrication data becomes available or updated. The underlying relationships between process variations and device performance can be complex; the methods developed here provide a framework to

craft compact simulation models that can quickly summarize the worst-case performance or statistical performance of a complex design.

In Chapter 2, some necessary background information on the topics of design of experiments and photonic device operation was provided. The components used for demonstrating the compact modeling methodology – the Y-branch and directional coupler – were introduced. These components were chosen as illustrative examples due to their sensitivity to geometric variations.

Once the background information was established, Chapter 3 focused on the corner analysis modeling method, the first of two modeling methods developed in the thesis. Chapter 3 provided a method for creating a compact simulation model based solely on discrete empirical results. These discrete cases are generated using design of experiments, and are meant to capture the worst-case input or output behavior of the device. Sensitivity analysis based on the DoE results was also discussed, and demonstrated for the Y-branch and directional coupler.

In practice, manufacturing variations are random. Taking this one step further, Chapter 4 suggested a method for creating models that capture continuous parameter dependencies and can take random variations into account. To achieve this, the method constructs a response surface model to estimate the underlying relationship between the process variations and the resulting device performance. A Monte-Carlo random simulation of the Y-branch was demonstrated using the parametric compact model.

Finally, Chapter 5 demonstrated the application of corner and response surface compact models. The impact of constituent device component variations on a simple Mach-Zehnder interferometer shows the value of variation analysis using our models.

There is still much work left to be done in the field of photonic device simulation modeling before it is possible to evaluate circuit designs with the same ease as in the CMOS electronics industry. This thesis has demonstrated examples of corner and response surface compact models for passive photonic components. Further development of methods to

model variations in active photonic devices is needed. Efficient statistical simulation, and ultimately robust statistical optimization methods, will help enable future photonic circuits to be designed with both high performance and high yield.

# Bibliography

[1] Orshansky, M. S. Nassif, and D. Boning, *Statistical Design and Design for Manufacturability: A Constructive Approach*, Springer, 2008.

[2] C. Sun, M. T. Wade, Y. Lee, J. S. Orcutt, L. Alloatti, M. S. Georgas, A. S. Waterman, J. M. Shainline, R. R. Avizienis, S. Lin, B. R. Moss, R. Kumar, F. Pavanello, A. H. Atabaki, H. M. Cook, A. J. Ou, J. C. Leu, Y. Chen, K. Asanovic, R. J. Ram, M. A. Popovic, and V. M. Stojanovic, "Single-chip microprocessor that communicates directly using light," *Nature*, vol. 528, no. 7583, pp. 534-538, 2015.

[3] J. Sun, E. Timurdogan, A. Yaacobi, E. Hosseini and M. Watts, "Large-scale nanophotonic phased array," *Nature*, vol. 493, no. 7431, pp. 195-199, 2013.

[4] S. Rakheja, M. Lundstrom and D. Antoniadis, "An Improved Virtual-Source-Based Transport Model for Quasi-Ballistic Transistors – Part I: Capturing Effects of Carrier Degeneracy, Drain-Bias Dependence of Gate Capacitance, and Nonlinear Channel-Access Resistance," *IEEE Trans. Electron Devices*, vol. 62, no. 9, pp. 2786-2793, 2015.

[5] L. Yu, S. Saxena, C. Hess, I. A. M. Elfadel, D. A. Antoniadis, and D. S. Boning, "Compact Model Parameter Extraction Using Bayesian Inference, Incomplete New Measurements, and Optimal Bias Selection," *IEEE Transactions on Computer-Aided Design of Integrated Circuits and Systems*, vol. 35, no. 7, pp. 1138-1150, July 2016.

[6] L. Yu, I. Elfadel, and D. Boning, "Statistical Library Characterization Using Belief Propagaion across Multiple Technology Nodes," *Design, Automation & Test in Europe (DATE)*, pp. 1383-1388, Grenoble, France, March 2015.

[7] L. Yu, S. Saxena, C. Hess, I. Elfadel, D. Antoniadis, and D. Boning, "Remembrance of Transistors Past: Compact Model Parameter Extraction Using Incomplete New Measurements and a Bayesian Framework," *Design Automation Conference (DAC)*, San Francisco, CA, June 2014.

[8] D. S. Boning, K. Valakrishnan, H. Cai, N. Drego, A. Farahanchi, K. M. Gettings, D. Lim, A. Somani, H. Taylor, D. Truque, and X. Xie, "Variation," in *IEEE Transactions on Semiconductor Manufacturing*, vol. 21, no. 1, pp. 63-71, Feb. 2008.

[9] H. Taylor, H. Sun, T. Hill, A. Farahanchi and D. S. Boning, "Characterizing and Predicting Spatial Nonuniformity in the Deep Reactive Ion Etching of Silicon," *Journal of The Electrochemical Society*, vol. 153, no. 8, p. C575, 2006.

[10] L. Chrostowski, Z. Lu, J. Flueckiger, J. Pond, J. Klein, X. Wang, S. Li, W. Tai, E. Y. Hsu, C. Kim, J. Ferguson, and C. Cone, "Schematic driven silicon photonics design," in Proc. SPIE 9751, Smart Photonic and Optoelectronic Integrated Circuits XVIII, vol. 9751, 2016.

[11] L. Chrostowski, M. Hochberg, *Silicon Photonics Design*. Cambridge, UK: Cambridge University Press, 2015.

[12] A. Farsaei, J. Klein, J. Pond, J. Flueckiger, X. Wang, G. Lamant, L. Chrostowski, and S. Mirabbasi, "A Novel and Scalable Design Methodology for the Simulation of Photonic Integrated Circuits," in Advanced Photonics 2016 (IPR, NOMA, Sensors, NEtworks, SPPCom, SOF), OSA Technical Digest (online), 2016.

[13] C. Sorace-Agaskar, J. Leu, M. Watts and V. Stojanovic, "Electro-optical co-simulation

for integrated CMOS photonic circuits with VerilogA," *Optics Express*, vol. 23, no. 21, p. 27180, 2015.

[14] Z. Peng, D. Fattal, M. Fiorentino and R. G. Beausoleil, "Fabrication variations in SOI microrings for DWDM networks," *7th IEEE International Conference on Group IV Photonics*, Beijing, 2010, pp. 120-122.

[15] W. A. Zortman, M. R. Watts, and D. C. Trotter, "Determination of Wafer and Process Induced Resonant Frequency Variation In Silicon Microdisk-Resonators," in *Advances in Optical Sciences Congress*, OSA Technical Digest (CD) (Optical Society of America, 2009), paper IMC5.

[16] K. Jinguji, N. Takato, A. Sugita, and M. Kawachi, "Mach-Zehnder interferometer type optical waveguide coupler with wavelength-flattened coupling ratio," *Electronics Letters*, vol. 26, no. 17, pp. 1326-1327, 1990.

[17] K. Okamoto, *Fundamentals of Optical Waveguides*, 2nd ed. San Diego, CA: Academic Press, 2000.

[18] A. I. Khuri and S. Muckhopadhyay, "Response surface methodology," *Wiley Interdisciplinary Reviews Computational Statstics*, vol. 2, no. 2, pp. 128-149, 2010.

[19] R. H. Myers, D.C. Montgomery, and C. M. Anderson-Cook, *Response Surface Methodology: Process and Product Optimization Using Designed Experiments*, 3rd ed. Hoboken, NJ: John Wiley & Sons, Inc., 2016.

[20] A. I. Khuri and J. A. Cornell, *Response Surfaces: Designs and Analyses*, 2nd ed., New York, NY: Marcel Dekker, Inc., 1996.

[21] G. E. P. Box and D. W. Behnken, "Some New Three Level Designs for the Study of Quantitative Variables," *Technometrics*, vol. 2, pp. 455-475, 1960.

[22] A. E. Lim, J. Song, Q. Fang, C. Li, X. Tu, N. Duan, K. K. Chen, R. P. Tern, and T. Liow, "Review of Silicon Photonics Foundry Efforts," *IEEE Journal of Selected Topics in Quantum Electronics*, vol. 20, no. 4, pp. 405-416, July-Aug. 2014.

[23] W. A. Zortman, D. C. Trotter, and M. R. Watts, "Silicon photonics manufacturing," *Optics Express*, vol. 18, no. 23, pp. 23598-23607, 2010.

[24] E. Palik, *Handbook of Optical Constants of Solids*. Elsevier, 1998.

[25] Y. Zhang, S. Yang, A. E. Lim, G. Q. Lo, C. Galland, T. Baehr-Jones, and M. Hochberg, "A compact and low loss Y-junction for submicron silicon waveguide," *Optics Express*, vol. 21, no. 1, pp. 1310-1316, 2013.

[26] H. Yamada, T. Chu, S. Ishida, and Y. Arakawa, "Optical directional coupler based on Si-wire waveguides," *IEEE Photonics Technology Letters*, vol. 17, no. 3, pp. 585-587, March 2005.

[27] M. Bertolotti, C. Sibilia, and F. Garzia, "Some nonlinear integrated optical devices," *Proceedings of 1995 SBMO/IEEE MIT-S International Microwave and Optoelectronics Conference*, Rio de Janeiro, 1995, vol. 2, pp. 784-788.

[28] A. Yariv, "Coupled-mode theory for guided-wave optics," *IEEE Journal of Quantum Electronics*, vol. 9, no. 9, pp. 919-933, 1973.

[29] C. H. Lin, M. V. Dunga, D. D. Lu, A. M. Niknejad, and C. Hu, "Performance-Aware Corner Model for Design for Manufacturing," *IEEE Trans. Electron Devices*, vol, 56, no. 4, pp. 595-600, 2009.

[30] Z. Zhang, T. El-Moselhy, I. M. Elfadel, and L. Daniel, "Stochastic testing method for transistor-level uncertainty quantification based on generalized polynomial chaos," *IEEE Trans. Computer-Aided Design of Integrated Circuits and Systems*, vol. 32, no. 10, pp. 1533-1545, Oct. 2013.

[31] T.-W. Weng, Z. Zhang, Z. Su, Y. Marzouk, A. Melloni, and L. Daniel, "Uncertainty quantification of silicon photonic deives with correlated and non-Gaussian random parameters," Optics Express, vol. 23, no. 4, pp. 4242-4254, 2015.